THESIS FOR THE DEGREE OF LICENTIATE OF ENGINEERING

Non-covalent Functionalization of 2D Black Phosphorus Nanosheets with Electron-deficient Organic Systems: Towards Enhanced Ambient Stability

ISHAN SARKAR

Department of Chemistry and Chemical Engineering

CHALMERS UNIVERSITY OF TECHNOLOGY

Gothenburg, Sweden 2025

Non-covalent Functionalization of 2D Black Phosphorus Nanosheets with Electron-deficient Organic Systems: Towards Enhanced Ambient Stability
Ishan Sarkar

Technical report no 2025:16

Department of Chemistry and Chemical Engineering
Chalmers University of Technology
SE-412 96 Gothenburg
Sweden
Telephone + 46 (0)31-772 1000

Gothenburg, Sweden 2025

Non-covalent Functionalization of 2D Black Phosphorus Nanosheets with Electron-deficient Organic Systems: Towards Enhanced Ambient Stability

Ishan Sarkar

Department of Chemistry and Chemical Engineering

Chalmers University of Technology

Abstract

In the diverse landscape of 2D materials, black phosphorus nanosheets (BPNSs) have emerged as a promising addition due to their unique properties and wide-ranging applications. However, their practical utility is hindered by poor ambient stability, primarily due to oxidative degradation in the presence of air and moisture. This process is accelerated by light exposure, which generates electron-hole pairs in BPNSs. The photoexcited electrons can transfer to oxygen molecules, producing reactive oxygen species (ROS), which collectively contribute to the structural breakdown of BPNSs.

Efforts to improve the stability of BPNSs involve various strategies such as surface passivation, encapsulation with protective coatings, and controlled environmental storage. In the present work, electron deficient organic molecules, synthesized with viologen-backbones, were combined with BPNSs to obtain nanohybrids. The interaction between the nanosheets and the molecules were characterized by UV-vis spectroscopy combined with infrared spectroscopy, Raman spectroscopy and electron microscopy techniques while the degradation of the nanohybrids exposed to the ambient condition were characterized by X-ray photoelectron spectroscopy measurement, which were compared against the samples stored in nitrogen atmosphere (pristine and functionalized) and ambient condition (pristine). Density functional theory (DFT) studies were performed to further improve the understanding behind hybrid formation efficiency and the degradability. Further series of electron-deficient molecules and polymers with viologen- and pyrene-4,5,9,10-tetraone- backbones were synthesized and preliminary tests were performed to improve the ambient stability of BPNSs.

To summarize, we showed that the electron-deficient systems are excellent candidates for functionalizing BPNSs in a non-covalent way and among them, some viologen-systems showed promising results in making BPNSs more resistant to ambient degradation. More progress has been made in synthesizing redox-active electron-deficient systems with viologen and pyrene-4,5,9,10-tetraone backbone which can be the basis for further improvements and potentially serve as materials for optoelectronics and energy-storage devices.

Keywords: Black phosphorus, viologen derivatives, pyrene-4,5,9,10-tetraone derivatives, polymers, non-covalent functionalization, ambient stability, density functional theory.

List of Publications:

This thesis is based on the results from the following publication.

I. **Boosting 2D Black Phosphorus Ambient Stability: Noncovalent Functionalization using Viologen Molecules.** Ishan Sarkar, Cong Guo, Cheng Peng, Yu Wang, Yafei Li, Xiaoyan Zhang, *Small*, **2025**, 21, 2410300.

II. **Charged Viologen Polymers with Hydrophobic Backbones Enable Improved Ambient Stability of 2D Black Phosphorus.** Ishan Sarkar, Xiaoyan Zhang, *Manuscript in preparation*.

Contribution Report:

The author has made the following contribution to the paper:

Paper I: Lead author. Synthesis, purification and characterization of molecular systems. Preparation of black phosphorus nanosheets, developing strategies for hybrid formation and characterization of the hybrids, data analysis and manuscript drafting. XPS measurements and theoretical calculations were performed by the collaborators.

Paper II: Lead author. Synthesis, purification and characterization of molecular and polymeric systems. Preparation of black phosphorus nanosheets, developing strategies for hybrid formation and characterization of the hybrids, data analysis and manuscript drafting.

Table of Contents

Abbreviations

AFM	Atomic force microscopy
AIBN	Azodiisobutyronitrile
ATR	Attenuated total reflectance
BP	Black phosphorus
BPNS	Black phosphorus nanosheet
CVD	Chemical vapor deposition
DCM	Dichloromethane
DFT	Density Functional Theory
DMSO	Dimethyl sulfoxide
FTIR	Fourier transform infrared
hBN	Hexagonal boron nitride
HOMO	Highest occupied molecular orbital
HR-TEM	High resolution transmission electron microscopy
IR	Infrared
LIB	Lithium-ion batteries
LUMO	Lowest unoccupied molecular orbital
MBE	Molecular beam epitaxy
NMR	Nuclear magnetic resonance
PLD	Pulse laser deposition
RF	Radio frequency
RP	Red phosphorus
SEM	Scanning electron microscopy
STM	Scanning tunneling microscopy
TEM	Transmission electron microscopy
TFA	Trifluoroacetic acid
THF	Tetrahydrofuran
TMD	Transition metal dichalcogenides
UV-Vis	Ultraviolet-Visible
XPS	X-ray photoelectron spectroscopy

Chapter 1

Introduction

For much of the history of materials science, research centered on bulk materials, where properties arise from the collective behavior of atoms arranged in three dimensions. This focus led to major technological breakthroughs, from structural engineering to microelectronics. However, bulk systems offered limited control at the atomic level, where new and often surprising behaviors can emerge. As the need grew for materials with greater efficiency, precision, and tunability, researchers began investigating materials with reduced dimensionality. This shift opened new avenues in nanoscale science, enabling the discovery of materials with fundamentally different properties from their bulk counterparts.

2D Materials

One of the most significant outcomes of this transition has been the rise of two-dimensional (2D) materials—atomically thin substances with lateral dimensions much larger than their thickness. Falling within the broader category of nanomaterials, which are typically defined by having at least one dimension below 100 nanometers, 2D materials have become a central focus of research over the past two decades.[1] This class essentially refers to homoatomic or heteroatomic assembly in a 2D plane with breadth in atomic dimensions and characteristics usually including bulk properties along with phenomena from the quantum realm.[2]

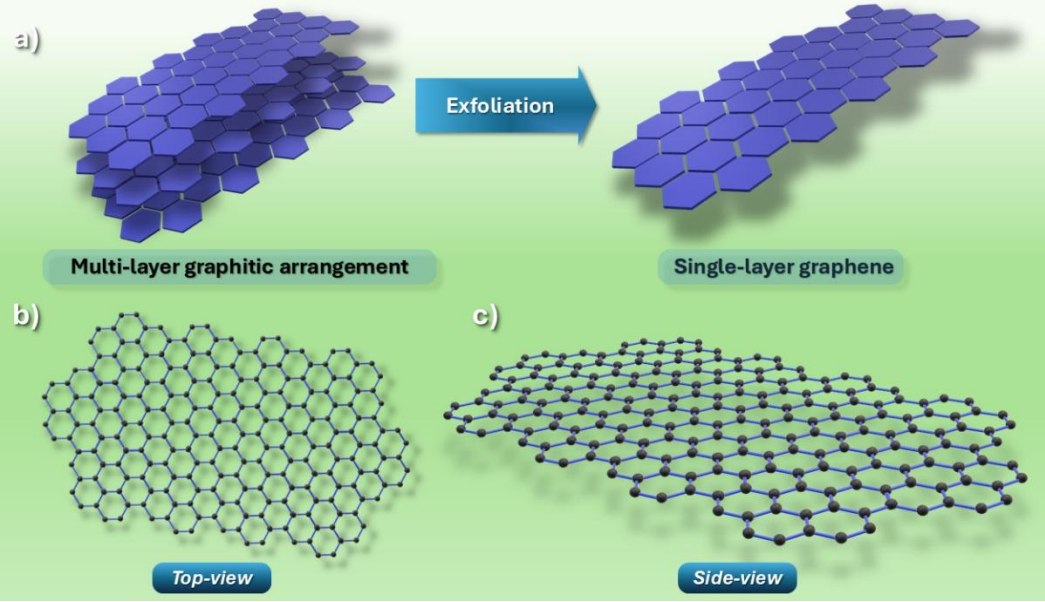

Figure 1.1. *Visual representation of (a) multi-layer graphitic arrangement (precursor) and single-layer graphene, (b) graphene showing its hexagonal array of sp^2 carbon atoms on its top view and (c) on its side view.*

The most celebrated discovery of graphene from crystalline graphite via scotch-tape exfoliation by Geim and Novoselov has been the cornerstone for the research in the domain of 2D materials as it showcases the ease of preparing an extraordinary substance from something very simple

and common.[3] A one-atom-thick planar array of sp^2-carbon atoms (Figure 1.1) in a honeycomb-lattice makes graphene the thinnest and the strongest 2D material known. This unique structural configuration endows graphene with a zero bandgap and enables its exceptional electron mobility[4-6] and thermal conductivity,[7] ambipolar field effect,[8] fractional quantum Hall effect,[9] proton permeation,[10] large specific area[11] with high transparency and high intrinsic strength.[12] Owing to these exceptional characteristics, graphene has found tremendous reach in various research fields including energy industry, medicines, electronics, food industry, sports and many other miscellaneous areas. Despite having all the desirable qualities in one material, graphene faced big challenges due to its limitations e.g. its market growth is slowed by high costs, inconsistent performance, and the lack of major breakthrough applications. Its properties depended heavily on the surface area and the number of layers.[13] Producing graphene on a large scale at a reduced cost often compromises its quality. Applications demanding superior-quality graphene typically rely on expensive methods, such as chemical vapor deposition (CVD).[14] As a result, rather than focusing solely on tailoring graphene for specific applications, researchers began exploring new 2D materials.

Black phosphorus

Discovery of black phosphorus (BP) dates to 1914 by Bridgman who obtained this specific allotrope of phosphorus from white phosphorus at a pressure of 1.2 GPa and an elevated temperature of 200 °C.[15] However, for the upcoming 100 years it failed to gain research interest partially because of the semiconducting research with silicon as a bulk material being overpowering to a large extent.[16] Nonetheless, the last decade brought forth a new perspective of thin film materials having only two dimensions and BP along with transitional metal dichalcogenides (TMDs) and hexagonal boron nitrides (hBNs) resurfaced as alternatives to futuristic science. Within the last decade, detailed studies have been conducted covering the properties of BP such as its band structure,[17] defects,[18] intercalation,[19] layer dependency, characterization methods,[20, 21] stability and passivation strategies,[22, 23] novel physical phenomena[24, 25] and applications in energy storage, opto-electronics,[17, 26-31] sensing,[32] etc.

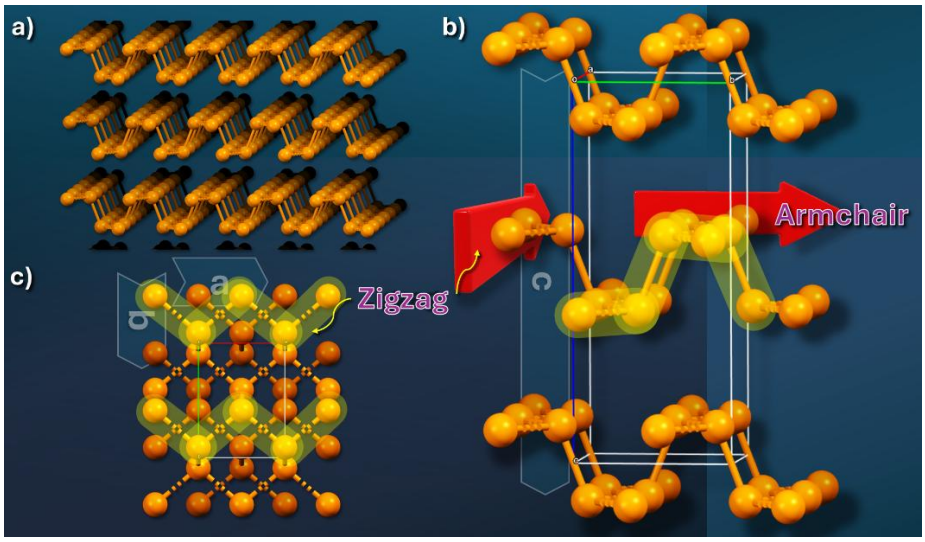

Figure 1.2. *BPNS crystal structure showing (a) 2D nanosheets stacked in bulk BP and the illustration of the zigzag and armchair directions in the crystal lattice from the side view (b) and the top view (c).*

The crystalline structure of BPNSs (Figure 1.2) consists of orthorhombic crystal structure with space group Cmca where the lattice parameters are as follows: a = 4.37 Å, b = 3.31 Å and c = 10.47 Å.[33] The bonds connecting two phosphorus atoms in plane has a bond length of 2.224 Å whereas the same for the ones connecting two planes of the monolayer is 2.244 Å.[34, 35] Theoretical calculations show that upper part of the valence band consists of bonding 3p levels and the lower part of the conduction band consists of antibonding 3p levels with a calculated energy gap of 2.5 eV at the Γ point (center of the irreducible Brillouin zone) of the Brillouin zone (the Wigner-Seitz cell constructed in reciprocal lattice (k-space) by taking one lattice point as a center) for a monolayer.[34, 35] Xia et al.[36] reported an absorption peak at 2700 cm^{-1} (~0.3 eV) corresponding to the band gap of bulk BP, which can increase to 2.05 eV in its single-layer form, as measured through STM characterization by Liang et al.[37] Hence, the bandgap of BPNSs falls between the zero band gap of graphene[38] and the larger bandgap (1.5-2.5 eV) of TMDs,[39, 40] enabling strong wave-matter interactions, particularly with electromagnetic waves in the mid-infrared, near-infrared and visible-frequency regions.

Despite having such desirable properties, BPNSs suffer from numbers of disadvantages which diminish their relevance in applicability. Bulk BP has been observed to have a long lifetime under ambient conditions, however, single- and few-layer BPNSs degrade over time in the presence of moisture, oxygen and exposure of light.[41] It has been hypothesized that the degradation mechanism begins with a light-dependent initiation process generating superoxide radical anion from molecular oxygen leading to peroxide species formed on the nanosheets. This process propagates within the nanosheets through involvement of surrounding water molecules eventually forming phosphoric acid (discussed later in Chapter 2).[23]

Chemical functionalization of 2D materials

Functionalization of materials is a strategy where materials are generally doped with atoms, molecules or even with other materials. Chemical functionalization on 2D materials provides tunability over long-range across the surface/edge while preserving the structural characteristics making the hybrid material accessible for technological implementation. Modifications of this sort can roughly be achieved through two different methodologies: (i) covalent and (ii) non-covalent functionalization (Figure 1.3).[42-45] As the name suggests, covalent functionalization occurs through forming covalent bonds in between the material and the functional module while the latter doesn't involve direct bond formation rather utilizes various sort of non-covalent interactions where several intermolecular forces are operating, for example, electrostatic forces, hydrogen bonding, π-π/charge-π interactions, different van der Waals interactions such as Keesom forces (dipole-dipole), Debye forces (dipole-induced dipole) and London dispersion forces, etc.[43] It is indeed noteworthy that unlike covalent modification, non-covalent functionalization can potentially be reversible and enables minute alteration of electronic properties for 2D materials. Both strategies enable scope for surface passivation/encapsulation which in turn can be implemented as a possible method for enhanced ambient stability.

Diazonium chemistry is a well-established reaction for covalent functionalization (Figure 1.3) in the case of graphene, nanotubes and other 2D materials and can be extrapolated in case of BPNSs as well.[46-48] Along with this, another radical based method that has been well explored is diaryliodonium salt chemistry that has been previously employed and was observed to have higher protection efficiency against ambient degradation of BPNSs since through this approach both phosphorus-ends as well as the oxygen-ends of the already oxidized nanosheets could be

functionalized.[49] Apart from these, BPNSs were also reported to have been functionalized by carbon free radicles from azodiisobutyronitrile (AIBN) molecules,[50] nucleophilic substitutions,[51] carbene[52] and nitrene[53] additions. Alkali metal intercalation[54] is another kind of modification which is beyond the scope of discussion.

Noncovalent interaction (Figure 1.3) refers to any interaction between two or more moieties where the moieties involved in the interaction do not share any electron. There are several different kinds of noncovalent forces, one of which is electrostatic interactions. Ionic forces and van der Waals forces are two subcategories of electrostatic forces. Van der Waals forces include dipole-dipole (Keesom force), dipole-induced dipole (Debye force) and induced dipole-induced dipole (London dispersion force) interactions. van der Waals forces act only at short distances and decay much more rapidly with increasing separation than electrostatic forces.

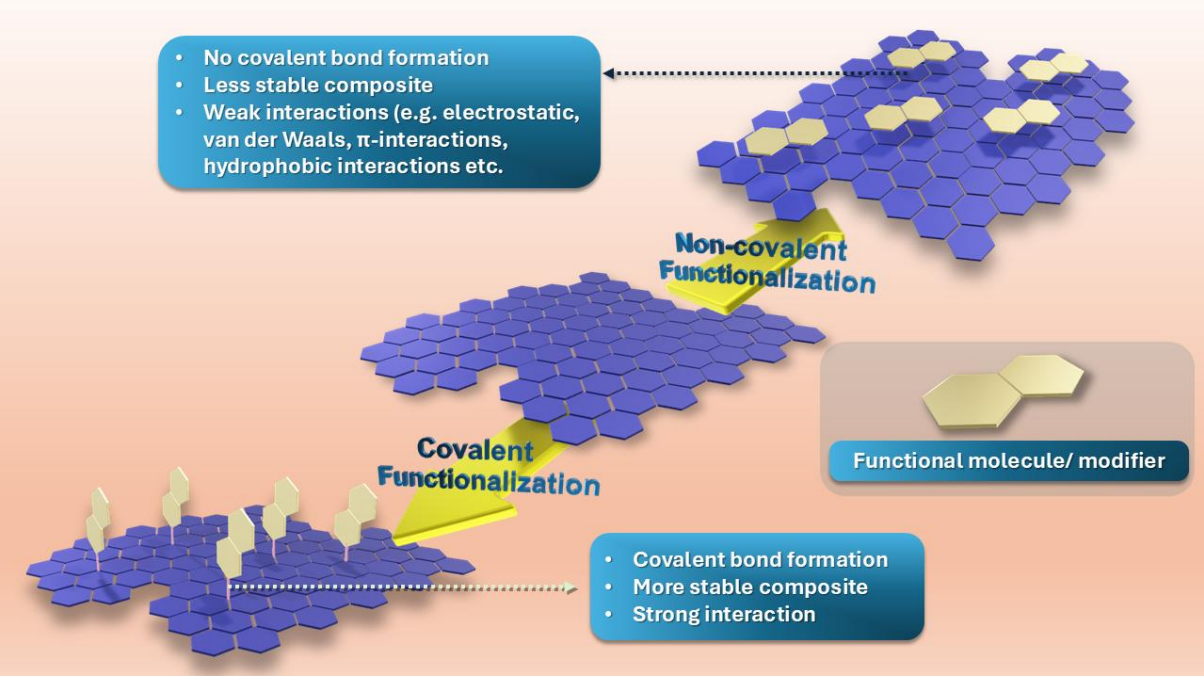

Figure 1.3. *Visual representation of covalent and noncovalent functionalization.*

Another very common and heavily explored non-covalent interaction is π-interaction. Displaced, edge-to-face and T-shaped interactions are more favorable than direct stacking which is unstable due to repulsion of the electron clouds within two molecules. Different charges (cations and anions) and polar hydrogens can also interact with π-clouds and have been heavily studied in different biological systems and organic catalysis.[55]

Hydrophobic interactions are commonly misjudged as a kind of van der Waals force and occur between water and substances which have very low polarity and low water-solubility. This sort of non-covalent interaction is purely thermodynamic and operates by minimizing free energy available in the system. A very common example of hydrophobic interaction is a mixture of oil and water. The separated phase of oil and water has more randomness (entropy) than the mixture phase where oil is mixed with water and exists in the water as smaller droplets.

Hydrogen bonding plays a crucial role in the functionalization of 2D materials, such as graphene oxide, MXene, etc.[56, 57] Hydrogen bonding is an attractive force that occurs between a hydrogen atom, which is part of a molecule or molecular fragment (X–H, where X is more electronegative than hydrogen), and another atom or group of atoms in the same or a different molecule. This interaction is supported by evidence of bond formation (X−H···Y, where Y serves as the hydrogen bond acceptor).[58]

Research in 2D materials relies heavily on functionalization methods and on the interactions between individual components during hybrid formation, as these determine their tunability and processability for industrial applications. However, the unique physicochemical characteristics of many 2D materials often limit the scope of viable functionalization techniques, creating a bottleneck in the development of more robust hybrid architectures. In the case of black phosphorus nanosheets (BPNSs), ambient photo-oxidation (discussed in detail in Chapter 2) significantly hinders their long-term applicability, as the highly reactive phosphorus atoms are very prone to oxidative degradation[59] despite the bulk black phosphorus is widely accepted as the most thermodynamically stable allotrope of phosphorus.[60] To date, no approach has been able to completely nullify the intrinsic oxidizable nature of the phosphorus atoms in BPNSs over longer period. Therefore, this thesis aims to investigate and develop novel strategies to enhance the ambient stability of BPNSs by preventing or minimizing their degradation under ambient conditions.

Chapter 2

Theory and method

Preparation of black phosphorus nanosheets (BPNSs)

BPNSs, also known as phosphorene, can be prepared by either a top-down method or a bottom-up method. A top-down synthesis approach essentially refers to a process where a specific material is obtained by breaking a larger or more complex material down whereas, a bottom-up approach is where the material is assembled from much simpler forms of materials, ideally atoms or small molecules.[61]

Top-down approach for BPNSs preparation

The top-down method for BPNSs preparation exploits the presence of weak van der Waals forces in between nanosheets in the bulk form and aims to achieve single- or few-layer nanosheets by breaking the weak force (Figure 2.1). Mechanical exfoliation is a very common example of a top-down method, and the famous scotch tape method is a very popular form among this category.[62] Although this produces very high quality nanosheets but suffers from scalability issues. Ball-milling technique is another form of the top-down approach in which instead of bulk BP crystals, red phosphorus (RP) is directly used. The RP powder goes through high pressure conditions generated via collision, shearing and friction.[63] Among the liquid phase exfoliation strategies, sonication is an effective way to exfoliate single- and few-layer nanosheets and can be performed in various solvents (organic solvents, water, ionic liquids, etc.), sometimes assisted by polymers or surfactants. Power and the duration for the sonication affects the size of the nanosheets.[64] Electrochemical exfoliation is another liquid-phase exfoliation technique in which ion intercalation occurs between the layers of the bulk material, followed by redox reactions of the ions. This process often generates gas bubbles within the interlayer space, forcing the layers to separate.[65] Liquid phase exfoliation is indeed very effective way of generating single- and few-layer nanosheets on a large scale, however, the uniformity of the nanosheets remains uncertain. Plasma-etching is known to produce nanosheets by chemical reactions induced by the diffusion of plasma-induced radicals. This gives precise control over thickness but is not suitable for large scale production due to high cost and specialized instruments required.[66]

Bottom-up approach for BPNSs preparation

BPNSs prepared by bottom-up approach essentially means fabricating the nanosheets by depositing phosphorous atoms on a smooth surface with negligible roughness (Figure 2.1). Chemical vapor deposition (CVD) provides high quality nanosheets with precision in doping and defect regulation.[67] Molecular beam epitaxy (MBE) is also used to prepare nanosheets by epitaxial growth in ultra-low-pressure environments on selected substrates allowing the nanosheets to have high degree of crystallinity.[68] Another thin-film deposition technique to produce nanosheets is pulse laser deposition (PLD), where a solid target is exposed to high energy laser pulses eventually vaporizing the surface and the vapor is then condensed over a substrate thus, forming the nanosheets.[69] Bottom-up approaches, as mentioned before, can be used to synthesize high quality and defect-less nanosheets, however, high cost of production along with low yields, expensive instrumentation and requirement for specialized expertise limits its applicability on a large scale.

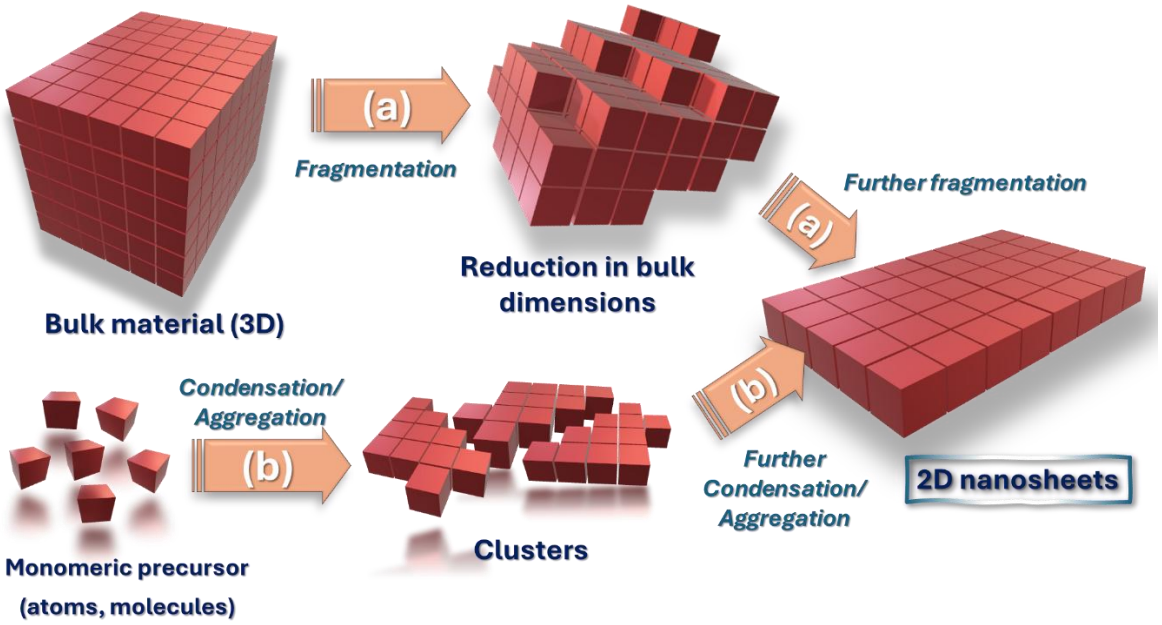

Figure 2.1. *Illustration showing the preparation methods of 2D materials: (a) top-down approach and (b) bottom-up approach.*

Degradation mechanism

Phosphorus and its different allotropes are all together more or less prone to oxidation and BPNSs are no exception for that. Many studies have been conducted over the years to determine the steps the nanosheets go through and the parameters which are responsible for the degradation process along with the studies conducted based on the theoretical calculations, giving us more insights into the probable intermediate species throughout the process. Three components that are found to have important roles in the mechanism are light, oxygen and water. Light exposure is the triggering step and heavily dependent on the band gap of the material. Multi-layer BPNSs possessing a direct band gap of ~1.51 eV at the Γ point is suitable, as the redox potential for O_2/O_2^- falls within the range. This is also the reason why the bulk BP crystals are more resistant to oxidation as their band gap is closer to 0.37 eV, which is much lower than the redox potential for O_2/O_2^-. The initiation process occurs by an electronic transition from the valence band to the conduction band in the presence of light, creating an exciton pair. An electron transfer occurs afterwards from the conduction band to the LUMO of an oxygen molecule, creating a peroxide radical anion (Figure 2.2). Further calculations suggest that the bond between the two oxygen atoms is elongated and a bond between phosphorus and oxygen is established. The last step as per the calculations is the propagation step in presence of water molecules, where the water molecules approach the nanosheets due to the hydrogen bonding present between the water molecules and the oxidized nanosheets, breaking the P−P bond and losing the structural integrity.[41]

The oxidation of BPNSs were characterized by Wood et al., and the formation of phosphoric acid bubbles under prolonged exposure to ambient conditions were confirmed by atomic force microscopy (AFM) measurements.[23] This was also known previously and was characterized by scanning tunneling microscopy (STM) tests. When the BPNSs were imaged in air, the formation of the bubbles on the surface was often seen as the tip approached the tunneling distance to the nanosheet surface.[70]

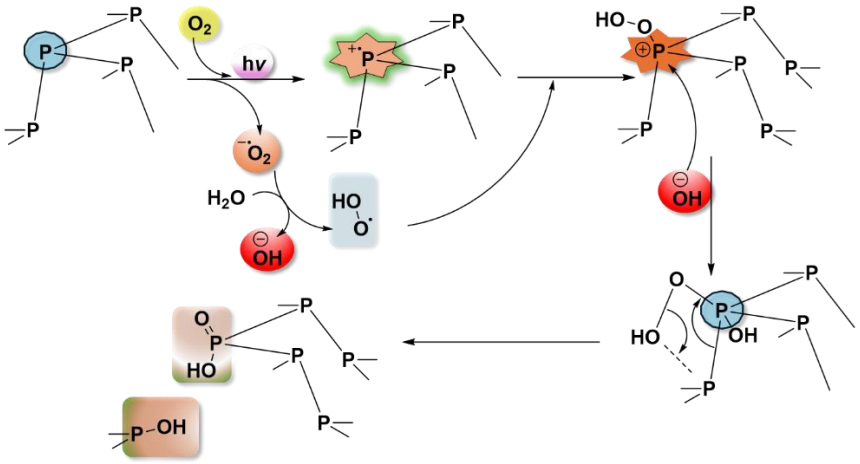

Figure 2.2. *Schematic representation of the degradation mechanism of BPNSs.*

Electron deficient organic molecules with redox sites such as cationic viologens and pyrene-4,5,9,10-tetrone systems have been employed before forming multiple composite materials due to their unique electronic properties. However, novel cationic compounds from these systems and hybrid formation strategies are still very much of a research interest. Additionally, the negatively charged nanosheet surface and the electron-deficient nature were hypothesized in this thesis to interact and provide effective ambient-stability through potential encapsulation. Some essential backgrounds and synthetic fundamentals are discussed below for these two systems.

Viologens and their properties

Viologens are a class of organic salts where the 4,4'-bipyridines are di-quaternized and can be expanded to have extended conjugated aromatic systems. The name viologen originates from their ability to generate violet colors, a characteristic observed for viologens and their derivatives upon reduction. N-alkylation/acylation/arylation and Zincke reaction[71] (Figure 2.3) are the most popular ways of synthesizing viologen derivatives, whereas oxonium ion substitution and reductive coupling are less common.[72] Bi-methylated bipyridines, also known as paraquat, has widely been used as herbicide as well as redox indicators. The toxicity towards herbicides is related to their ability to interfere with electron transfer processes which in turn inhibit photosynthesis in them.[73] Each step in the reduction process of a viologen derivative involves one electron transfer (Figure 2.4) and generates stable and delocalized radical which is also the reason for viologens being able to produce dramatic change in color in a reversible way.[74, 75] This reversible redox capability makes viologen derivatives a suitable choice for electrochromic devices and charge-storage devices.[76]

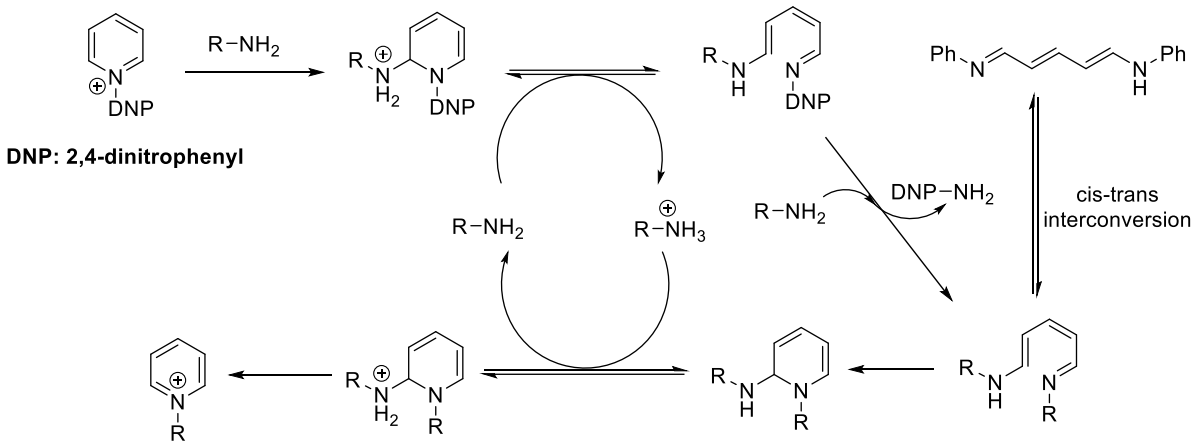

Figure 2.4. *Schematic representation of the mechanism of Zincke reaction.*[77]

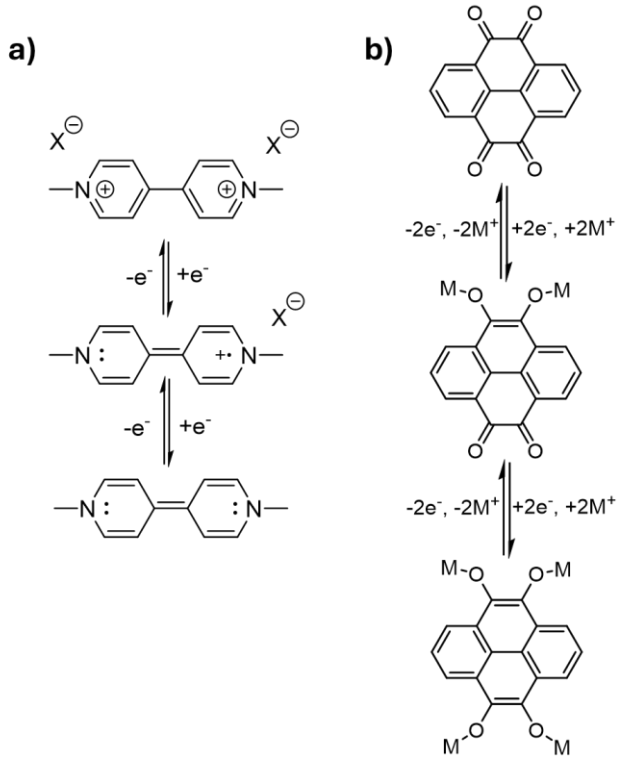

Figure 2.5. *Schematic representation of the redox process for: (a) viologen moieties and (b) pyrene-4,5,9,10-tetrone (e^- = electron, M = H, metals; as the charge storage mechanism involves cations).*

Pyrene-4,5,9,10-tetrone derivatives and their properties

Among all the derivatives of pyrene, pyrene-4,5,9,10-tetrone is the most explored in the field of energy storage and their photosensitizing ability. Its photosensitizing ability has been characterized in detail along with the intermediates formed during the process.[78] Theoretical studies also showed that the triplet T_3 state generation occurs in this molecule via vibrational coordinate-dependent spin-vibronic coupling, which rapidly and efficiently decays to the T_1 state, thus making it a suitable candidate for photosensitizers.[79] The system can be further

modified at the 2,7-positions to have fine-tuned HOMO-LUMO levels.[80] Pyrene-4,5,9,10-tetrone in its unmodified form is redox-active and the redox reaction occurs in two steps where each step is a two electron process (Figure 2.5) enabling it to be applied as cathodes in fast-charge, fast-discharge Li-ion batteries (LIBs).[81] Here we have employed Suzuki coupling reactions to further modify the pyrene-4,5,9,10-tetrone systems (Figure 2.6).

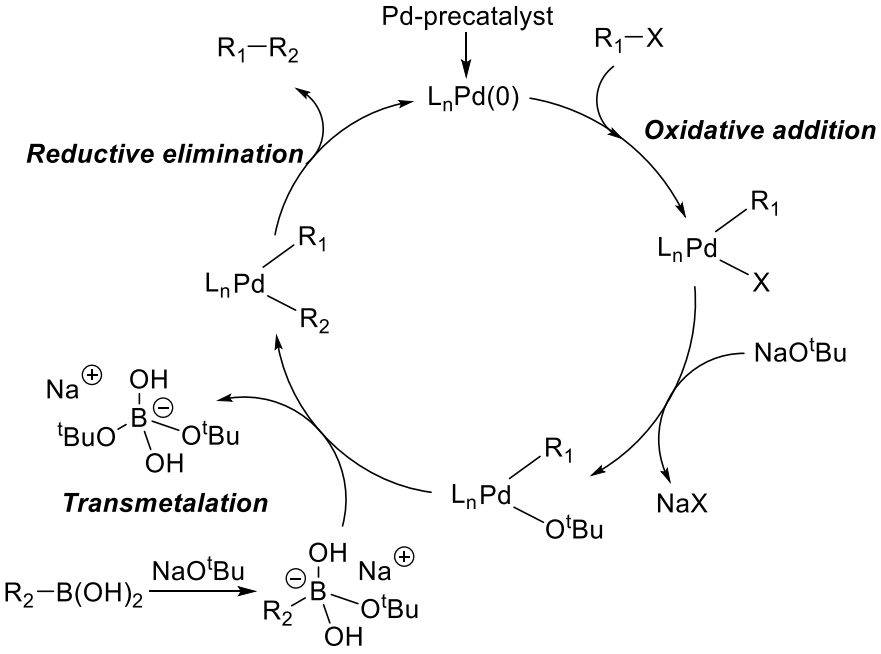

Figure 2.6. *Schematic representation of the mechanism of Suzuki coupling reaction.*

Characterization methods

Nuclear Magnetic Resonance (NMR) is one of the key techniques often utilized in organic chemistry to reveal information about atomic connectivity, functional groups, and molecular conformations in molecules and materials. This technique operates on the interaction between atomic nuclei with nonzero spin and an external magnetic field. When subjected to this field, nuclei occupy discrete energy levels based on their spin states. Upon absorbing radiofrequency (RF) radiation at a specific resonance frequency, they undergo transitions between these states. The resonance frequency varies due to the surrounding electronic environment, giving rise to chemical shifts. Additionally, interactions between neighboring nuclei create spin-spin coupling, further refining structural analysis.

Infrared (IR) spectroscopy is an analytical technique used to identify molecular structures by measuring the absorption of infrared radiation, which causes specific vibrational modes within a molecule. Different functional groups produce characteristic absorption bands corresponding to distinct vibrational modes (such as stretching or bending) influenced by the bonds and local molecular environment. The resulting IR spectrum displays absorption frequencies at which the molecule undergoes vibrational transitions, providing insight into the presence of specific chemical bonds and functional groups. This technique is widely applied in organic and inorganic chemistry for structural analysis, compound identification, and material characterization.

Raman spectroscopy is another analytical technique that measures the scattering of monochromatic light, typically from a laser, by a sample. This scattering results in shifts (Stokes or anti-Stokes) in the light's energy, corresponding primarily to vibrational and sometimes rotational transitions in the molecule (by inducing virtual states depending on the polarizability of the molecule). The resulting Raman spectrum provides information about molecular vibrations, chemical composition, and structural features, making it useful for material characterization and identifying functional groups.

UV-Vis (Ultraviolet-Visible) spectroscopy is an analytical technique that measures the absorption of ultraviolet and visible light by a sample. When light passes through or is reflected from a sample, molecules absorb specific wavelengths of light, causing electronic transitions. The resulting spectrum shows absorption peaks, which provide information about the molecular structure, electronic states, and concentration of the sample.

Zeta potential is the electrical potential at the shear plane of particles in suspension and serves as a key measure of colloidal stability. Larger absolute zeta potential values indicate stronger electrostatic repulsion and greater stability, whereas values near zero imply a tendency toward aggregation or flocculation. This method is exclusively for particles, and the small molecules cannot be detected as the detection is completely dependent on the electrophoretic scattering of light by the particles (laser Doppler velocimetry). Stability behavior of the particles with zeta potential range of 0 to ±5 mV corresponds to rapid coagulation or flocculation, ±10 to ±30 mV implies instability, ±30 to ±40 implies moderate stability, ±40 to ±60 mV implies good stability and more than ±61 usually corresponds to excellent stability.

X-ray Photoelectron Spectroscopy (XPS) is a surface-sensitive analytical technique used to determine the elemental composition, chemical states, and electronic states of materials. When a sample is exposed to X-rays, they interact with core electrons, ejecting them from the atom's core shell. The kinetic energy of these ejected electrons is measured, and from this, the binding energy can be calculated. This binding energy is characteristic of the element, the electron's specific orbital, and the chemical environment, allowing for the identification of elemental composition and oxidation states. XPS provides detailed information about the surface of a material, typically probing the top 1-10 nm of the sample surface, depending on the X-ray energy and the energy of the emitted photoelectrons. This makes XPS particularly useful for analyzing thin films, coatings, catalysts, and surface modifications, where surface properties are critical. The technique can quantify elemental abundance and detect changes in the chemical environment of atoms, making it valuable for studying interfaces, corrosion/oxidation, and surface reactions.

The techniques explained above serve as fundamental and essential methods for characterization used in the discussions in Chapter 4. The results from the characterization methods shed light on the fabrication of hybrid formation-dynamics as well as their morphology. Ambient stability was also characterized further by these methods, and the functionalization degree was quantified.

Chapter 3

Hypothesis and aim

The thesis focuses on addressing the ambient stability challenges associated with BPNSs and improving its long-term durability by preventing the oxidation of the nanosheets. This oxidation process predominantly leads to structural deterioration, altering its electrical and optical characteristics and significantly limiting its practical applications in nanoelectronics, optoelectronics, and energy storage devices. This brings forth several hypotheses as discussed below.

1. BPNSs can be functionalized non-covalently with cationic π-conjugated systems.
2. Electron deficient systems are important for passivation of the electron rich environment of BPNSs.
3. The number of charges in the π-conjugated systems affects the interaction and protection efficiency.
4. Introduction of hydrophobic and electrostatic interactions could further inhibit oxygen and water adsorption.

The hypotheses, hence, set forth the following aims.

1. Synthesis of a series of cationic π-conjugated systems with varied number of charges and electron deficiency.
2. Method development for the non-covalent functionalization of BPNSs.
3. Characterization of hybrid systems and analysis of structure-property relationships.
4. Determination of the protection-efficiency of BPNSs and the hybrids using different characterization techniques.

Chapter 4

Results and discussions

Synthesis and characterization

To solve the ambient stability issue of BPNSs and study their structure-property relationships, a series of π-conjugated electron deficient organic molecules have been synthesized. The design of the compounds was based on a speculative orbital interaction of the electron deficient π-systems and the electronic environment of the anisotropic nanosheet surface. Furthermore, hydrophobic alkyl chains were also incorporated in the design of compounds to block the approach of water and/or oxygen to the surface, thus, potentially reducing the oxidation of the nanosheets. This thesis focuses on the derivatives synthesized from 4,4'-bipyridine and pyrene-4,5,9,10-tertaone.

Strategies for viologen derivatives

There are four different structural aspects based on which the derivatives have been designed (Scheme 4.1). Double methylation of 4,4'-bipyridine is the simplest way to make the π-system electron deficient (Scheme 4.1, compound **3**). Then two modules of doubly charged bipyridinium modules were connected through a benzene linkage increasing the number of charges in one molecule (Scheme 4.1, compound **9**). It is noteworthy that the charges created on the pyridine systems are of a delocalized nature. However, compounds **11a** and **11b** have quaternary amines which are purely sp^3 in nature, which creates opportunities for pure electrostatic interactions along with hydrocarbon-based chains providing hydrophobicity. Compound **15** also has similar aspects in a polystyrene backbone.

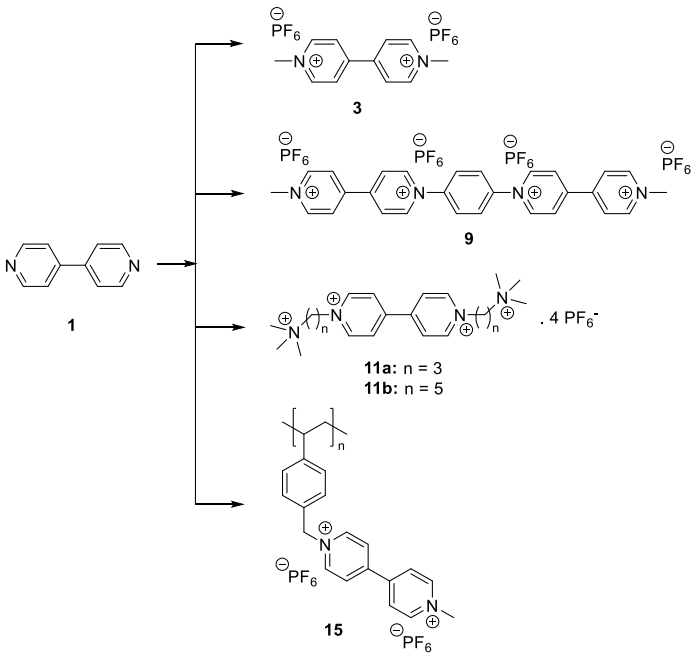

Scheme 4.1. *Viologen derivatives and their precursor 4,4'-bipyridine (**1**).*

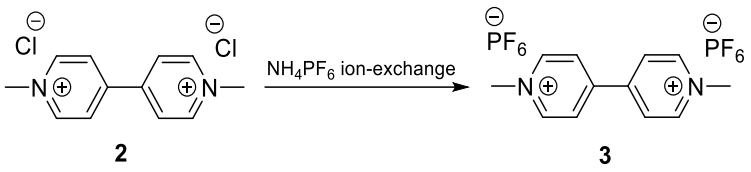

Scheme 4.2. *Synthesis of compound **3**.*

Compound **3** was prepared by exchanging the counter anions of a commercially available methyl viologen dichloride to hexafluorophosphate (Scheme 4.2). To synthesize **9** (Scheme 4.3), a Zincke salt was prepared by compound **1** with 1.1 equivalents of **4** in ethanol under reflux conditions for 23 hours. The resulting salt (**5**) upon reacting with 1,4-phenylenediamine (**6**) in ethanol under reflux conditions yielded the chloro-derivative (**7**). Purification of **7** required attention and can only be done by exchanging the counter anions to hexafluorophosphate followed by precipitation using acetonitrile:DCM (1:2). The resulting compound **8** was soluble in solvents such as acetonitrile, acetone, etc., compared to **7** being soluble in methanol, ethanol, water and insoluble in acetonitrile and acetone. Compound **9** was synthesized by methylation of **8** using methyl iodide in acetonitrile under reflux conditions, followed by an ion-exchange to hexafluorophosphate.

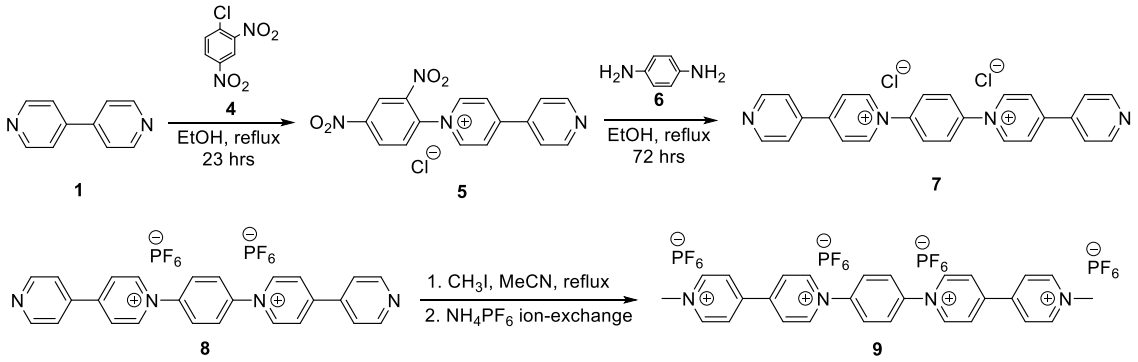

Scheme 4.3. *Synthesis routes compound **9** by preparing the Zincke salt, followed by Zincke reaction and methylation.*

The alkyl chain derivatives were synthesized by reacting **1** with **10a** and **10b** (Scheme 4.4) in DMSO followed by anion exchange to hexafluorophosphate (**11a** and **11b**).

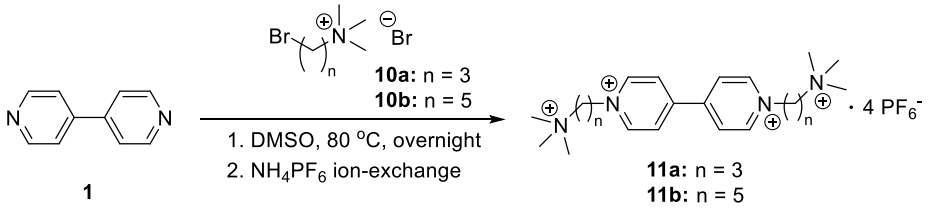

Scheme 4.4. *Schematic synthesis for alkylated bipyridinium derivatives with terminal quaternary amines (with carbon chain lengths of 3C and 5C).*

Strategies for polymer based on viologens

Mono-methylation of **1** was performed by one equivalent iodomethane in acetone under a reflux condition. A general trend from previous observation was that the halo-salts of pyridinium were soluble in solvents like methanol, ethanol, water, etc., but insoluble in acetone and acetonitrile. Hence, low impurity for the mono-methylated product **12** was achieved by performing the reaction in acetone since precipitation of **12** in acetone pushes the reaction forward and inhibits further reaction forming a di-methylated product. S_N2-type substitution of **13** by **12** followed by anion exchange yields **14**. The polymerization was performed using $K_2S_2O_8$ as the initiator, at 80 °C over 4 days in DMSO, yielding **15** (Scheme 4.5).

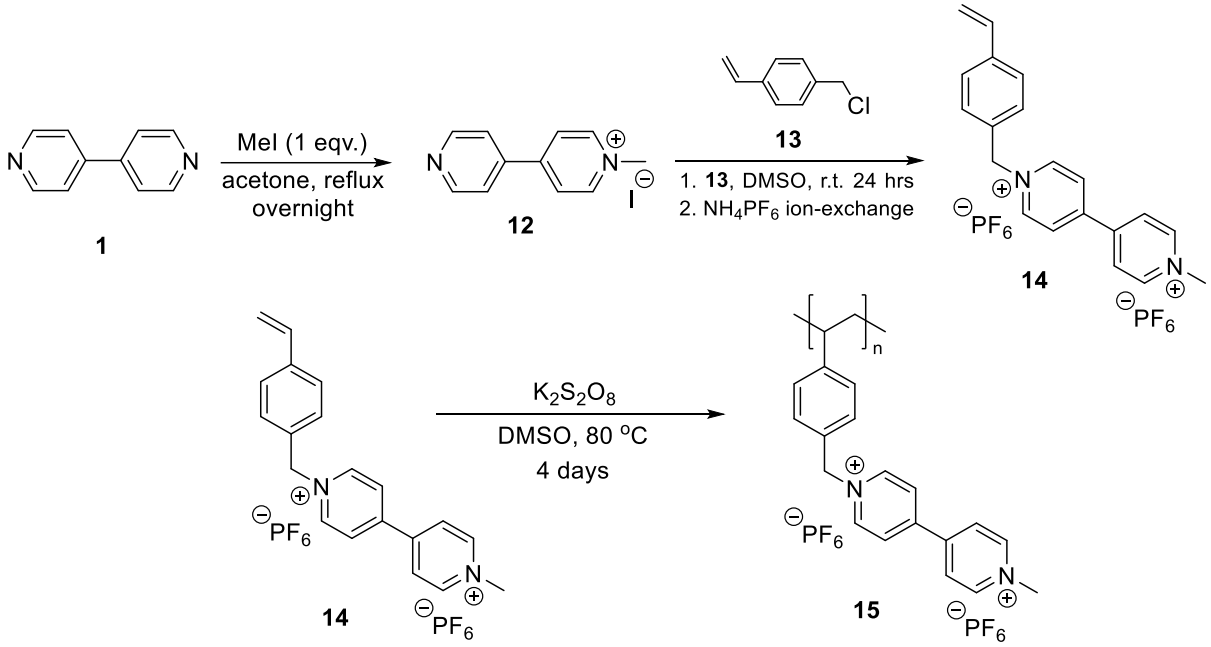

Scheme 4.5. *Synthetic scheme for viologen-based polymer **15** with alkyl chain as a backbone. (For the conversion of **1** to **12**, more than 1 equivalent of methyl iodide has been used, however, due to the very low solubility of **12** in acetone, the mono-substituted product precipitates and the reaction is terminated before further substitution).*

Strategies for pyrene-4,5,9,10-tetrone derivatives

The electron deficient system with a pyrene backbone (**23**) could be synthesized from Suzuki coupling in two different ways: either between a boronic ester derivative of pyrene-4,5,9,10-tetrone and bromo-derivatives of pyridine (Path A, Scheme 4.6) or between a dibromo-derivative of pyrene-4,5,9,10-tetrone and boronic acid/ester- derivatives of pyridine (Path B, Scheme 4.6). Pyrene-4,5,9,10-tetrone (**17**) was synthesized from pyrene (**16**) by a well-known IO_4^- based oxidation reaction with $RuCl_3$ as the catalyst in a ternary mixture of solvents (dichloromethane, acetonitrile and water in a ratio of 4:4:5).

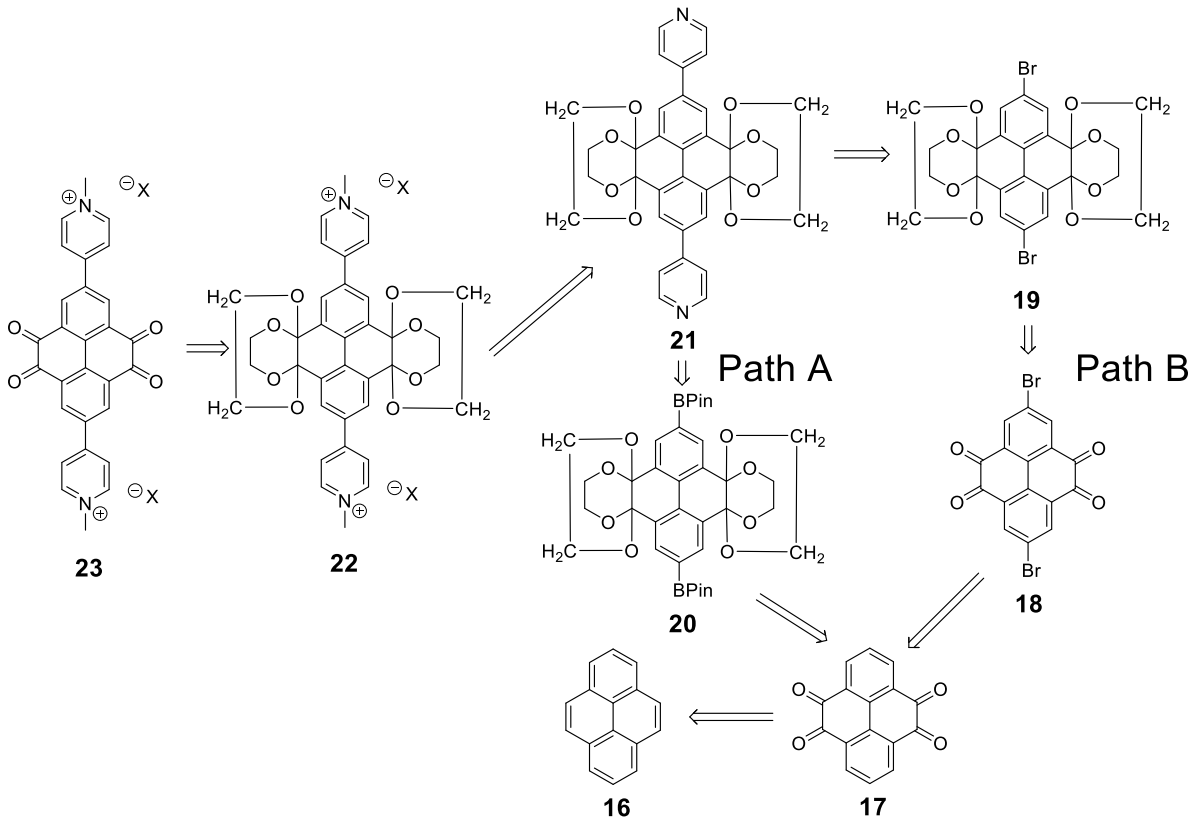

Scheme 4.6. *Retrosynthetic pathways for the pyrene-4,5,9,10-tetrone derivative* ***23****.*

Higher valent ruthenium oxide species are the catalysts for oxidation and have been known to be sluggish and incomplete in the absence of acetonitrile as a co-solvent. Addition of acetonitrile helps in keeping the relative content of the active species high by coordinating with the lower valent ruthenium species inhibiting the coordination with byproducts (carboxylic acids), allowing the regeneration of the catalyst.[82] The double bromination at the 2,7- positions was achieved by *N*-bromosuccinimide in concentrated sulfuric acid environment to yield **18** (Scheme 4.7).

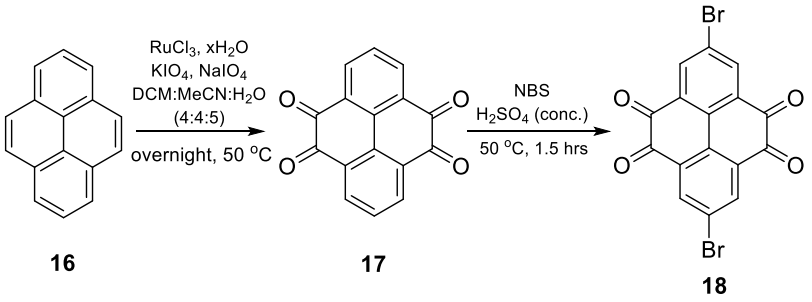

Scheme 4.7. *Synthetic routes for 2,7-dibromopyrene-4,5,9,10-tetraone (****18****) from pyrene.*

The tetra-ketone system **18** cannot yield the desired product upon Suzuki coupling, potentially due to the deactivation of the Pd-based catalyst; hence, the protection of the tetra-ketone is necessary. The protection of **18** was performed using ethylene glycol catalyzed by *p*-

toluenesulphonic acid in refluxing toluene. The coupling was then performed between **19** and 4-pyridinylboronic acid catalyzed by XPhos-Pd-G2 (Scheme 4.8) in a typical Suzuki coupling setup with a binary mixture of solvents (1M aq. Cs_2CO_3 and THF with a 1:1 ratio) under a nitrogen environment to yield **21**.

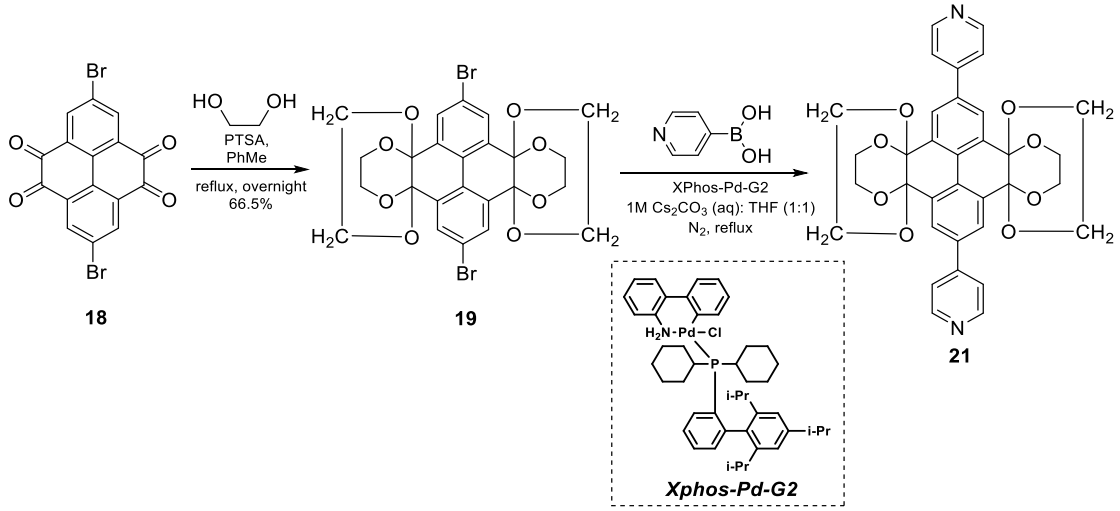

Scheme 4.8. *Synthetic routes for the keto-group protection followed by a Suzuki-coupling step.*

Compound **22** was prepared by di-methylation of **21** and TFA:H_2O (9:1) was employed to deprotect the ketal on **22**. However, no clear indication of purity or complete conversion has been obtained so far, for compound **23**. (Scheme 4.9).

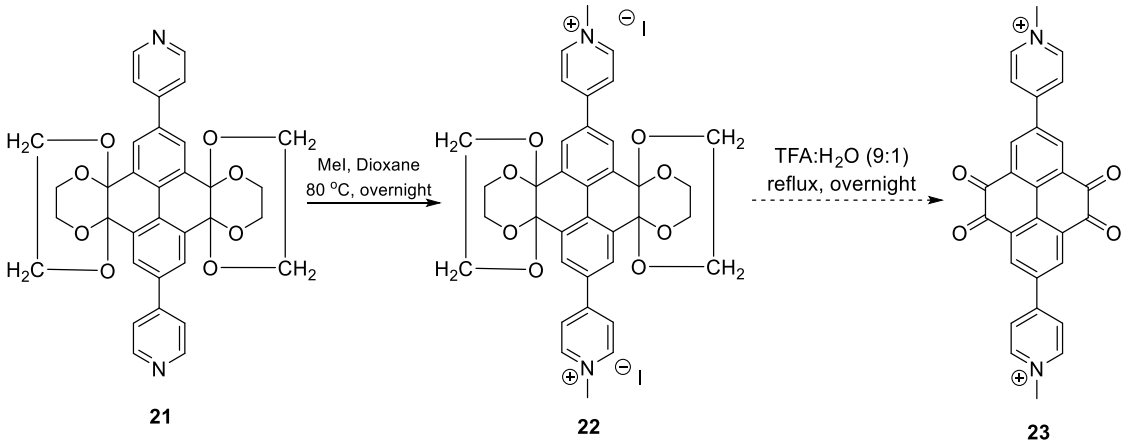

Scheme 4.9. *Synthetic routes for methylation followed by the deprotection of the keto-groups.*

Theoretical characterization of BPNSs hybrid systems with compounds 3 and 9

The properties of the viologen derivatives (**3** and **9**) and their behavior upon interacting with BPNS were investigated theoretically with the help of density functional theory (DFT) calculations. All first-principles calculations were implemented using the Vienna ab initio simulation package (VASP). The Perdew, Burke, and Ernzerhof (PBE) functional of

generalized gradient approximation (GGA) served to approximate exchange-correlation functions and the projector-augmented wave (PAW) method was used to represent the core-valence electron interactions.[83] The frontier molecular orbitals of **3** and **9** were calculated first. The highest occupied molecular orbitals (HOMO) were found to be −2.65 eV and −2.63 eV, and the lowest unoccupied molecular orbitals (LUMO) were found to be −0.94 eV and −1.25 eV for **3** and **9** respectively. The bandgaps for compounds **3** and **9**, hence calculated, were 1.7 eV and 1.38 eV, respectively.

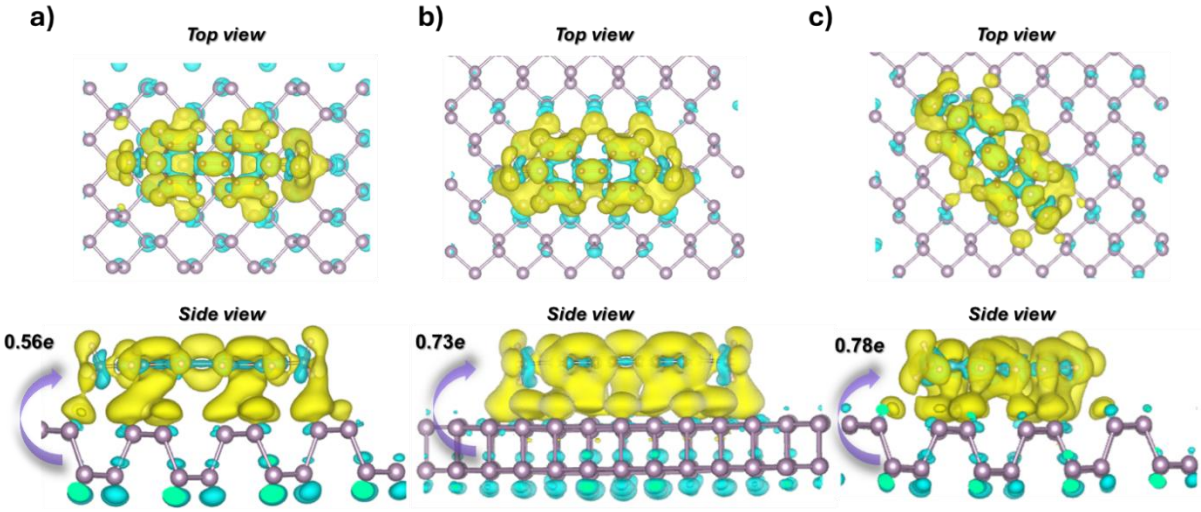

Figure 4.1. *Charge-difference plots of the molecule **3** on top of a single-layer BPNS surface. (a) perpendicular to the ridge, (b) parallel to the ridge, (c) diagonal to the ridge. Orbital overlap scenarios for the **3**-BPNS hybrids in each direction are shown as the side view located under each consecutive illustration. The yellow region represents areas of electron accumulation, while the cyan region indicates areas of electron depletion.*

Table 4.1. Total and average adsorption energy of the **3**-BPNSs hybrids along different directions from the ridges of BPNSs calculated by DFT.

Materials [3-BPNSs]	**E_{ads} (eV)**	**Number of atoms**	**E_{ads}/X (eV)**
Perpendicular	−1.45	28	−0.0518
Parallel	−1.47	28	−0.0524
Diagonal	−1.44	28	−0.0516

Normalized adsorption energies while interacting with a single-layer BPNS surface, were calculated for **3** and **9** in parallel, perpendicular and diagonal direction to the ridges of BPNSs

(Figure 4.1 and 4.2). For both compounds, the normalized adsorption energy is greater in the parallel direction, and the orbital overlap is also maximum in the parallel direction (Figure 4.1 and 4.2 for **3** and **9**, respectively). It is noteworthy that the normalized adsorption energy value was found to be lower for compound **9** (−0.0472 eV) compared to **3** (−0.0518 eV) (Table 4.1 and 4.2).

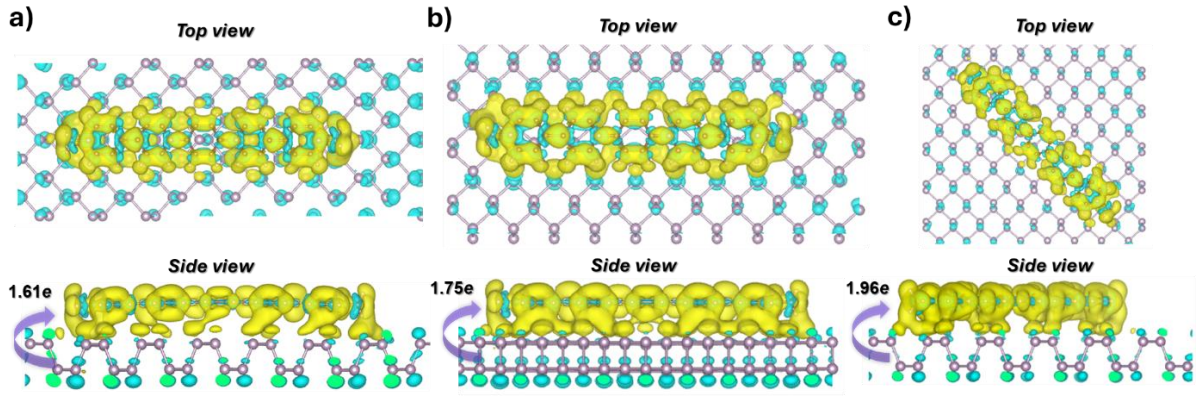

Figure 4.2. *Charge difference plots of the molecule **9** on top of a single-layer BPNS surface: (a) perpendicular to the ridge, (b) parallel to the ridge, (c) diagonal to the ridge. Orbital overlap scenarios for the **9**-BPNS hybrids in each direction are shown as the side view located under each consecutive illustration. The yellow region represents areas of electron accumulation, while the cyan region indicates areas of electron depletion.*

Table 4.2. Total and average adsorption energy of the **9**-BPNSs hybrids along different directions from the ridges of BPNSs calculated by DFT.

Materials [9-BPNSs]	**E_{ads} (eV)**	**Number of atoms**	**E_{ads}/X (eV)**
Perpendicular	−2.74	58	−0.0472
Parallel	−2.83	58	−0.0487
Diagonal	−2.67	58	−0.0460

The orbital overlap picture also suggests that the interaction of the nanosheets with the small molecules were possibly a type of cation-induced dipole interaction. In the parallel configuration, both molecules were predicted to have a partial charge-transfer, which was measured to be 0.73*e* and 1.75*e* for the **3**-BPNS and **9**-BPNS hybrids, respectively (Figures 4.1 and 4.2).

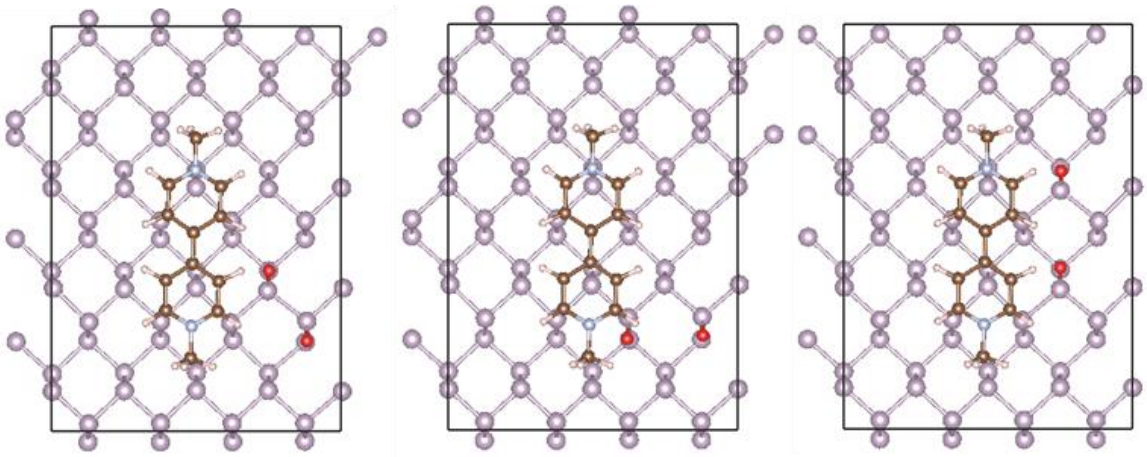

Figure 4.3. *Structures of O_2 after adsorption at different sites on **3**-BPNS.*

Oxygen adsorption on the nanosheets is one of the key phenomena and provides a deep insight into the degradation pathway of the nanosheets under ambient exposure. One of the key events during the process is immediate dissociation of oxygen molecules into atoms[84] on the nanosheet surface and the free energy of adsorption for the oxygen atoms (Figure 4.3) onto the nanosheet surface is a very crucial parameter for evaluating the ease of BPNS oxidation.

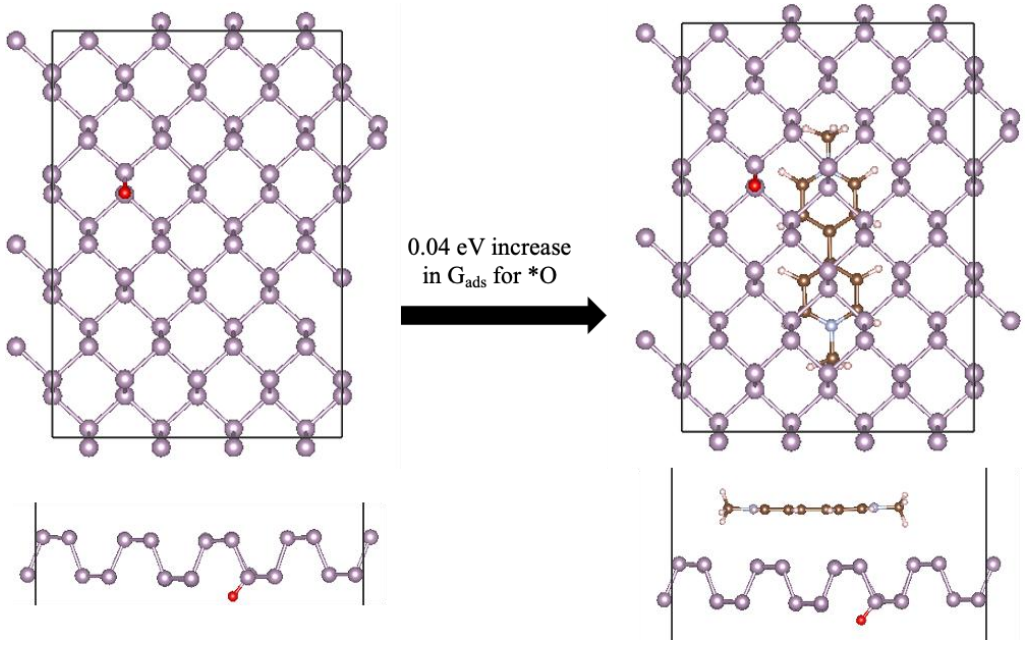

Figure 4.4. *The calculated adsorption-free energy increased by 0.04 eV for the **3**-BPNS hybrid, compared to the pure BPNS. Increment in free energy of adsorption usually implies energetically less favorable i.e. weaker binding to the surface. Here, the increment suggests that the adsorption of oxygen atom is comparatively less favorable once the compound **3** is adsorbed onto the nanosheet surface.*

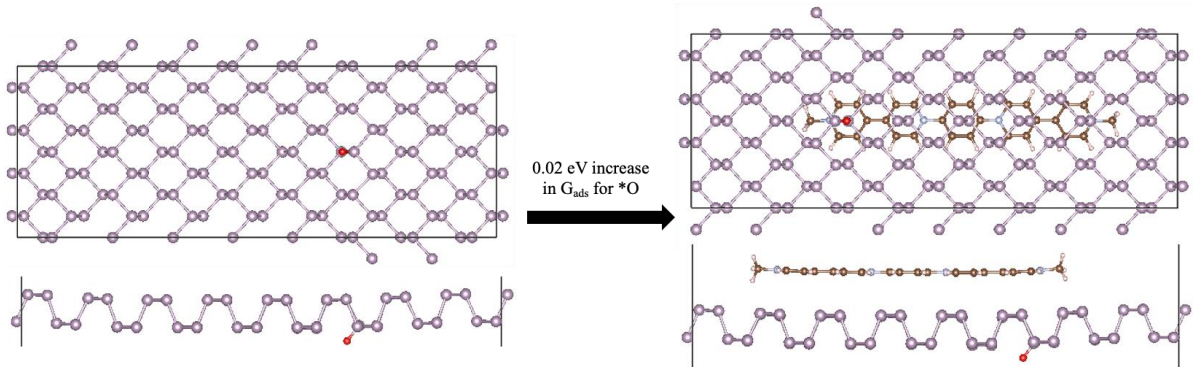

Figure 4.5. *The calculated adsorption free energy increased by 0.02 eV for the* ***9****-BPNS hybrid, compared to the pure BPNS. Here, the increment suggests that the adsorption of oxygen atom is less favorable once the compound* ***9*** *is adsorbed onto the nanosheet surface but will comparatively be stronger than the case of compound* ***3****.*

The Gibbs free energy for the adsorption of the oxygen atoms was calculated for the surfaces of pure BPNSs, **3**-BPNS and **9**-BPNS hybrids. Interestingly, the Gibbs free energy was calculated to be increased by 0.04 (Figure 4.4) and 0.02 eV (Figure 4.5) for the **3**-BPNS and the **9**-BPNS hybrids respectively, compared to that of pure BPNSs (possibly due to lesser electron density onto the exposed nanosheet surface). This suggests the more favorable and spontaneous nature of the oxidation process on the pure BPNSs, whereas the hybrids are comparatively less prone to oxidation (**3**-BPNS being the least prone). The calculations were performed for one-atom-adsorption scenario and did not consider the following: the excitonic pairs generated on the nanosheets under light exposure and the charged superoxide radical anion species formed through electron transfer from the conduction band of the nanosheets to the molecular oxygen.

Photophysical studies of BPNSs hybrid systems with compounds **3** and **9**

BPNSs were titrated with gradual addition of the small molecules, and the process was monitored using UV-vis spectrometry. Molecular absorbance was checked for compounds **3** and **9**. The peak absorbances were found at 257 nm (Figure 4.6a) and at 287 nm (Figure 4.6b) for compounds **3** and **9**, respectively. Upon addition of the compounds **3** and **9** (1 mg ml^{-1} for both solutions) to a fixed amount of a BPNS dispersion (a 1.75 mL of a 0.143 mg ml^{-1} dispersion for **3** and a 1.7 ml of a 0.118 mg ml^{-1} dispersion for **9**), red shifts in the molecular absorptions were observed. The new peak absorbances for the hybrids systems were found to be at 259 nm (Figure 4.6a) for compound **3** and at 291 nm (Figure 4.6b) for compound **9**, respectively. The decrease in characteristic BPNS absorption upon addition of compound **3** can be attributed to the reduced aggregation tendency of nanosheets dispersed in the solvent. In contrast, with compound **9** the decrease in absorption stabilized and no precipitation was observed, likely due to slower aggregation and the possible presence of a dynamic adsorption–desorption process.

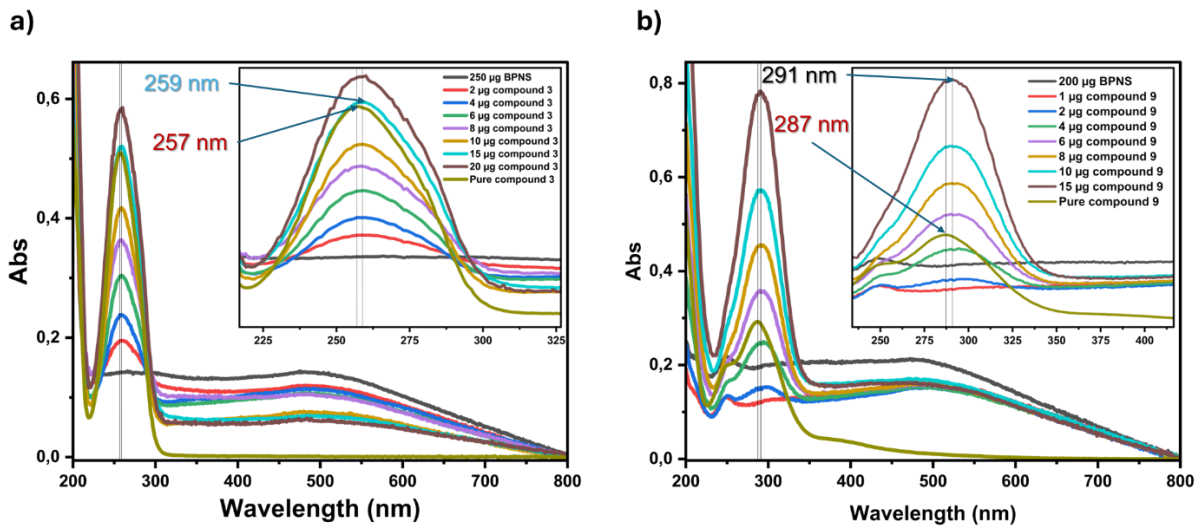

Figure 4.6. *Titrimetric studies indicate the interaction between the viologen derivatives and BPNSs as observed through UV-vis absorption measurements. BPNSs were titrated using (a) compound **3** and (b)compound **9**. The absorbance of a 3.01 ml solution of a 0.0138 mg ml^{-1} of compound **3** in acetonitrile was measured for comparison in (a). The absorbance of a 1.55 ml solution of a 0.0045 mg ml^{-1} compound **9** in acetonitrile was measured for comparison (b). The shifts in the peaks for the hybrids were compared against the absorption of the compound **3** (inset of (a)) and **9** (inset of (b)) in their pure form.*

Formation strategies for BPNSs hybrid systems with compounds **3** and **9**

Compound **3** provided a comparatively faster precipitation rate than compound **9** with BPNSs in low concentration in acetonitrile media during UV-titration. At higher concentrations, when the dynamics is known to be unpredictable, the aggregation kinetics was slower for the **9**-BPNS hybrid and possibly involving dynamic adsorption-desorption processes while the **3**-BPNS hybrid exhibited consistent behavior. Hence, the **3**-BPNS hybrid can easily be prepared by precipitation and removal of the solvent by centrifugation, whereas the **9**-BPNS hybrid was prepared by adding an excess of compound **9** and evaporating the solvent under nitrogen flow, resulting in inhomogeneity within the hybrid.

Characterization of BPNSs hybrid systems with compounds **3** and **9**

The hybrid systems of BPNSs with **3** and **9** have been characterized through several characterization techniques. IR and Raman spectroscopy provided a deep understanding of the interaction, and the morphology of the hybrid systems was observed using electron microscopy techniques (SEM, TEM & HR-TEM).

IR

FTIR spectra of both the compounds in its salt form were compared to the pure BPNSs and the hybrids formed using attenuated total reflectance (ATR) measurements. Molecular stretching and bending modes observed in both the cases can also be traced in the hybrid systems.

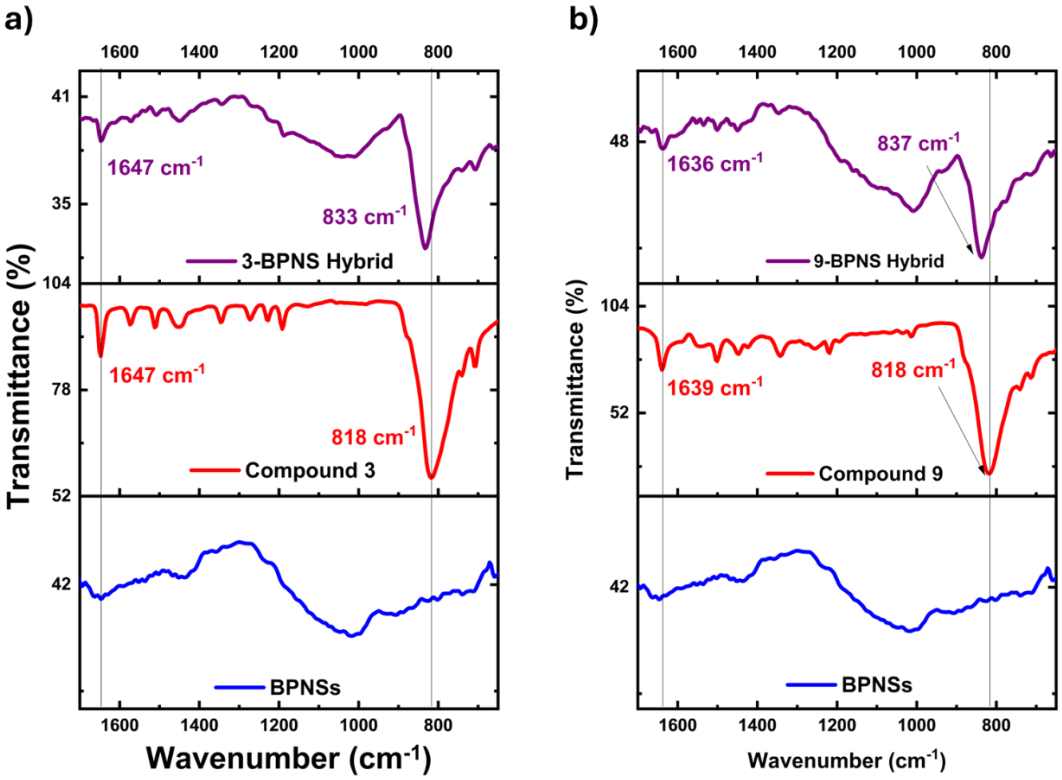

Figure 4.7. *ATR-FTIR studies indicate the interactions between the molecules and BPNSs, (a) with compound **3** and (b) with the compound **9**. In each figure the pure nanosheets and the pure molecule were compared with the spectrum of the hybrid systems.*

The most noticeable peak for both the molecules around 818 cm^{-1} can be assigned to the C-H out-of-plane bending mode generated by the methyl groups attached to the terminal nitrogen atoms forming the pyridinium ions. The peak position was found to be shifted to 833 cm^{-1} for the hybrid of **3** (Figure 4.7a) and to 837 cm^{-1} for the hybrid of **9** (Figure 4.7b). The blue-shifts, thus observed, were an indication of restriction in the out-of-plane bending modes of the methyl groups due to their stacking nature on the BPNS surface, which in turn indicates the interaction between the molecules and the nanosheet surface.

Raman

In the mean Raman spectra of pure BPNSs, three sharp peaks could be observed at 362 cm^{-1}, 437 cm^{-1} and 468 cm^{-1}, corresponding to the out-of-plane symmetric phonon mode A^1_g and the in-plane modes B_{2g} and A^2_g, respectively. The average Raman spectra for the hybrids also show the respective peaks at around 362 cm^{-1}, 438 cm^{-1} and 464 cm^{-1} for the hybrid samples with **3** and at around 358 cm^{-1}, 434 cm^{-1} and 460 cm^{-1} for the hybrid samples with **9** (Figure 4.8). The average spectra were derived from over 20 measurements for each sample and the A^1_g to A^2_g intensity ratios were calculated for all the three samples. The A^1_g to A^2_g intensity ratio is a measurement for aerobic oxidation and was found out to be 0.719, 0.716 and 0.693 for the pure BPNSs, **3**-BPNS and **9**-BPNS hybrids, respectively, indicating minimal oxidation throughout the hybrid preparation steps.

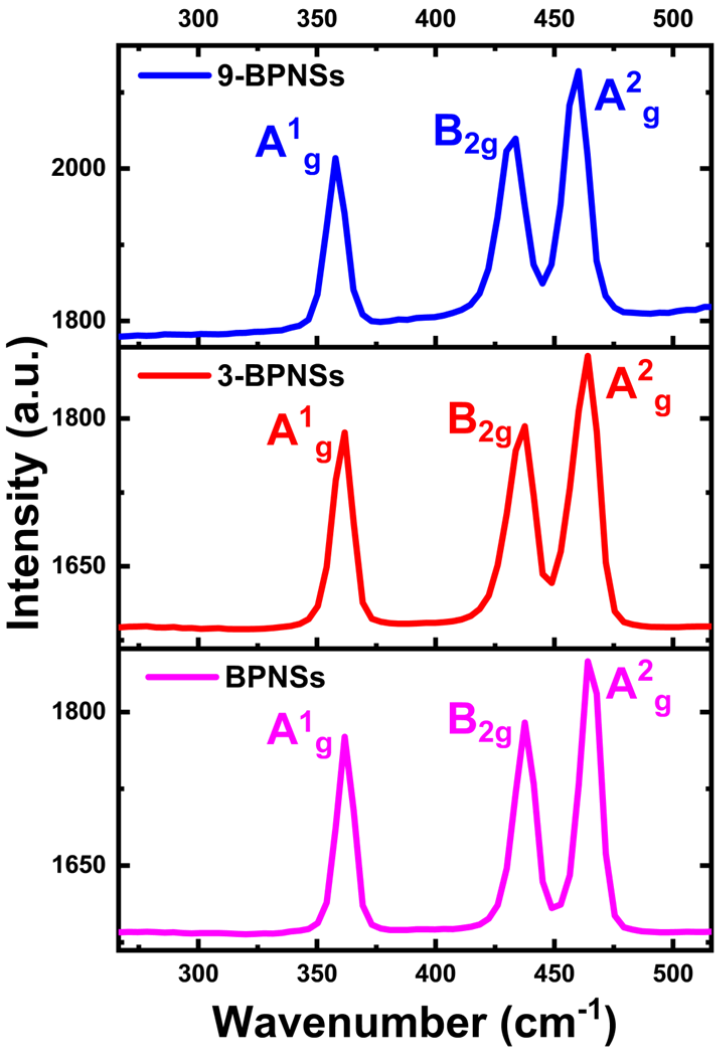

Figure 4.8. *Mean Raman spectra measured using a 532 nm laser excitation for the hybrids compared to the pure BPNSs. The out-of-plane symmetric phonon mode A^1_g and the in-plane modes B_{2g} and A^2_g are preserved in the hybrid samples.*

SEM

The morphology of the hybrids was investigated using scanning electron microscopy (SEM) and was compared against that of the bare nanosheets (Figure 4.9a, 4.9d) and the viologen derivatives (Compounds **3** and **9**, Figure 4.9c and 4.9b). Solid block-like features for both **3** and **9** with additional rod-like structures in **3** represent the crystalline structure of the viologen derivatives, whereas the flake-like structures confirm the 2D nature of the few-layer BPNSs.

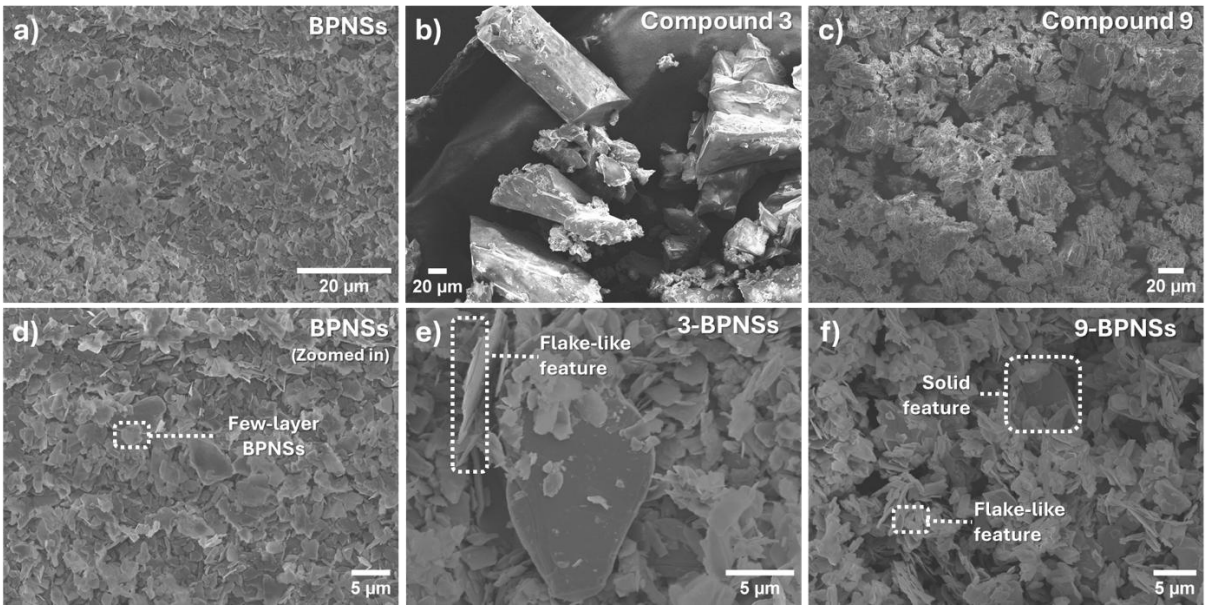

Figure 4.9. *SEM images of (a) BPNSs, (b) compound **3**, (c) compound **9**, (d) BPNSs (zoomed in), (e) **3**-BPNS hybrid and (f) **9**-BPNS hybrid.*

Both the hybrids showed flake-like features along with occasional large solid structures scattered throughout the samples (comparatively more in case of **9**-BPNS (Figure 4.9f), due to the higher requirement of molecule **9** for the hybrid preparation), indicating that the overall morphology has not been altered significantly after noncovalent functionalization.

TEM

TEM and HR-TEM measurements were performed on the samples for a closer look at the morphology, especially on the lattice parameters of the nanosheets. Lattice fringes for the bare nanosheets can be observed in the HR-TEM images with a d-spacing of about 2.5 Å and 2.2 Å for the (111)[85] plane and (014)[47] plane, respectively (Figure 4.10d). The (111) plane of the BPNSs can be traced to the **3**-BPNS hybrid, having a d-spacing of 2.5 Å (Figure 4.10e), implying unaffected crystallinity of BPNSs in the hybrid. The (014) plane can be observed in the case of the **9**-BPNS hybrid with a d-spacing of 2.2 Å (Figure 4.10f).

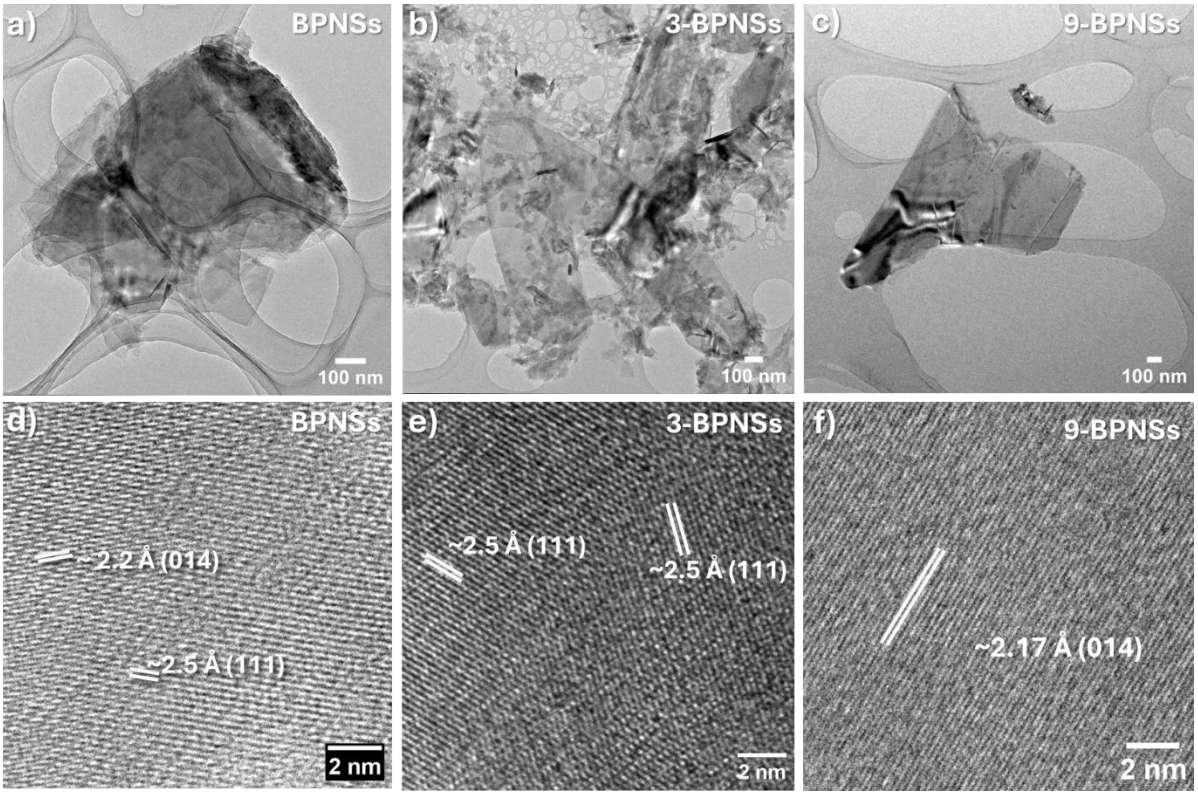

Figure 4.10. *TEM and HR-TEM images of (a,d) BPNSs, (b,e) the* ***3****-BPNS hybrid and (c,f) the* ***9****-BPNS hybrid.*

Interestingly, the aggregated nature of the **3**-BPNS hybrid can be observed in the TEM images (Figure 4.10b) but the **9**-BPNS hybrid did not show any aggregated morphology (Figure 4.10c). This essentially implies that the **9** molecules cannot be captured by TEM-grid in the solution phase leaving behind mostly bare nanosheets onto the carbon grid due to their lower adsorption energy onto the nanosheets and slower aggregation kinetics.

Ambient stability studies of BPNSs hybrid systems with compounds **3** and **9**

The protection efficiency of the small molecules on the BPNS-hybrids was monitored using X-ray photoelectron spectroscopy (XPS) studies. The control experiment involves preserving the bare BPNSs and both the hybrids under inert nitrogen environment for 6 days. Another group of the same samples was exposed to ambient conditions for the same time interval, and the experiment was repeated several times to ensure repeatability. The core level P2p intensity was plotted against the binding energy and each spectrum for the samples in the protected condition can be deconvoluted into four peaks at 129.69, 130.53, 133.23, 134.47 eV for the bare BPNSs (Figure 4.11a, Table 4.3), at 129.62, 130.46, 133.35, and 134.24 eV for the **3**-BPNS hybrid (Figure 4.11c, Table 4.3) and at 129.63, 130.47, 133.38, 134.28 eV for the **9**-BPNS hybrid (Figure 4.13a, Table 4.4), which can be assigned to $P2p_{3/2}$, $P2p_{1/2}$, P-O and P=O peaks. For the samples kept under ambient conditions, the $P2p_{3/2}$, $P2p_{1/2}$, P-O and P=O peaks can be observed at 129.71, 130.55, 132.83, 133.97 eV for the bare BPNSs (Figure 4.11b, Table 4.3), at 129.73, 130.57, 133.39, 134.30 eV for the **3**-BPNS hybrid (Figure 4.11d, Table 4.3) and at 129.04, 129.88, 133.31,134.28 eV for the **9**-BPNS hybrid (Figure 4.13b, Table 4.4). However, in the

case of the **9**-BPNS hybrid, an additional peak (Figure 4.13, Table 4.4) can be observed at 136.57 eV for the protected sample (Figure 4.13a, Table 4.4) and at 136.18 eV for the sample stored under the ambient condition (Figure 4.13b, Table 4.4), which can be assigned to the P-F peak. This peak originates from the PF_6^- anion present in molecule **9** during the hybrid formation and could not be traced in the **3**-BPNS hybrid due to the low requirement of **3** for the hybrid preparation.

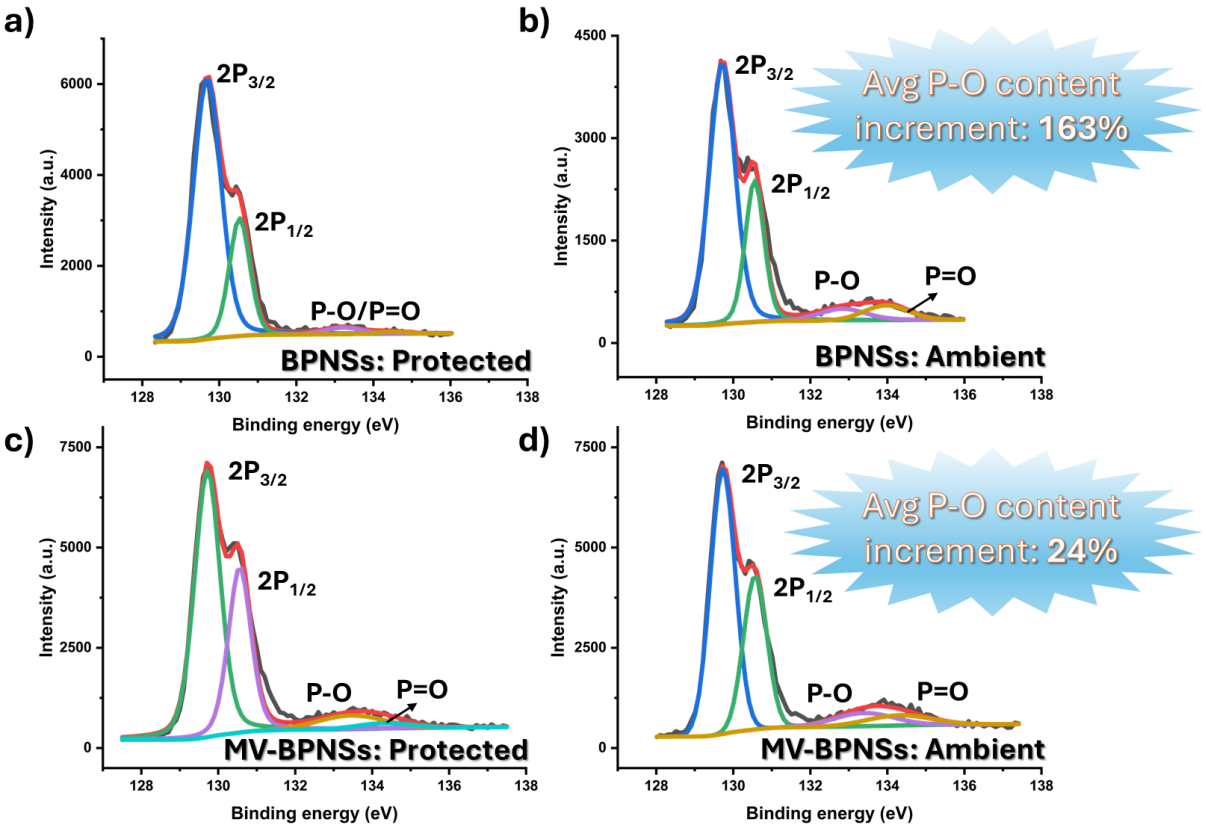

Figure 4.11. *P2p XPS spectra of (a,b) BPNS under protected and ambient conditions. (c,d)* ***3****-BPNS hybrids under protected and ambient conditions.*

Table 4.3. P2p binding energies of BPNSs and **3**-BPNS in XPS measurements.

Binding Energy	**BPNS-P (eV)**	**BPNS-A (eV)**	**3-BPNS-P (eV)**	**3-BPNS-A (eV)**
$P2p_{3/2}$	129.69	129.71	129.62	129.73
$P2p_{1/2}$	130.53	130.55	130.46	130.57
P–O	133.23	132.83	133.35	133.39
P=O	134.47	133.97	134.24	134.30

P-protected, A-ambient

Table 4.4. P2p binding energies of the **9**-BPNS hybrid in XPS measurements.

Binding Energy	**9-BPNS-P_1 (eV)**	**9-BPNS-P_2 (eV)**	**9-BPNS-A_1 (eV)**	**9-BPNS-A_2 (eV)**
$P2p_{3/2}$	129.63	129.04	129.84	129.74
$P2p_{1/2}$	130.47	129.88	130.68	130.58
P−O	133.38	133.31	133.38	133.33
P=O	134.28	134.28	134.28	134.23
P-F	136.57	136.18	136.73	136.92

P-protected, A-ambient

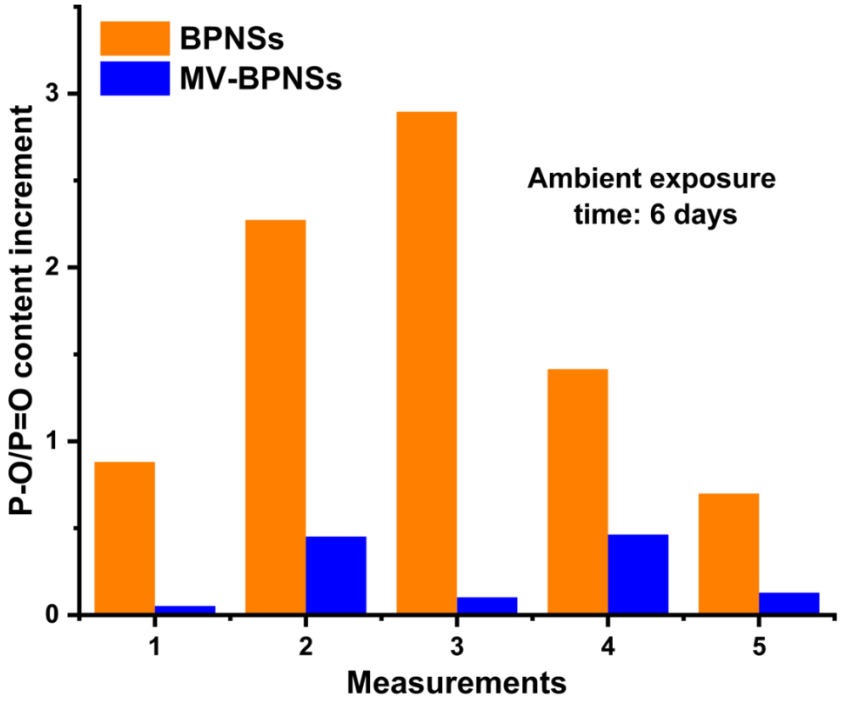

Figure 4.12. *A comparison of the extent of oxidation between BPNSs and the* ***3****-BPNS hybrids in various measurements over 6 days of ambient exposure.*

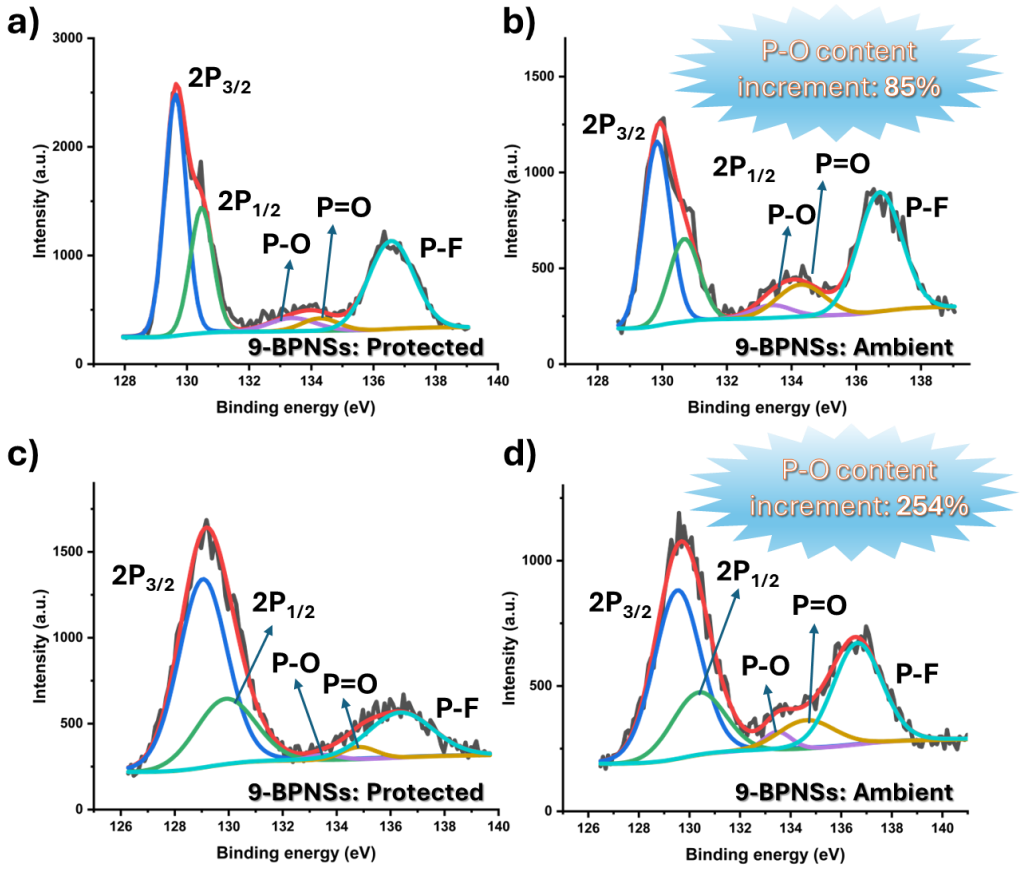

Figure 4.13. *P2p XPS spectra of the* ***9****-BPNS hybrid under (a,c) protected and (b,d) ambient conditions. The increase in the P-O/P=O content was compared under similar experimental conditions.*

Repeated measurements (comparison for each set of experiments was provided in Figure 4.12) showed a significant increment in the average P-O/P=O content in the pure BPNSs under the ambient exposure of 6 days (163%, Figure 4.11b), whereas the same for the **3**-BPNS hybrid had a very low average increment (24%, Figure 4.11d) under similar experimental conditions. The degree of noncovalent functionalization was calculated based on the atomic ratio between phosphorus and nitrogen from the N1s (Figure 4.14) spectra and was found to be one molecule of **3** for approximately every 21 phosphorus atoms. However, the increment in the P-O/P=O content for the **9**-BPNS hybrid was widely varied and showed a rise of 85% (Figure 4.13b) and up to 254% (Figure 4.13d) because of the sample inhomogeneity.

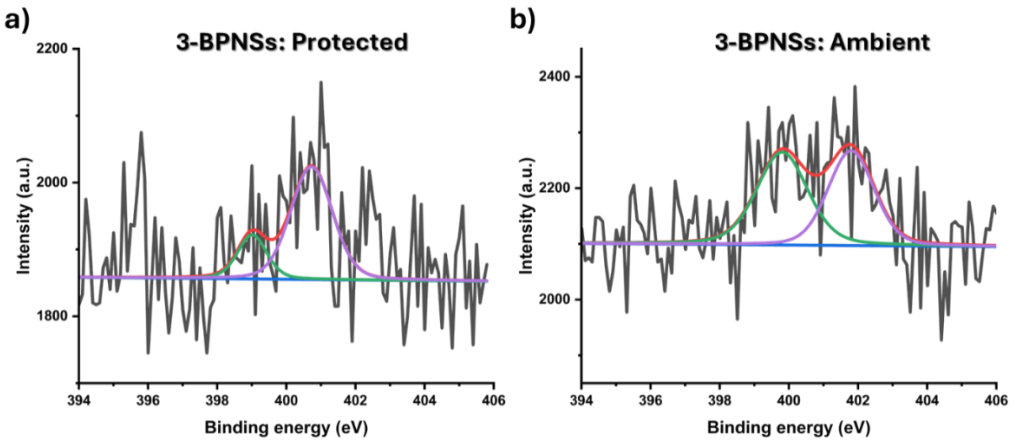

Figure 4.14. *N1s XPS spectra of* ***3****-BPNSs in (a) protected and (b) ambient conditions. The charged nitrogen (N+) and radical cation (N·+) generated during the X-ray exposure in the XPS chamber can be assigned to 400.7 eV and 399 eV for the protected hybrid and 401.8 eV and 399.8 eV for the hybrid in ambient condition.*[86] *The sample preparation was performed in acetonitrile and the acetonitrile signal was not observed at 397.7 eV.*[87]

Studies of other viologen-based systems

Other viologen derivatives were successfully synthesized and preliminary characterizations were performed. Sample preparation steps are identical to that of the **3**-BPNS hybrid.

Titrimetric studies

The aggregate formation was investigated firstly by zeta potential studies. The polymer is positively charged with negatively charged chlorides as counter anions. Since small molecules and ions don't show zeta potential, the positive value of +30.9 mV can only be attributed to the positively charged polymer. Pure BPNS dispersions on the other hand show a zeta potential of –13.9 mV. The mass fractions of the nanosheets and the polymer were varied, and the zeta potential was measured for the hybrids. With the increment of mass fraction for the **15**-polymer, the mean zeta potential of the pure BPNSs was observed to be shifted towards more positive value (normalized intensity distribution provided in Figure 4.15a) and the charge neutralization point was observed at a mass fraction between 0.04 and 0.08. The mean zeta potential was further observed to increase with increment in mass fraction and finally converge towards the zeta potential value of the pure polymer. This suggests that the excess polymer, being electrostatically stabilized, may not contribute to further aggregation, leading instead to an increase in zeta potential characteristic of true polymer dispersion.

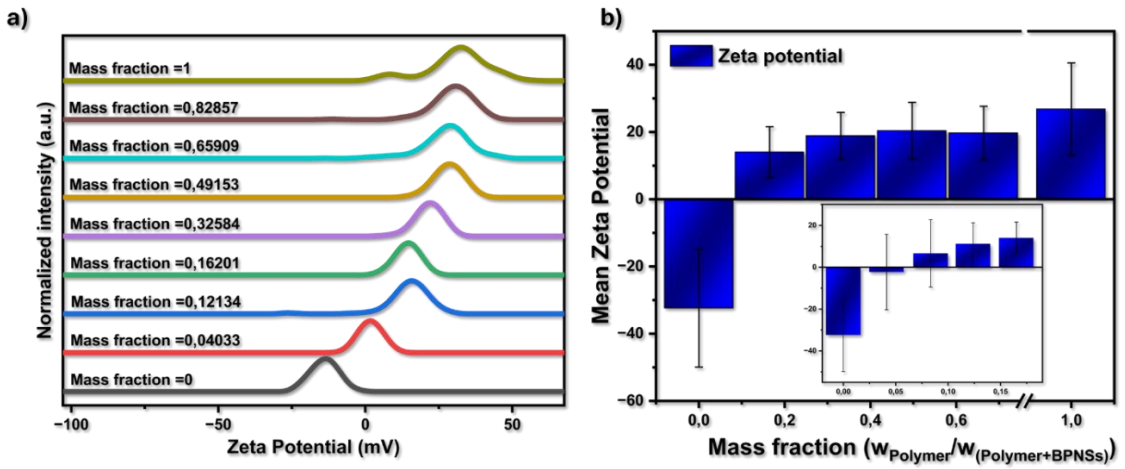

Figure 4.15. *Zeta potential studies for the* ***15****-BPNS hybrid systems, (a) changes in zeta potential plotted against the normalized intensity with the increment in polymeric mass fractions, (b) mean zeta potential increment with the increase in polymeric mass fractions (neutralization-point was achieved between the polymeric mass fraction of 0.04 and 0.08 (inset)).*

The polymeric viologen derivative was designed to include hydrophobic interaction alongside charge-induced dipole interaction (from the bipyridinium di-cation moiety, as discussed in the case for **3**-BPNSs) with BPNSs. The chloride derivative of the polymer **15** (i.e. **15-Cl$_x$**), hence, was measured for the peak absorbance, which was found to be around 258 nm (Figure 4.16, in water medium), and the position of the peak was found to be not changing while BPNSs were being titrated against the polymer. The scattering of the BPNSs was found to be dropping very fast with addition of the polymer **15** and after reaching a mass fraction of 0.056 (Figure 4.16, addition of 11.8 µg of **15-Cl$_x$**), the reduction of scattering was observed to converge. This, in turn, aligns with the finding in the Zeta potential studies about the charge neutralization point being achieved around a mass fraction of 0.04 and 0.08 and can also be correlated to the unstable dispersion, i.e., precipitation. No shifts in the peak positions are likely to be a consequence of purely electrostatic interaction with very little orbital overlap.

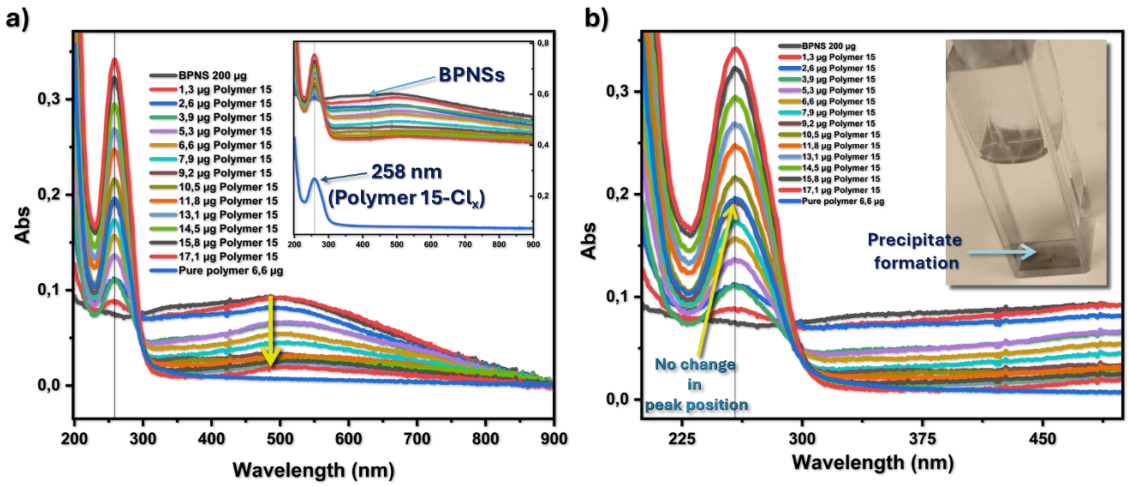

Figure 4.16. *Titrimetric studies indicate the interaction between the polymer* ***15-Cl$_x$*** *and BPNSs (200 µg, 2 ml) in water, as observed through UV-vis absorption measurements, (a)*

*lowering of scattering with the addition of **15-Cl$_x$** to the BPNS dispersion after zeroing (inset: original spectra without zeroing), (b) clear view of peak absorbances of the **15**-BPNS hybrids with no shift in peak positions as compared against the pure **15-Cl$_x$** (inset: precipitation was observed at the bottom of the cuvette).*

Vibrational characterization of hybrid systems

ATR-FTIR was performed on the hybrids based on **15**-BPNS hybrids to observe the interaction between the polymer and BPNSs. The aliphatic bending modes and the stretching modes of the polymer can be traced to the hybrid samples at 1639 (C=C stretch), 1560-1506 (C−C in ring stretch, aromatic), 1456 (C−H bend, alkane) and 1342 (C−N stretch, aromatic) cm^{-1} (Figure 4.16). The clear distinction of the aliphatic C−H out-of-plane bending modes (750-850 cm^{-1}) of the polymer cannot be observed in the hybrid, instead of which a new peak can be seen around 1118 cm^{-1} because of the aggregation of the polymer around the nanosheets which could be assigned to the out-of-plane bending modes in the new hybrid system (Figure 4.17).

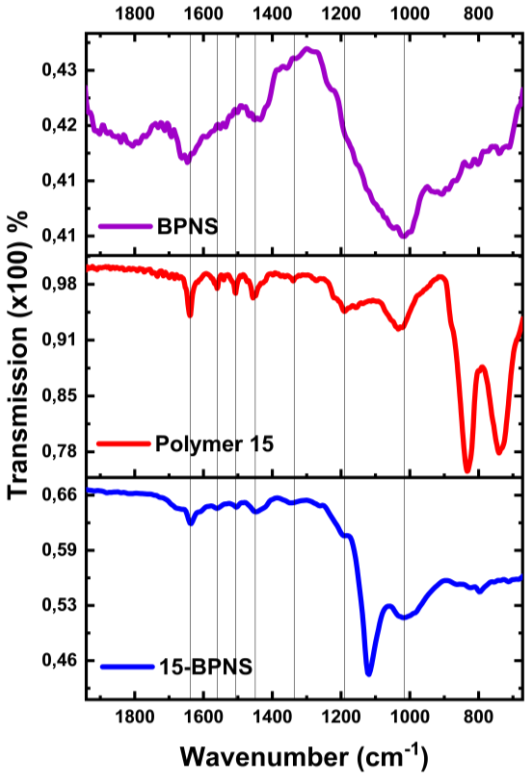

***Figure 4.17.** ATR-IR spectra of BPNSs, polymer-**15**, the **15**-BPNSs hybrid.*

Morphological studies

The morphology of the hybrids was characterized by SEM. The hybrid samples were prepared by grinding the BPNSs and the polymers in dry DMSO under constant nitrogen flow to avoid inhomogeneity in the samples. The dry samples for the SEM studies were obtained by evaporating the DMSO under high vacuum. The morphology of the hybrid samples was seen to contain amorphous polymeric depositions onto the nanosheet surfaces which were observed to be completely absent in the bare nanosheet surfaces. This indicates the formation of hybrid materials with the flake-like features of the nanosheets being retained.

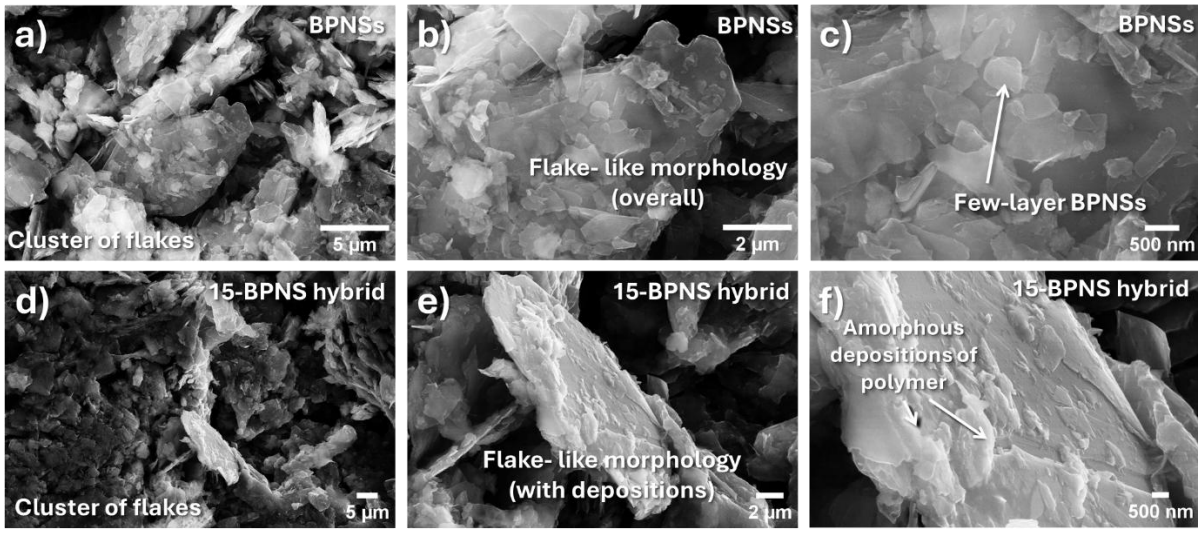

Figure 4.18. *SEM images of (a-c) BPNSs and (d-f) the* ***15****-BPNS hybrid. Flake-like morphology is present in both cases; in contrast, amorphous polymeric depositions can be observed for the* ***15****-BPNS hybrid (e,f).*

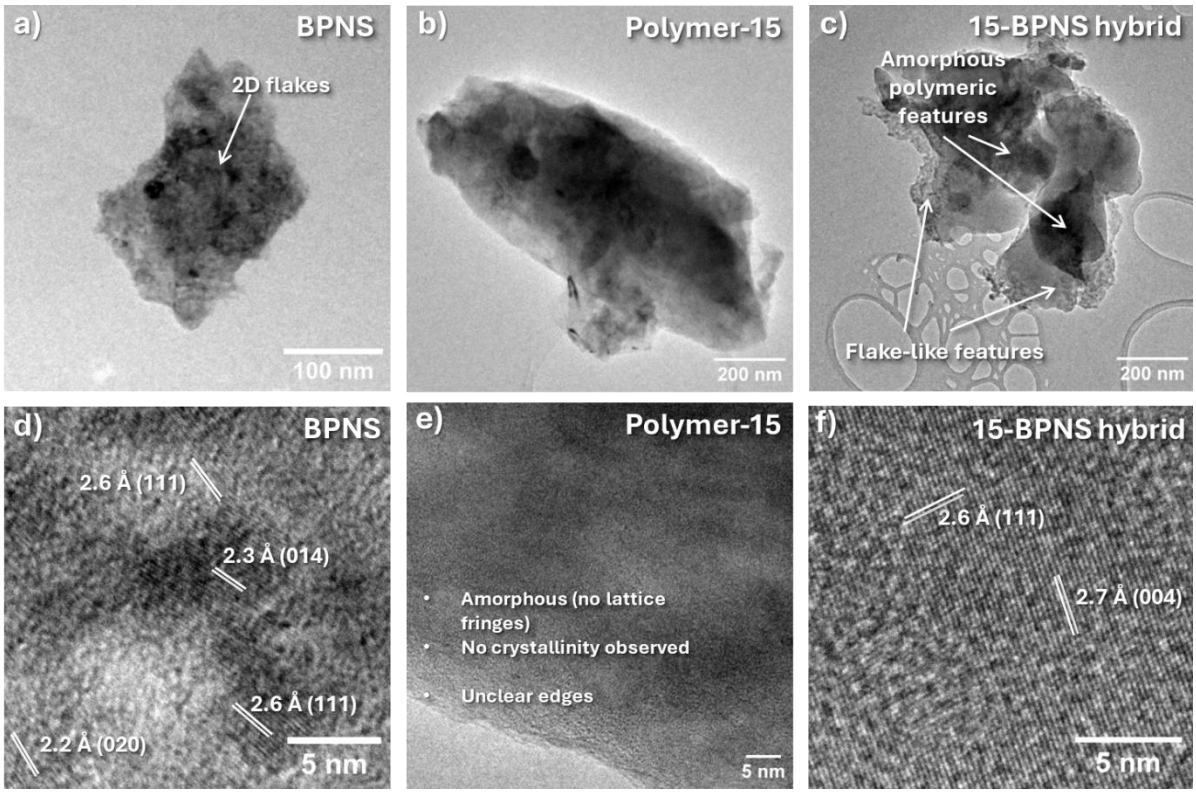

Figure 4.19. *TEM (a-c) and HR-TEM (d-f) images of (a,d) BPNSs, (b,e) polymer-****15*** *and (c,f)* ***15****-BPNS hybrids. The lattice fringes have been assigned by generating powder XRD patterns in VESTA using the crystallographic data provided by Hultgren et al.*[88]

Further morphological studies of the hybrid and the comparison against the pure BPNSs and the pure polymer-**15** were conducted by employing TEM and HR-TEM techniques. The hybrids could be observed to have depositions (Figure 4.19c) onto the BPNS surface where the lattice fringes were prominent (Figure 4.19f). These depositions were not observed onto the

pure nanosheets (Figure 4.19a, d) and the pure polymer was seen as amorphous solid (Figure 4.19b) with no observable lattice fringes (Figure 4.19e).

Ambient stability studies

Ambient stability efficiency was investigated using XPS studies and the $P2p_{3/2}$, $P2p_{1/2}$, P-O and P=O peaks can be observed at 129.79, 130.63, 133.51, 134.03 eV for the bare BPNSs (Figure 4.20a, table 4.5) and at 129.29, 130.13, 132.98, 134.26 eV for the **15**-BPNS hybrid (Figure 4.20c, table 4.5) preserved in the protected conditions. The $P2p_{3/2}$, $P2p_{1/2}$, P-O and P=O peaks can be observed at 129.82, 130.66, 133.43, 134.44 eV for the bare BPNSs (Figure 4.20b, Table 4.5) and at 129.50, 130.34, 133.38, 134.26 eV for the **15**-BPNS hybrid (Figure 4.20d, Table 4.5) stored in ambient conditions.

Table 4.5. P2p binding energies of BPNSs and **15**-BPNS in XPS measurements.

Binding Energy	BPNS-P (eV)	BPNS-A (eV)	15-BPNS-P (eV)	15-BPNS-A (eV)
$P2p_{3/2}$	129.79	129.29	129.82	129.50
$P2p_{1/2}$	130.63	130.13	130.66	130.34
P−O	133.51	132.98	133.43	133.38
P=O	134.03	134.26	134.44	134.26

P-protected, A-ambient

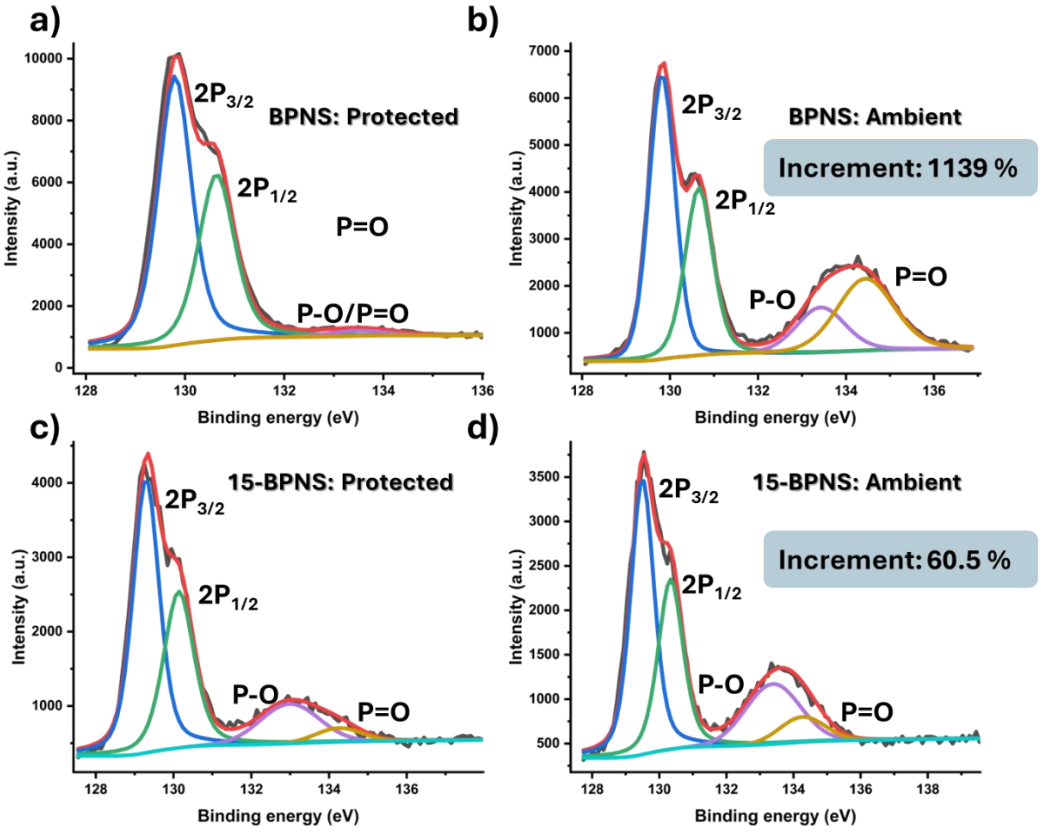

Figure 4.20. *P2p XPS spectra of (a,b) BPNS under protected and ambient conditions. (c,d) The* ***15****-BPNS hybrid under protected and ambient conditions.*

The extent of oxidation was determined by comparing the P-O/P=O content for both the samples after 6 days of exposure. The pure BPNSs sample had an overall increment of 1139 % in the P-O/P=O content, whereas the polymer- hybrid showed only 60.5 % of increment within the same exposure time. More experiments will be conducted to further validate the results.

Chapter 5

Conclusion and outlook

The thesis includes works that elaborate on a detailed study about the non-covalent functionalization of BPNSs by a series of cationic π-conjugated systems. The characterization of the hybrids provides us with some counter-intuitive facts which are crucial in understanding the hybrid systems and the physical parameters involved.

Two viologen derivatives, containing 2 and 5 aromatic rings, were successfully utilized to passivate the BPNS surface. DFT calculations predicted the normalized adsorption energy, which directly correlated with the interactions between the viologen molecules and the BPNS surface. Gibbs free energy oxygen adsorption was also calculated to be the highest for the **3**-BPNS hybrid, essentially referring to the low possibility of the hybrid system being oxidized. These interactions were further validated through UV-vis absorption, FTIR, and Raman spectroscopy. Surprisingly, despite its higher charge, compound **9** formed weaker hybrids with BPNSs than compound **3**, likely due to its lower average adsorption energy and slower aggregation kinetics.

The ambient stability efficiency was assessed through XPS studies by comparing the **3**-BPNS hybrid to pristine BPNSs under both protected and ambient conditions. While BPNSs exhibited significant oxidation, the **3**-BPNS hybrid showed notable protective efficiency, highlighting its potential as an effective stabilization strategy. In contrast, the **9**-BPNS hybrid displayed inhomogeneity, leading to an inconclusive protective effect.

Furthermore, hydrophobic viologens (**11a**, **11b**) and the polymer **15** were also successfully synthesized. Polymer **15** has been employed as a passivator, and preliminary studies has been conducted which also showed good protection efficiency. Morphological analyses confirmed the effective formation of the hybrid structure, supported by evidence from titrimetric measurements and vibrational characterization. These findings offer an opportunity to investigate the hydrophobic interactions between the polymers and the 2D material surface, despite the charged nature of the polymer environment.

The hypotheses behind the idea that the number of charges affects the interaction between the molecules and the nanosheets, was found to be more complex and needs further modification of the hypothesis itself. The basis of the modification must be based on the more parameters such as free energy availability, equilibrium criteria for aggregation and corresponding kinetics, types of hybridization of the atoms holding the charges (charges on sp^2 centers tend to be different from charges on sp^3 centers) etc. Electron deficiency, although, plays a crucial role in non-covalent interaction, structural parameters and constraints on molecular levels are also important in dictating aggregation kinetics, thus influencing the extent of functionalization.

Chapter 6

Acknowledgements

Firstly, I would like to thank my supervisor, Xiaoyan Zhang, for the guidance and continuous support. All the discussions with you have been a source of inspiration and motivation for me to become an independent and competent researcher.

Many thanks also go to my co-supervisor, Martin Rahm, and my examiner, Maria Abrahamsson, for their deep insights and expertise which helped me a lot in realizing the bigger picture of my project, in particular during the yearly study meetings.

Many thanks to friends and colleagues Cheng, Zenghua and Mangmang. You have been awesome and very fun to work with. I learned a lot from you and hope to keep on exchanging our ideas, knowledge and wits.

Floor 9 has been more than just a workspace—it has been my home. I have had the privilege of being surrounded by incredible colleagues, whose support, generosity, and encouragement have made my journey even more meaningful. While I cannot mention everyone with names, I deeply appreciate each of you for fostering a collaborative and welcoming environment that has made my time here so enjoyable and fulfilling.

Chapter 7

Appendices

Synthesis of compound ***5****:* 2,4-dinitrochlorobenzene (1 g, 0.0049 mol) and 4,4'-bipyridine (848.2 mg, 0.0054 mol) were dissolved in ethanol (25 mL). The mixture was heated under reflux for 24 h. The hot mixture was filtered, and the filtered cake was washed with acetone (2 × 80 mL). The solvent was evaporated and the remaining solid was recrystallized from C_2H_5OH:ether (1:10). The compound was obtained as a brown solid. Yield: 25.3% (448 mg), ^{1}H NMR (600 MHz, D_2O, δ): 9.40 (d, 1H), 9.26 (d, 2H), 8.95 (dd, 1H), 8.86 (d, 2H), 8.70 (d, 2H), 8.29 (d, 1H), 8.06 (d, 2H).

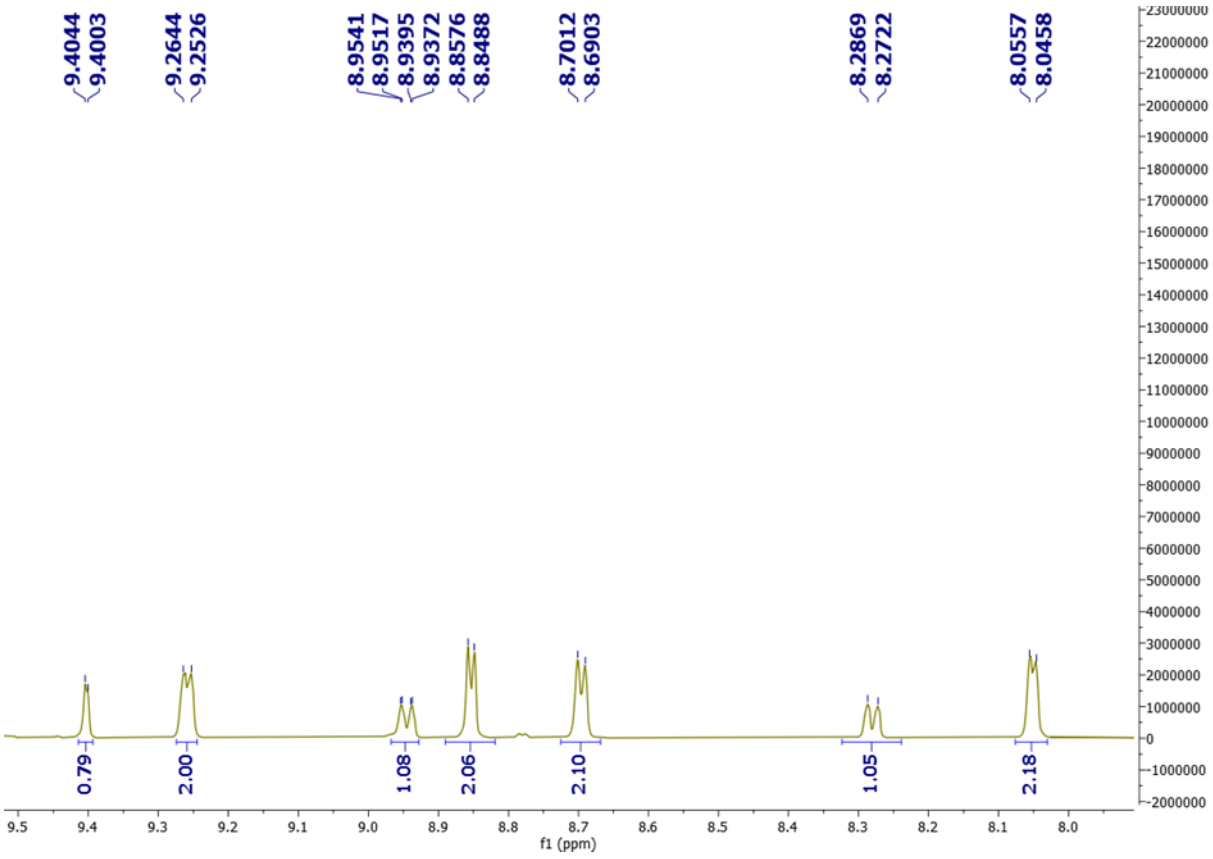

Figure 7.1. *^{1}H NMR spectrum of compound* ***5*** *(D_2O, 600 MHz).*

Synthesis of compound ***8****:* 1-(2,4-dinitrophenyl)-[4,4'-bipyridin]-1-ium chloride (447.6 mg, 1.249 mmol) and *p*-phenylenediamine (64.23 mg, 0.594 mmol) were dissolved in ethanol (15 mL). The mixture was heated under reflux for 72 h. The solvent was evaporated and the remaining solid was washed by acetone (200 mL). The filter cake was collected and dissolved in water and its hexafluorophosphate salt mixture was obtained by ion-exchange with NH_4PF_6 (excess). The pure compound was obtained as brown solid by recrystallization in

MeCN/diethylether (1:3). Yield: 23.6% (91 mg), ^{1}H NMR (600 MHz, CD_3CN, δ): 9.11 (d, 4H), 8.93 (d, 4H), 8.58 (d, 4H), 8.12 (s, 4H), 7.93 (d, 4H).

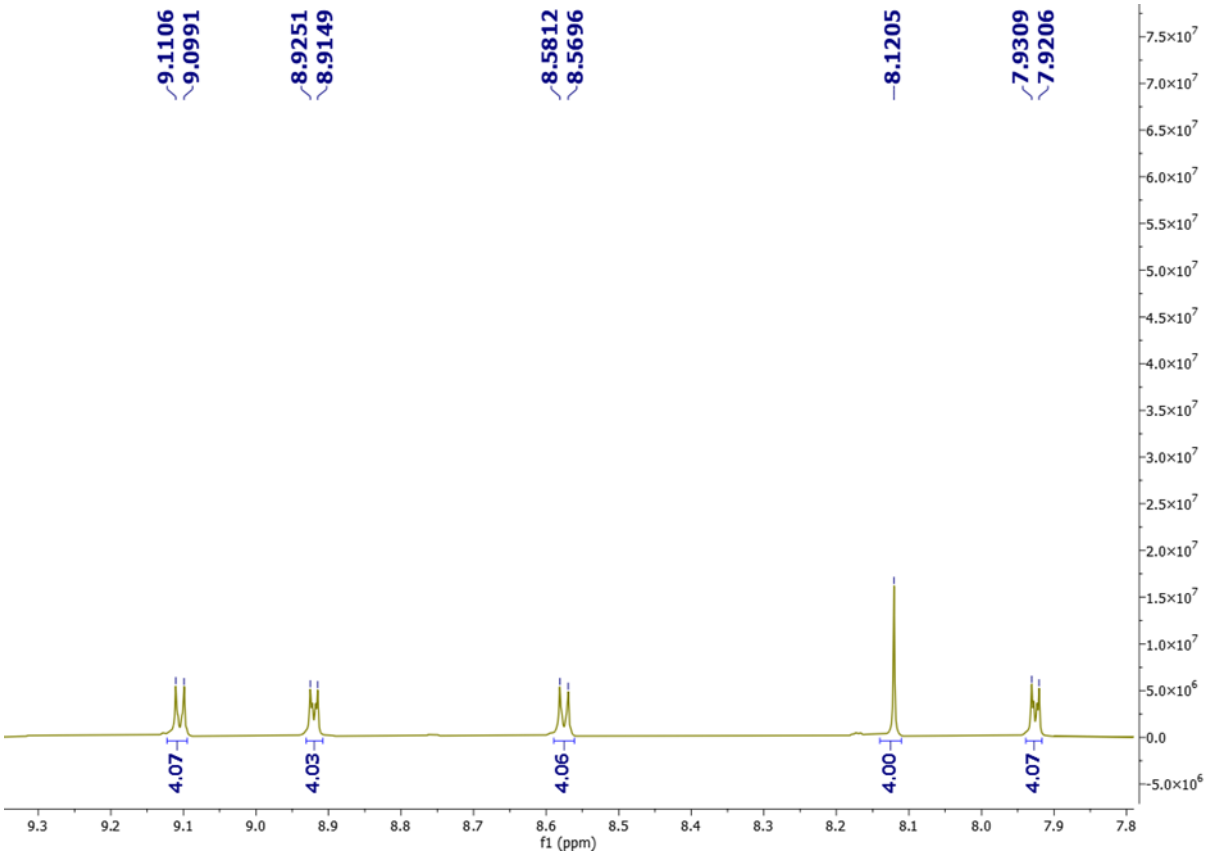

Figure 7.2. *^{1}H NMR spectrum of compound **8** (CD_3CN, 600 MHz).*

*Synthesis of compound **9**:* In a sealed tube, 1,1''-(1,4-phenylene)bis(([4,4'-bipyridin]-1-ium)) hexafluorophosphate (91 mg, 0.14 mmol) was dissolved in acetonitrile (5 ml) and to it methyl iodide (1 ml) was added. The mixture was heated to 80 °C and kept running overnight. The reaction was stopped afterwards, and the solvent evaporated. The solid obtained was dissolved into water and its hexafluorophosphate salt was obtained by ion-exchange with NH_4PF_6 (excess). Yield: 62.2% (87 mg), ^{1}H NMR (600 MHz, CD_3CN, δ): 9.25 (d, 4H), 8.92 (d, 4H), 8.66 (d, 4H), 8.50 (d, 4H), 8.17 (s, 4H), 4.45 (s, 6H).

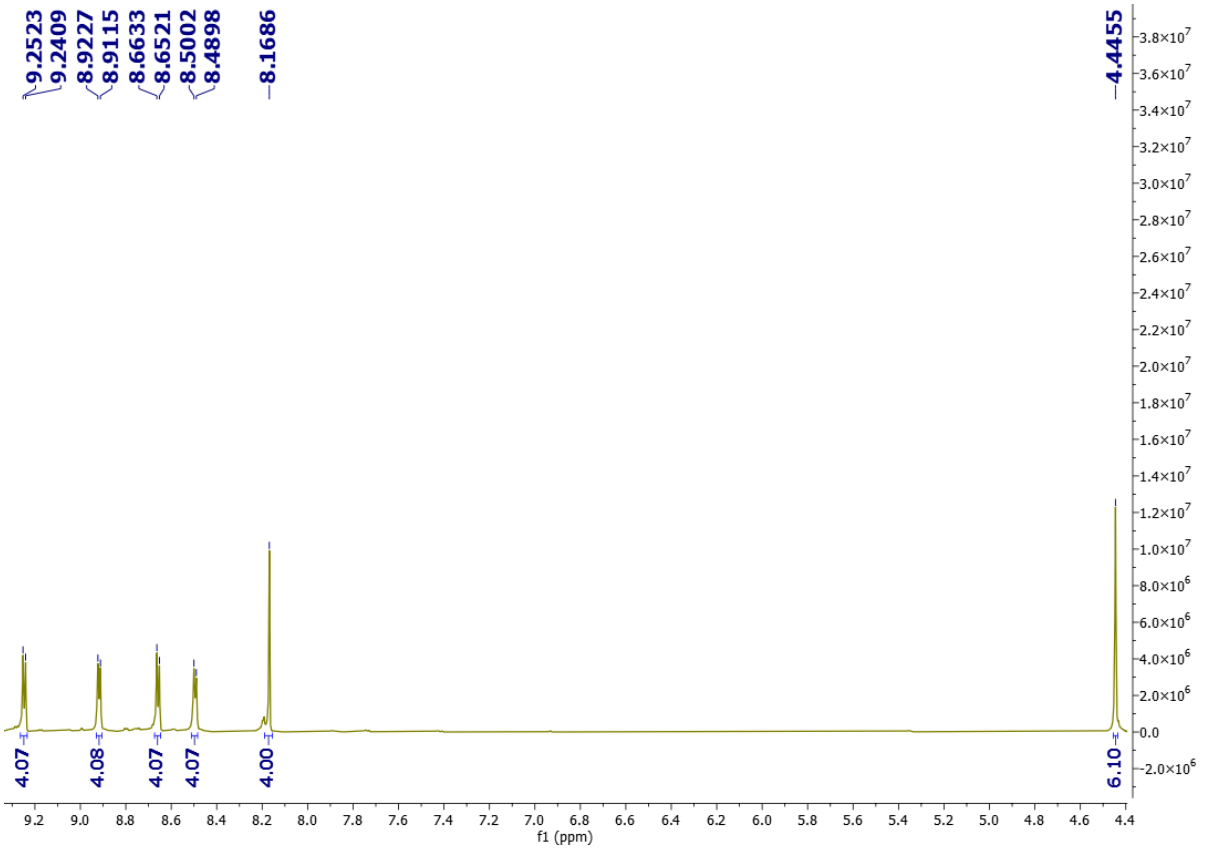

Figure 7.3. *^{1}H NMR spectrum of compound **9** (CD_3CN, 600 MHz).*

*Synthesis of compound **11a** and **11b**:* In a sealed tube, 4,4'-Bipyridine (100 mg) was dissolved in DMSO (4 ml) and to it bromoalkyltrimethylammonium bromide (**10a**: 334.2 mg, 2.4 eqv. or **10b**: 407.19 mg, 2.2 eqv.) was added and the mixture was heated at 80 °C overnight. The reaction was then stopped and to the mixture acetone was added. The precipitates were collected and washed several times with acetone and anion-exchange was performed using NH_4PF_6 (excess). Pure products were isolated as a white powder for **11a** and as red solid for **11b**. ^{1}H NMR of **11a** (600 MHz, CD_3CN, δ): 8.93 (d, 4H), 8.46 (d, 4H), 4.65 (t, 4H), 3,36 (t, 4H), 3.07 (s, 18H), 2.48 (m, 4H). ^{13}C NMR of **11a** (151 MHz, CD_3CN, δ): 151.46, 146.93, 128.51, 63.35, 59.28, 54.25, 25.53. ^{1}H NMR of **11b** (600 MHz, CD_3CN, δ): 8.91 (d, 4H), 8.41 (d, 4H), 4.64 (t, 4H), 3.21 (t, 4H), 3.02 (s, 18H), 2.01 (m, (7-3) H = 4H), 1.79 (m, 4H), 1.42 (m, 4H). ^{13}C NMR of **11b** (151 MHz, CD_3CN, δ): 151.08, 146.59, 128.28, 67.01, 62.59, 53.94, 53.89, 31.19, 23.14, 22.91.

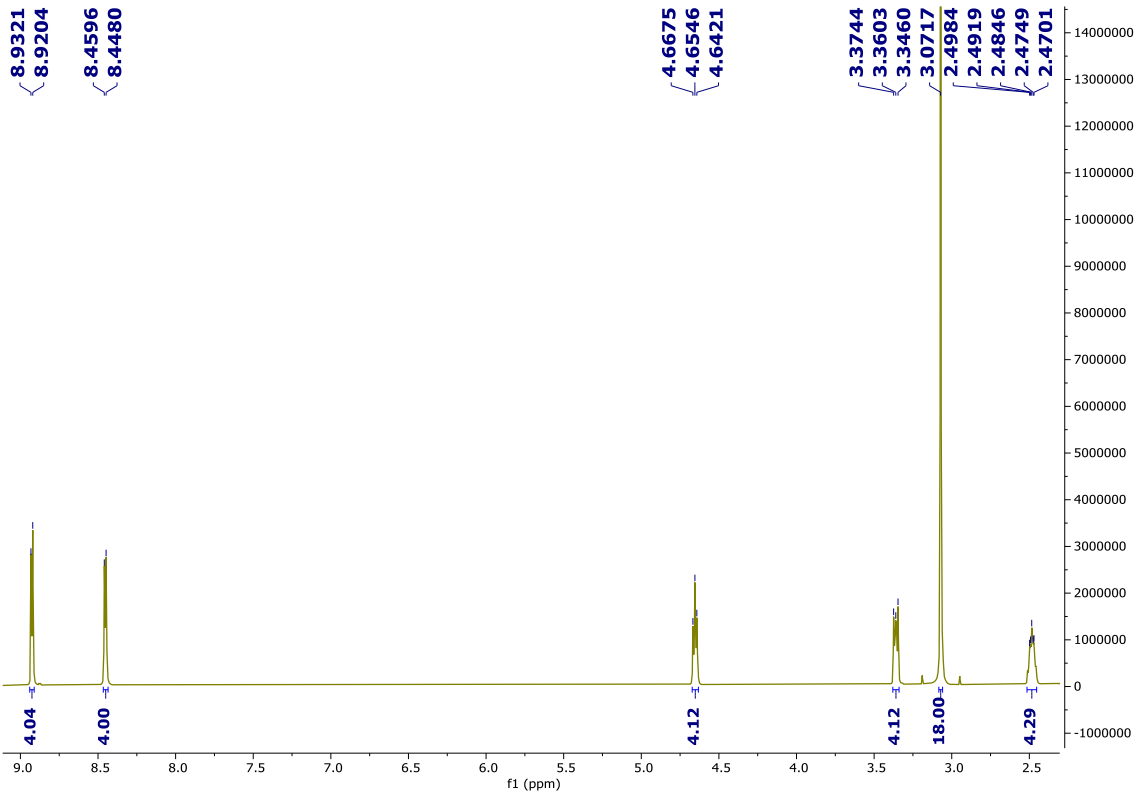

Figure 7.4. *^{1}H NMR spectrum of compound **11a** (CD_3CN, 600 MHz).*

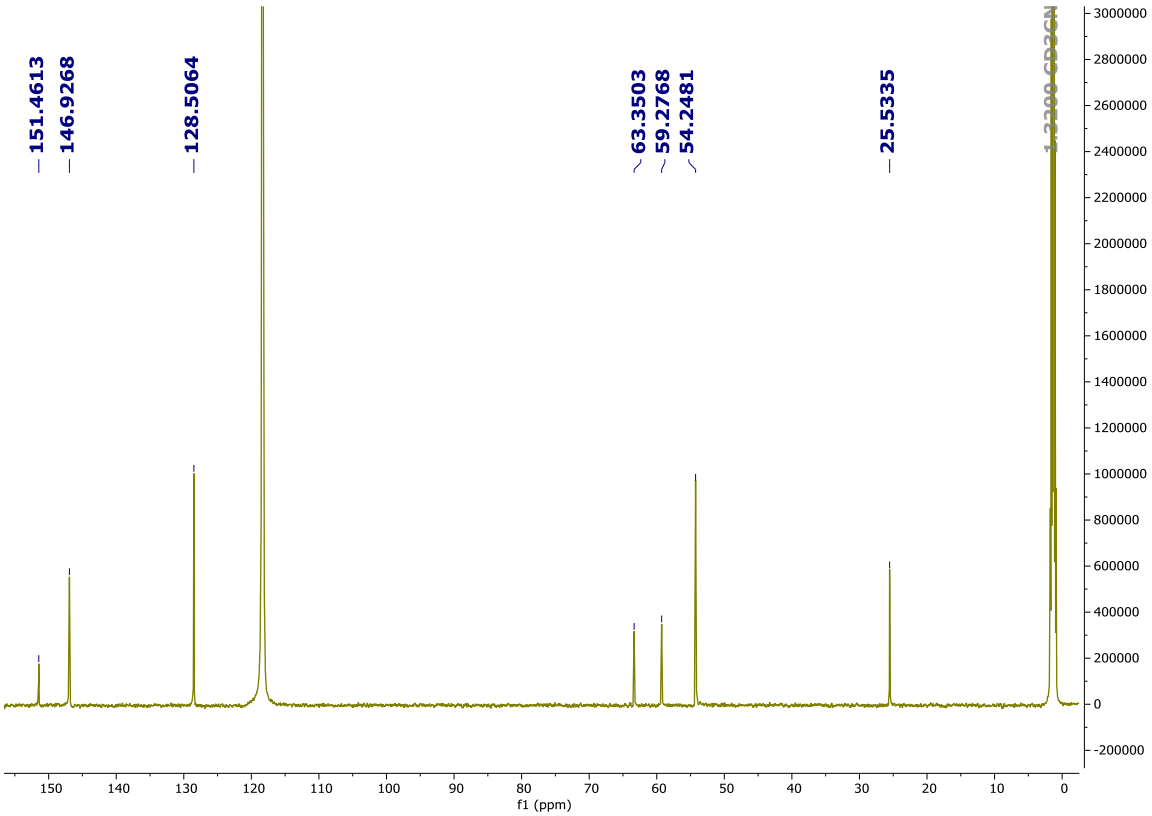

Figure 7.5. *^{13}C NMR spectrum of compound **11a** (CD_3CN, 151 MHz).*

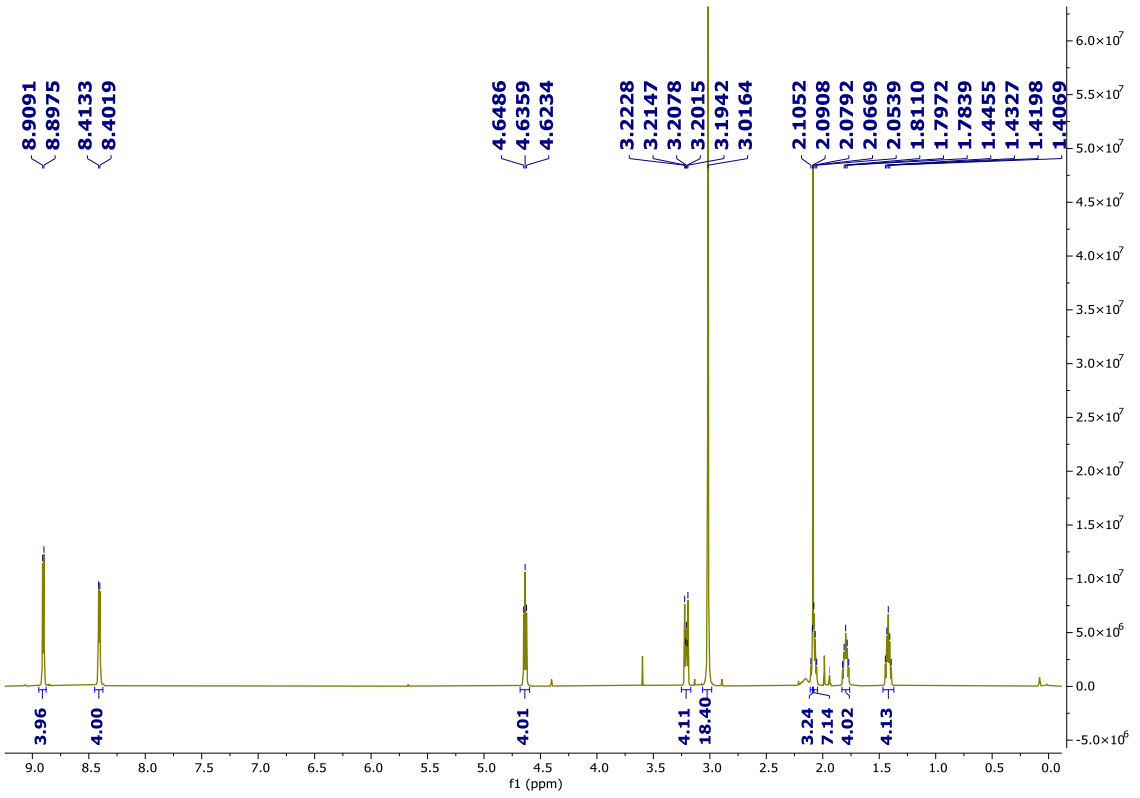

Figure 7.6. *^{1}H NMR spectrum of compound **11b** (CD_3CN, 600 MHz).*

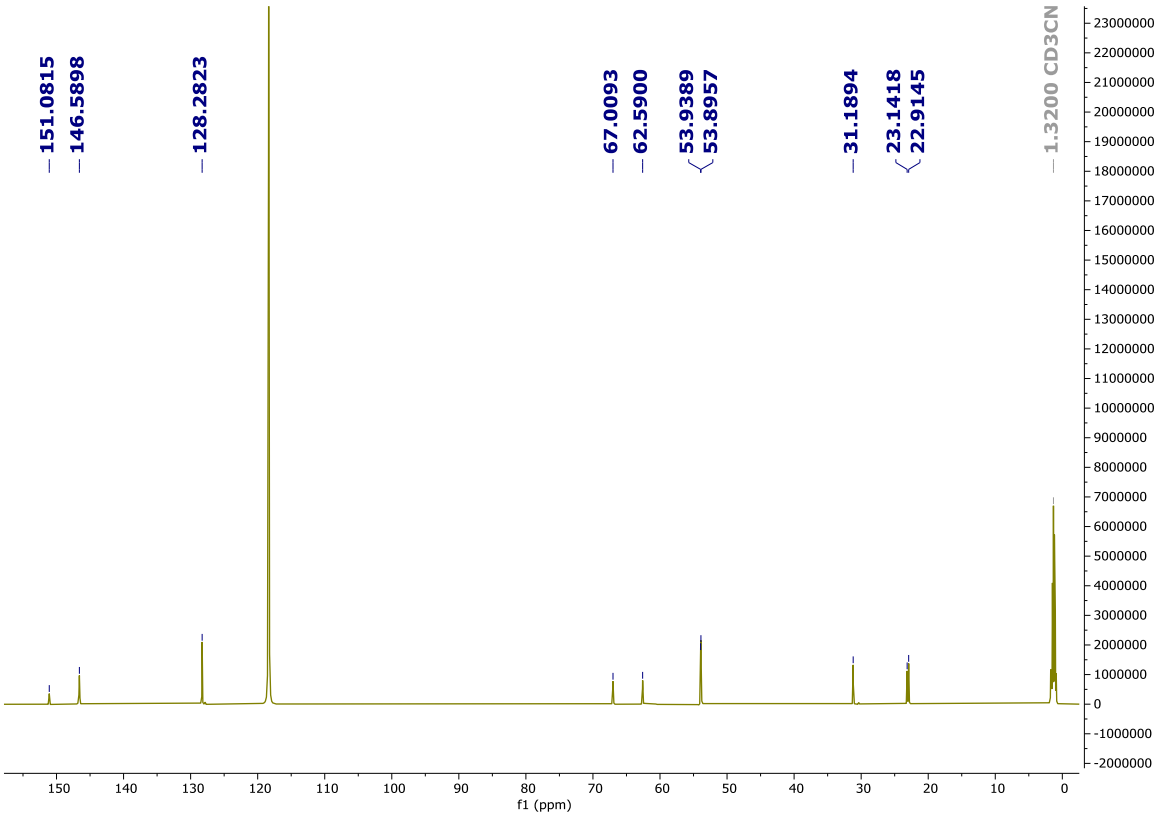

Figure 7.7. *^{13}C NMR spectrum of compound **11b** (CD_3CN, 151 MHz).*

Synthesis of compound ***12****:* In a sealed tube, 4,4'-bipyridine (500 mg, 3.2 mmol, 1 eqv.) was dissolved in acetone (15 ml). To it, methyl iodide (0.4 ml, 6.43 mmol, 2 eqv.) was added. The mixture was stirred at room temperature for 24 hours. The precipitate was filtered, washed with acetone, and the filter cake was collected by redissolving it in methanol. Yield: 89.4% (853.11 mg), ^{1}H NMR (600 MHz, CD_3OD, δ): 9.04 (d, 2H), 8.84 (d, 2H), 8.51 (d, 2H), 7.99 (d, 2H), 4.47 (s, 3H).

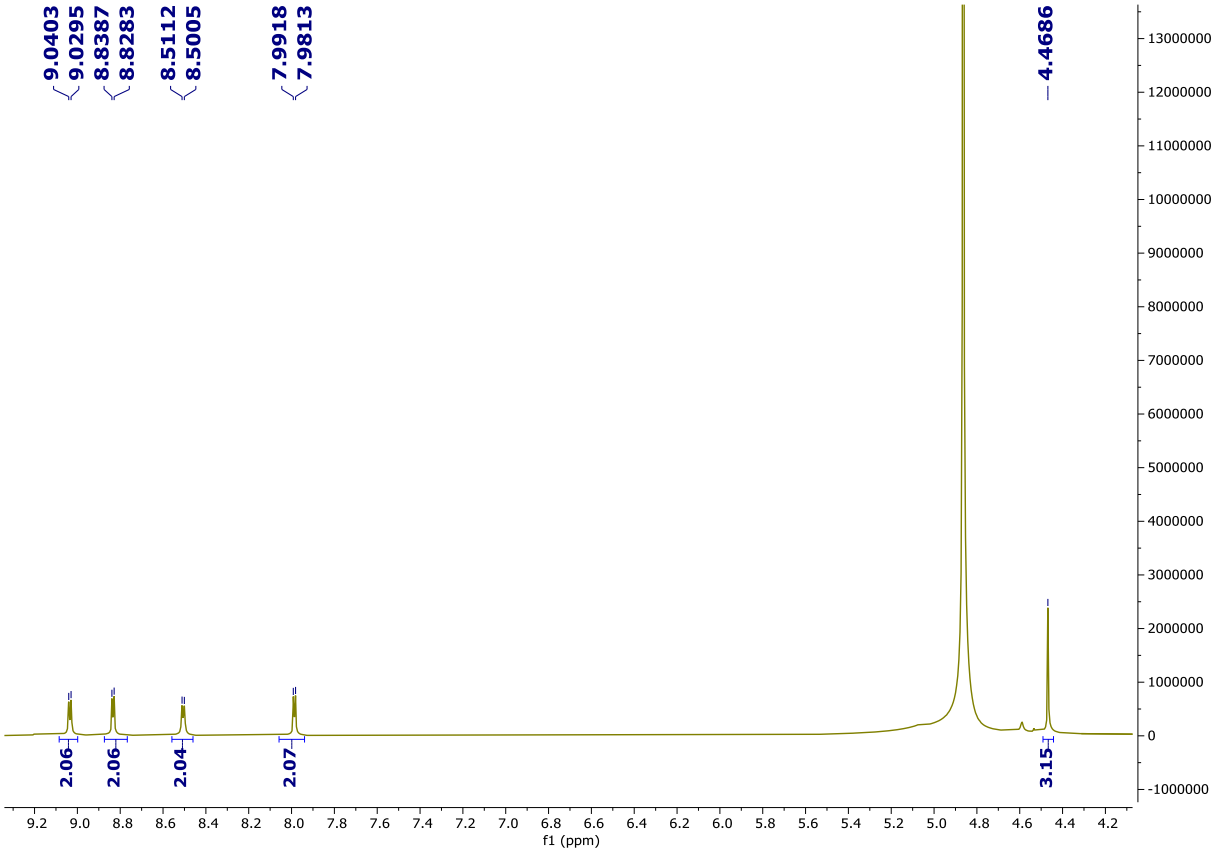

Figure 7.8. *^{1}H NMR spectrum of compound* ***12*** *(CD_3OD, 600 MHz).*

Synthesis of compound ***14****:* In a capped vial, *N*-methyl-4,4'-bipyridinium iodide (500 mg, 1.68 mmol) was dissolved in DMSO (3 ml). To it, 4-vinylbenzylchloride (0.29 ml, apprx. 308 mg, 1.2 eqv) was added. The mixture was stirred at room temperature for 24 hours. To the mixture, acetonitrile (20 ml) was added. The orange solid was precipitated and collected by filtration. The filter cake was washed with acetonitrile and recollected using methanol. Yield: 50.9% (386.46 mg). The hexafluorophosphate salt derivative was obtained by ion-exchange with NH_4PF_6 (excess). The pure compound was obtained as white solid, ^{1}H NMR (600 MHz, CD_3OD, δ): 9.34 (d, 2H), 9.19 (d, 2H), 8.68 (d, 2H), 8.65 (d, 2H), 7.58

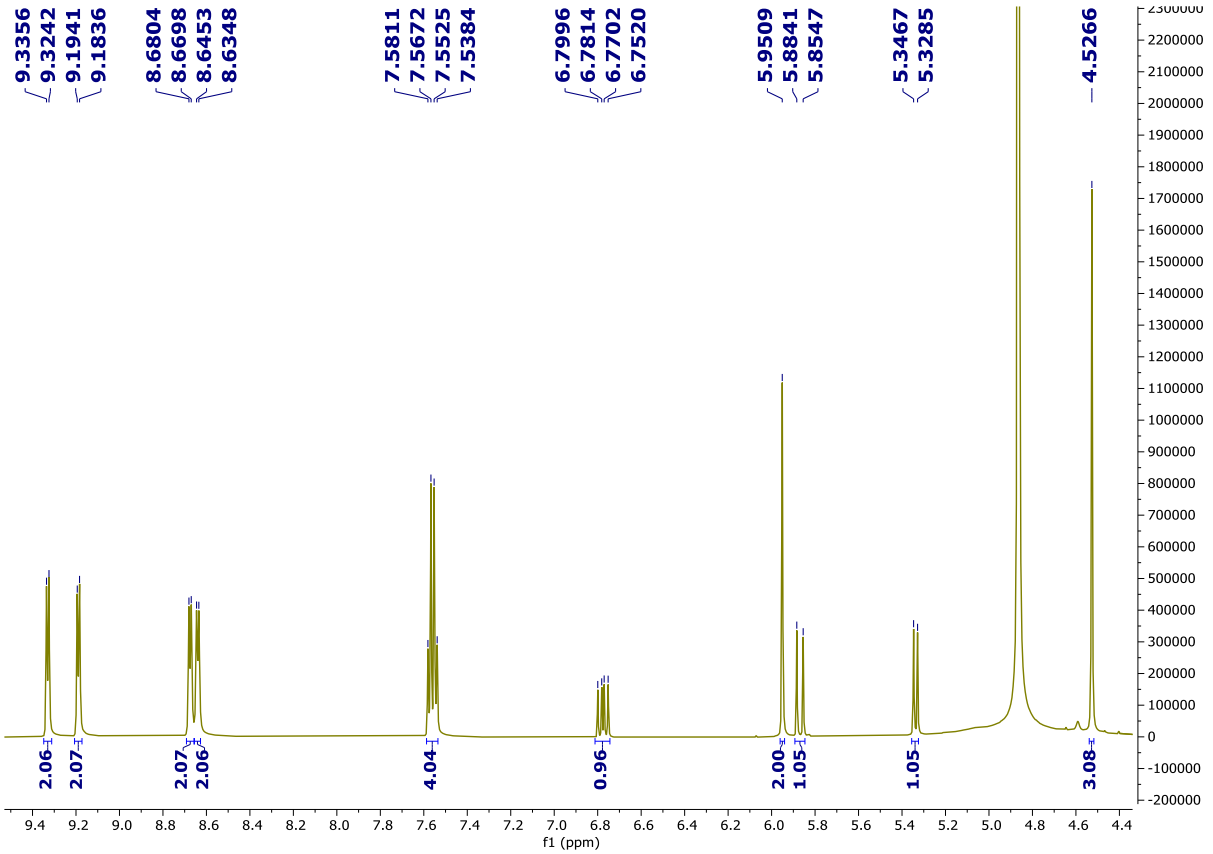

Figure 7.9. *^{1}H NMR spectrum of compound **14** (CD_3OD, 600 MHz).*

*Synthesis of compound **15**:* In a nitrogen-filled sealed tube, compound **14** (82.34 mg) was dissolved in DMSO (4 ml) and to it $K_2S_2O_8$ (15 mg) was added, and the mixture was heated to 80 °C overnight. The reaction was then stopped and to the mixture acetone was added. The precipitates were collected, redispersed in acetone by sonication and the solvent was removed by centrifugation. The washing step was repeated several times and the solid was collected separately.

*Synthesis of compound **17**:* 2.2g (1.0 eq., 10 mmol) pyrene was dissolved in a mixture of 40 mL DCM and 40 mL acetonitrile in a 250 mL round bottom flask. Then 50 mL distilled water, 18.9 g (8.2 eq., 82 mmol) KIO_4, and 0.025g (1.2%, 0.12 mmol) $RuCl_3 \cdot xH_2O$ were added at 0 °C. The round bottom flask was kept at 50 °C after 3 mins stirring in an ice bath. The reaction was monitored by TLC every hour. Then 0.025 g $RuCl_3 \cdot xH_2O$ was added after 4 h. After 8 hours, 4.3 g $NaIO_4$ was added and stirred for 3.5 hours. The reaction mixture was poured into 200 mL of H_2O, and the solid filter-cake was removed by filtration. After the filter-cake was washed with excess of H_2O, the solid thus obtained was separated. The aqueous phase was extracted with DCM (3 × 50 mL) and the solvent was evaporated. The solid, thus obtained, was combined with the filter cake and column chromatography (DCM:Ethyl Acetate = 96:4) was performed to give pure product as bright orange crystals (Yield: 29%). ^{1}H NMR (600 MHz, $CDCl_3$, δ): 8.53 (d, 4H), 7.75 (t, 2H).

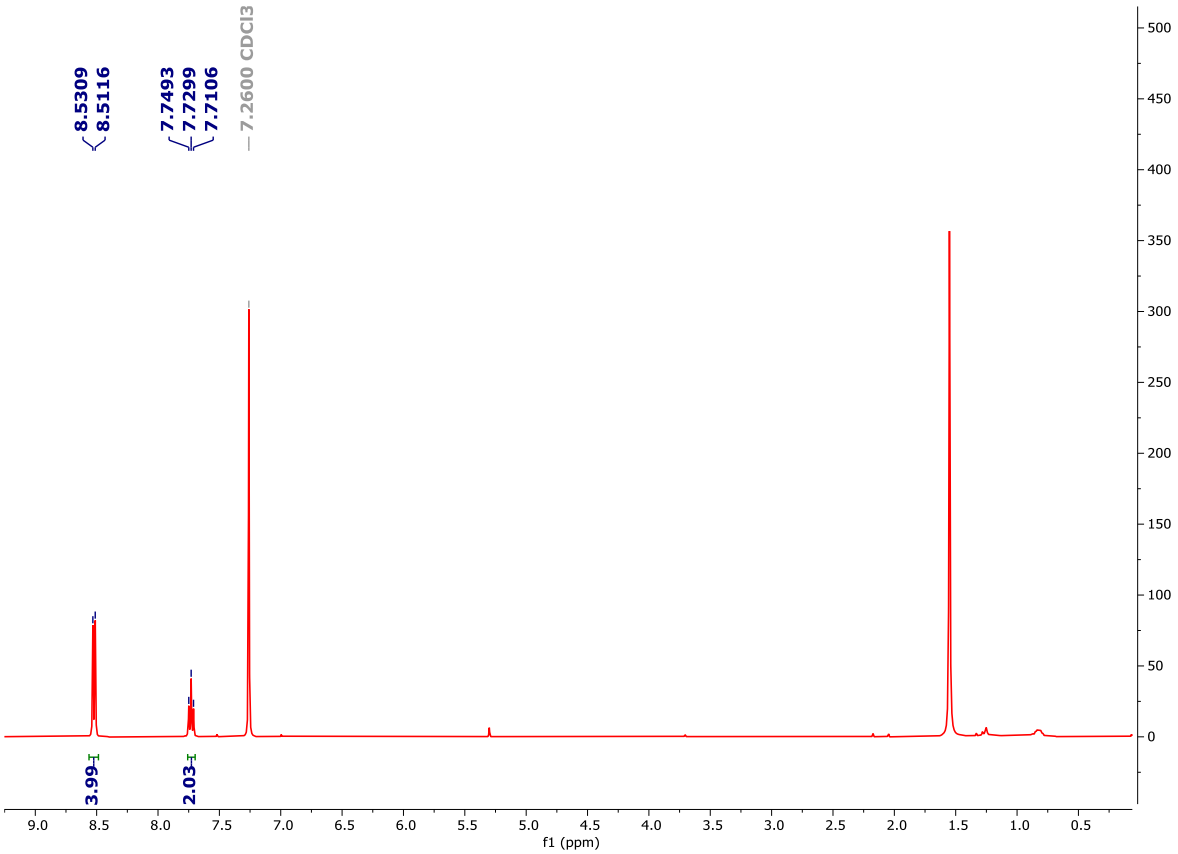

Figure 7.10. *^{1}H NMR spectrum of compound **17** ($CDCl_3$, 600 MHz).*

*Synthesis of compound **18**:* In an RB flask, compound **17** (101.79 mg, 0.572 mmol) and concentrated sulphuric acid (3 ml) was stirred for 5 minutes in an ice bath. To the mixture, NBS (145.1 mg, 1.2 mmol) was added and was stirred again for 5 minutes. The mixture was then heated to 50 ℃ for 2 hours. Upon completion the mixture was dumped into ice cold water, and the resultant precipitate was then collected by filtration, and the filter cake was washed several times with DI water. The filter cake was then collected by dispersing in methanol and the solvent was then evaporated using rotary evaporator. The di-bromo derivative was isolated using column chromatography (DCM:ethyl acetate = 99:1) as a pale-yellow solid (yield: 42%). ^{1}H NMR (600 MHz, $CDCl_3$, δ): 8.6 (s, 4H).

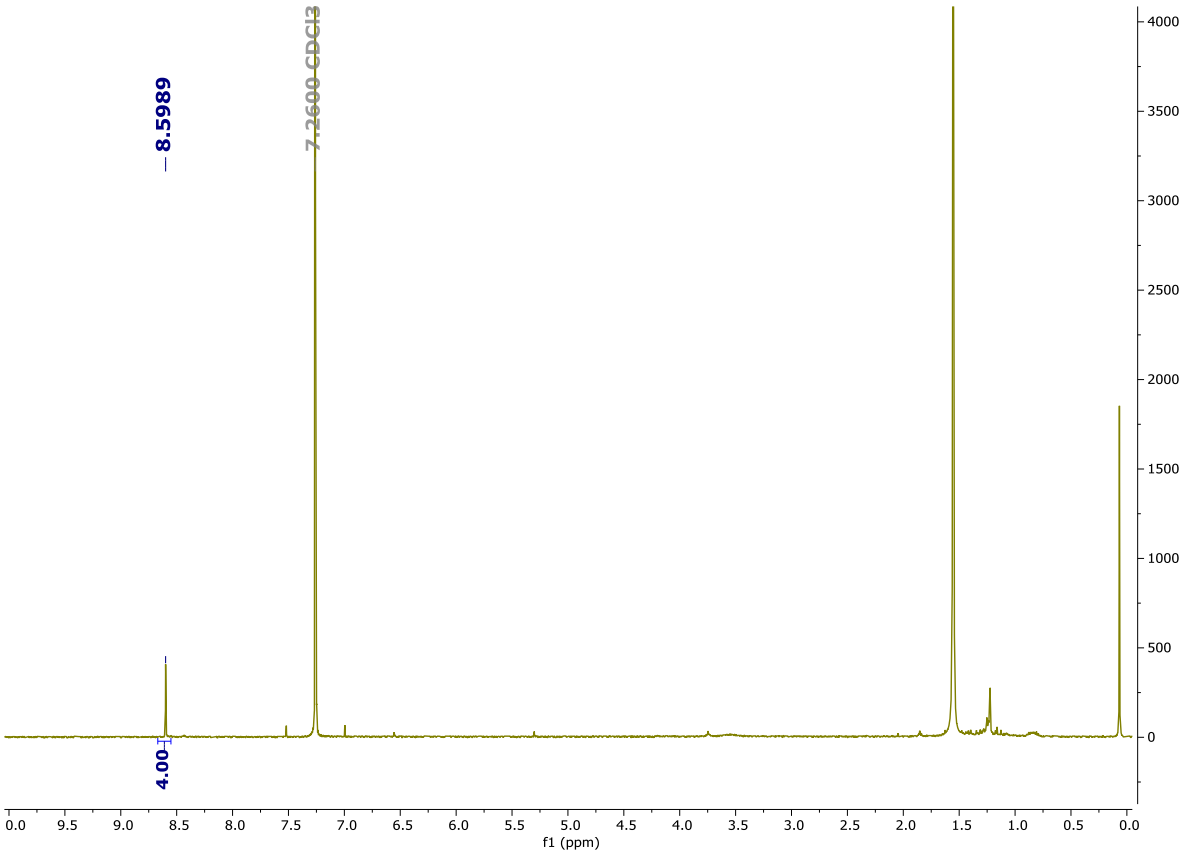

Figure 7.11. *^{1}H NMR spectrum of compound* ***18*** *($CDCl_3$, 600 MHz).*

Synthesis of compound ***19****:* Compound **18** (63 mg, 0.15 mmol) and $TsOH.H_2O$ (57 mg, 0.3 mmol) were added into a flask with a mixed solution of ethylene glycol (3 mL) and toluene (10 ml). The resulting mixture was refluxed at 110 °C under argon protection for 18 hrs. After the solution cooled down to room temperature, the solvent evaporated, and excess water was added to the mixture. The solid, thus formed, was washed with excess of H_2O and with MeOH afterwards, dried to obtain off-white solid (56 mg, 63%).^{1}H NMR (600 MHz, $CDCl_3$, δ): 8.6 (s, 4H), 4.21 (br, 8H), 3.67 (br, 8H).

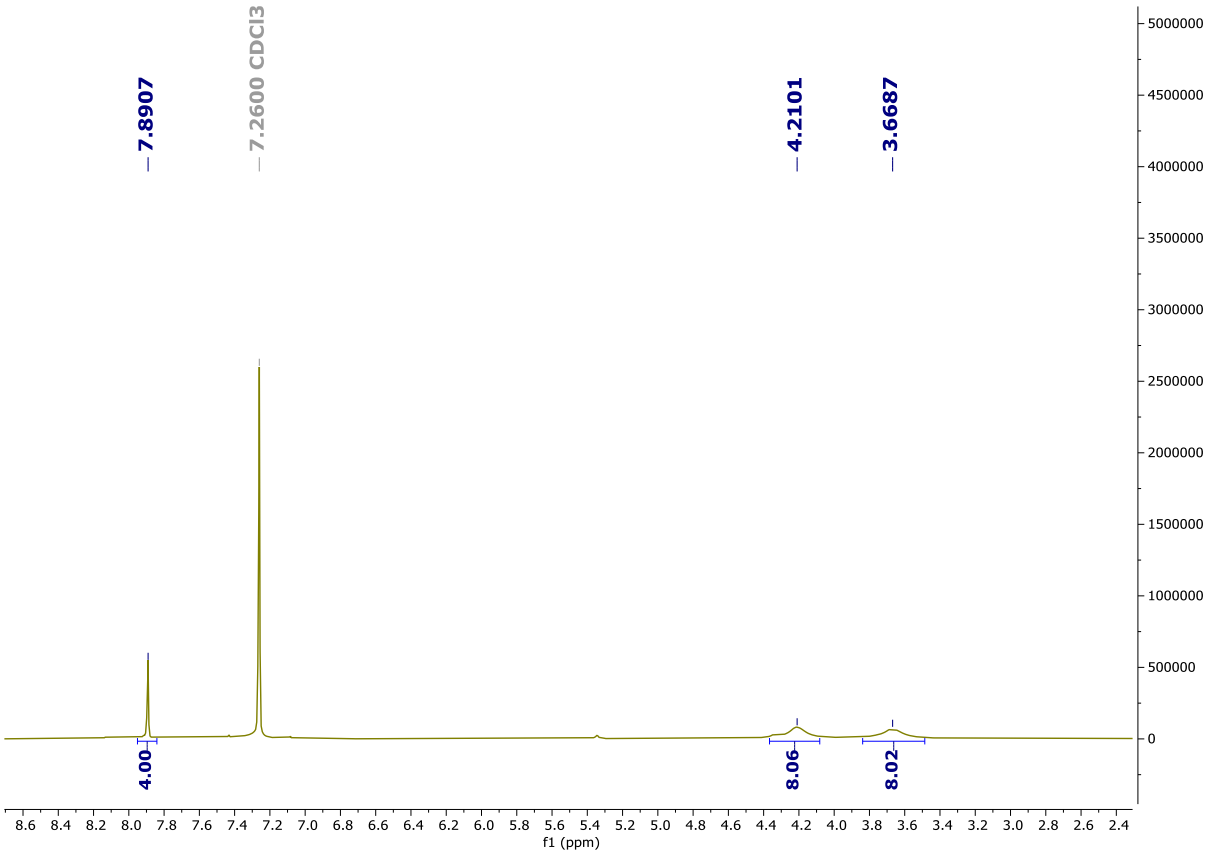

Figure 7.12. *^{1}H NMR spectrum of compound **19** ($CDCl_3$, 600 MHz).*

*Synthesis of compound **21**:* A sealed tube was charged with compound **19** (82 mg, 120 µmol) pyridinyl-4-boronic acid (76 mg, 350 µmol) was added as a solution in THF (2 mL), followed by aqueous 1M Cs_2CO_3 solution (2 mL) under N_2 atmosphere. While stirring Xphos-Pd-G2 (3 mg, 3.6 µmol) was added. The mixture was stirred vigorously at 85 °C for 17 h. The reaction mixture was cooled down to room temperature and was extracted with ethyl acetate (4×5 mL). The combined organic phases were dried over Na_2SO_4, and the solvents were removed under reduced pressure. The crude product was purified by preparative TLC (PE:DCM:MeOH = 10:9:1) to obtain the product as a white solid. ^{1}H NMR of **21** (600 MHz, CD_3CN, δ): 8.72 (d, 4H), 8.1 (s, 4H), 7.64 (d, 4H), 4.27 (br, 8H), 3.72 (br, 8H). ^{13}C NMR of **21** (151 MHz, CD_3CN, δ): 150.6, 147.3, 139.7, 134.4, 129.5, 125.8, 121.7, 92.6.

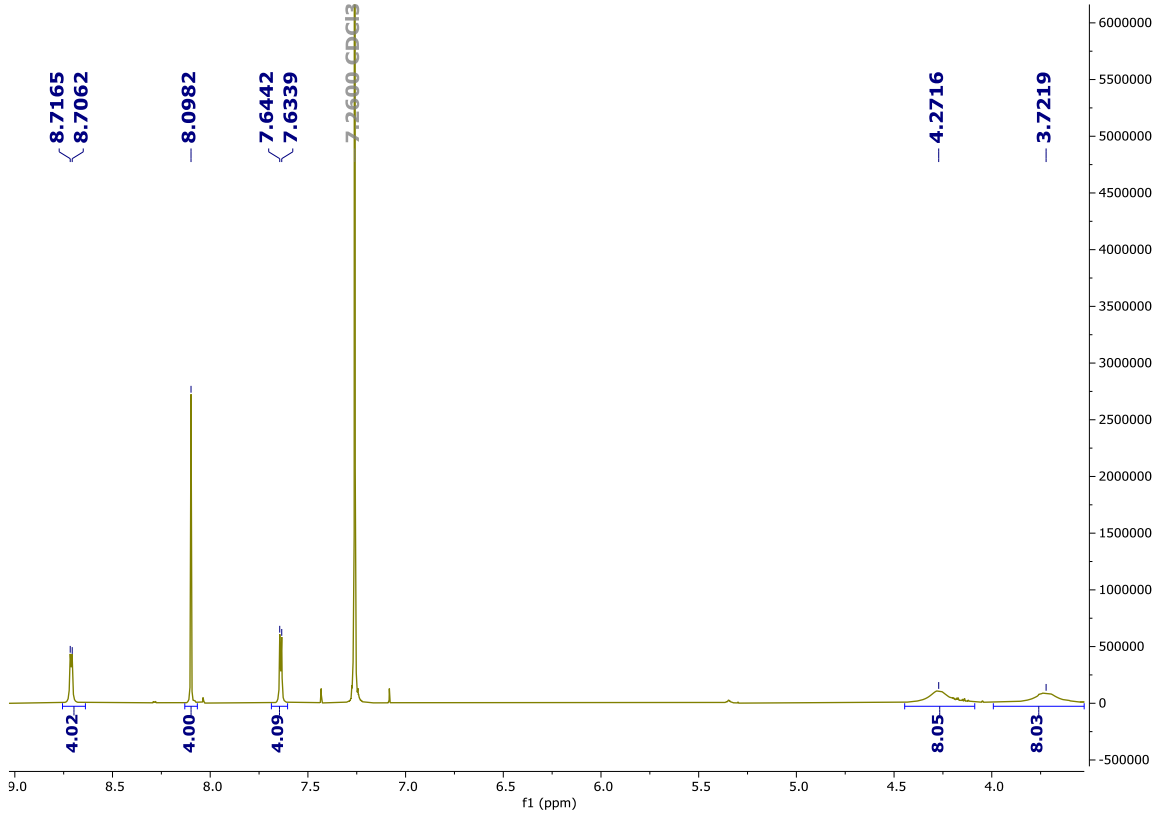

Figure 7.13. *^{1}H NMR spectrum of compound **21** ($CDCl_3$, 600 MHz).*

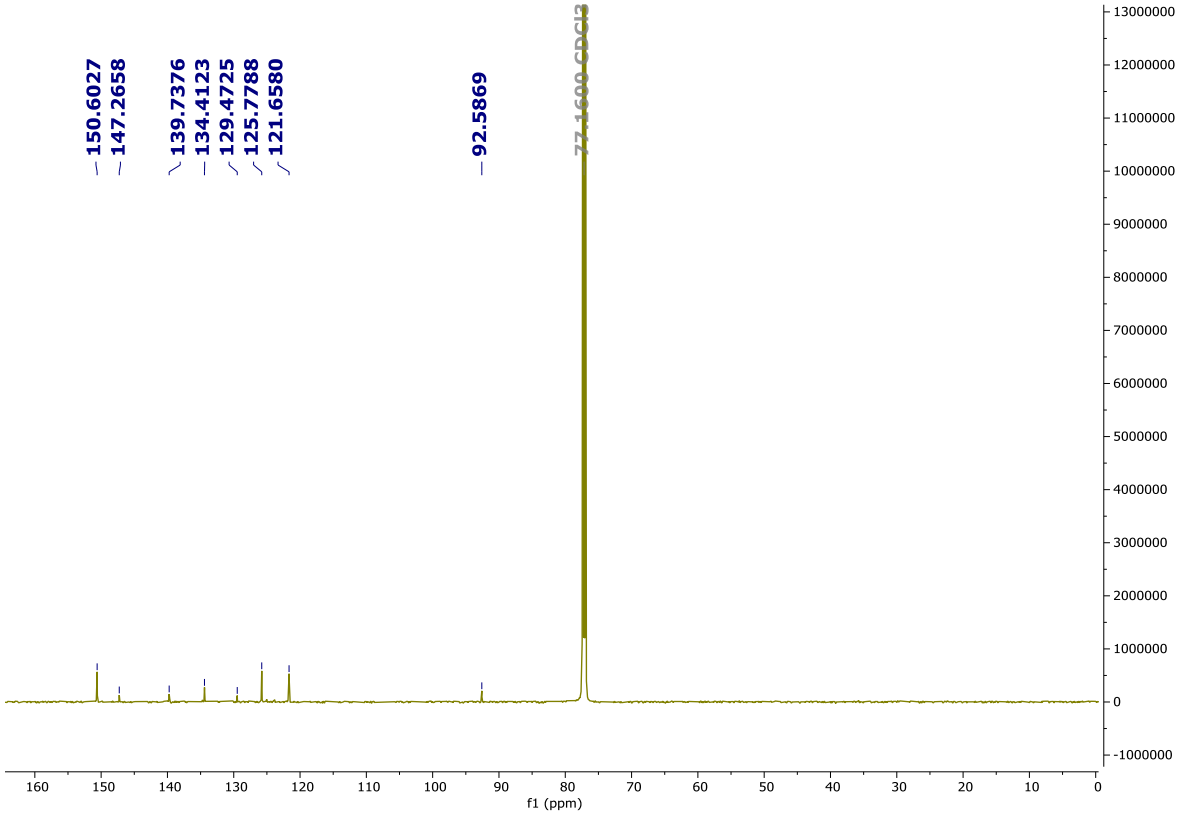

Figure 7.14. *^{13}C NMR spectrum of compound **21** ($CDCl_3$, 151 MHz).*

*Synthesis of compound **23**:* A sealed tube was charged with compound **23** (19 mg, 32 µmol) methyl iodide (0.3 ml) was added in 4 ml of dioxane. The mixture was stirred vigorously at 80 °C overnight. The reaction mixture was cooled down to room temperature and the solvent was evaporated under rota-vap. The solid thus obtained was dispersed in 0.2 ml water and to it 1.8 ml of TFA was added (TFA:water = 9:1). The mixture was then sealed and stirred at 72 °C. The mixture was dumped into ice-water to obtain the product as an orange solid. ^{1}H NMR of **23–TFA$_2$** (400 MHz, CD_3OD, δ): 9.00 (d, 4H), 8.87 (s, 4H), 8.69 (d, 4H), 4.75 (s, 6H). ^{19}F NMR of **23-TFA$_2$** (376 MHz, CD_3OD, δ): –77.3.

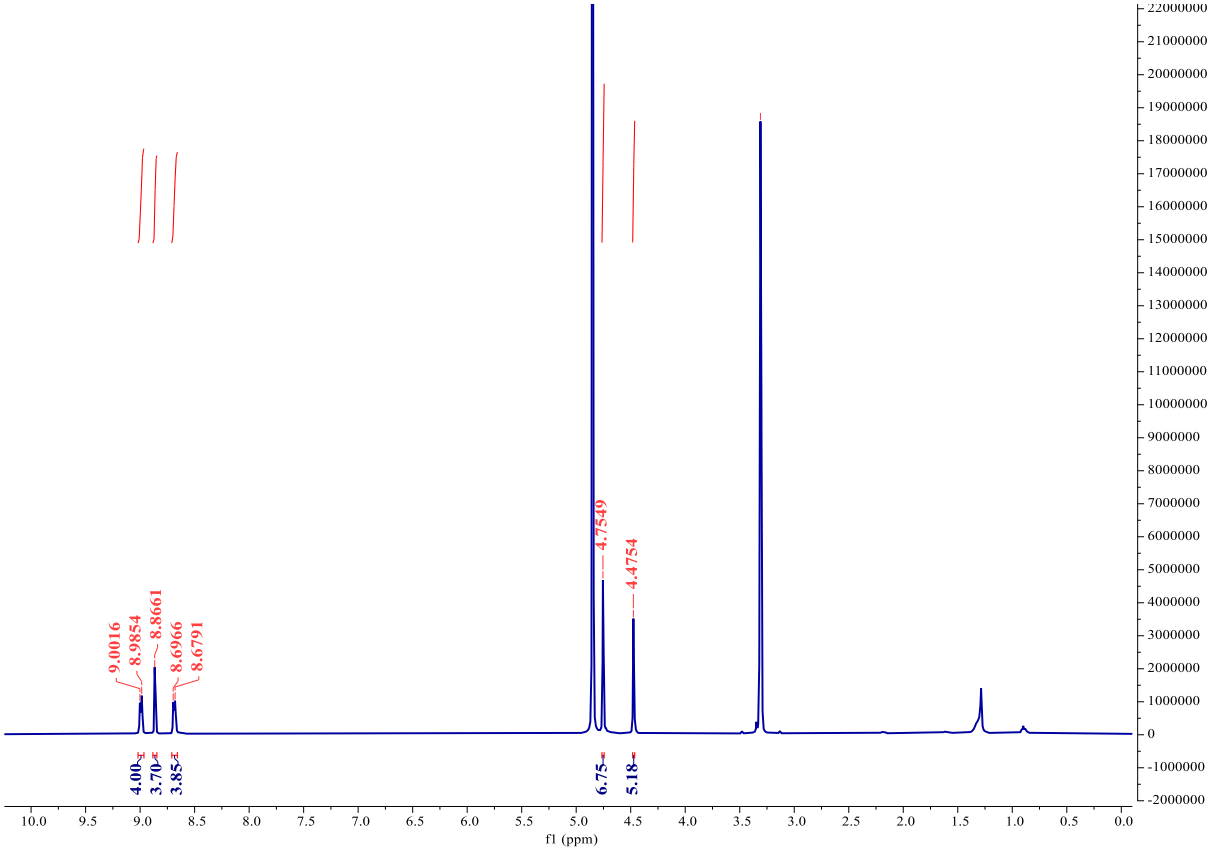

Figure 7.15. *^{1}H NMR spectrum of compound **23** (CD_3OD, 400 MHz).*

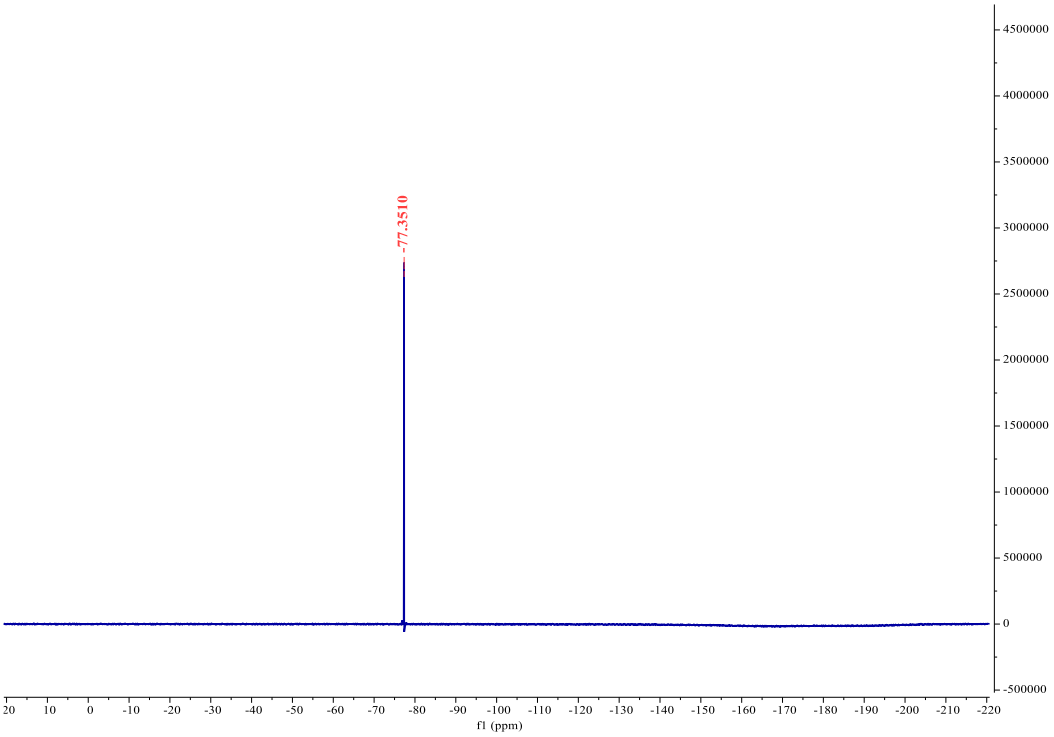

Figure 7.16. *^{19}F NMR spectrum of compound* ***23*** *(CD_3OD, 376 MHz).*

Chapter 8

Bibliography

1. Buzea, C.; Pacheco, II; Robbie, K., *Biointerphases* **2007,** *2* (4), MR17.
2. *Nat. Phys.* **2024,** *20* (1), 1.
3. Novoselov, K. S.; Geim, A. K.; Morozov, S. V.; Jiang, D.; Zhang, Y.; Dubonos, S. V.; Grigorieva, I. V.; Firsov, A. A., *Science* **2004,** *306* (5696), 666.
4. Geim, A. K.; Novoselov, K. S., *Nat. Mater.* **2007,** *6* (3), 183.
5. Du, X.; Skachko, I.; Barker, A.; Andrei, E. Y., *Nat. Nanotechnol.* **2008,** *3* (8), 491.
6. Bolotin, K. I.; Sikes, K. J.; Jiang, Z.; Klima, M.; Fudenberg, G.; Hone, J.; Kim, P.; Stormer, H. L., *Solid State Commun.* **2008,** *146* (9), 351.
7. Balandin, A. A.; Ghosh, S.; Bao, W.; Calizo, I.; Teweldebrhan, D.; Miao, F.; Lau, C. N., *Nano Lett.* **2008,** *8* (3), 902.
8. Pasadas, F.; Medina-Rull, A.; Ruiz, F. G.; Ramos-Silva, J. N.; Pacheco-Sanchez, A.; Pardo, M. C.; Toral-Lopez, A.; Godoy, A.; Ramírez-García, E.; Jiménez, D.; Marin, E. G., *Small* **2023,** *19* (49), 2303595.
9. Du, X.; Skachko, I.; Duerr, F.; Luican, A.; Andrei, E. Y., *Nature* **2009,** *462* (7270), 192.
10. Hu, S.; Lozada-Hidalgo, M.; Wang, F. C.; Mishchenko, A.; Schedin, F.; Nair, R. R.; Hill, E. W.; Boukhvalov, D. W.; Katsnelson, M. I.; Dryfe, R. A. W.; Grigorieva, I. V.; Wu, H. A.; Geim, A. K., *Nature* **2014,** *516* (7530), 227.
11. Li, X.; Cai, W.; An, J.; Kim, S.; Nah, J.; Yang, D.; Piner, R.; Velamakanni, A.; Jung, I.; Tutuc, E.; Banerjee, S. K.; Colombo, L.; Ruoff, R. S., *Science* **2009,** *324* (5932), 1312.
12. Lee, C.; Wei, X.; Kysar, J. W.; Hone, J., *Science* **2008,** *321* (5887), 385.
13. Lin, L.; Peng, H.; Liu, Z., *Nat. Mater.* **2019,** *18* (6), 520.
14. Amontree, J.; Yan, X.; DiMarco, C. S.; Levesque, P. L.; Adel, T.; Pack, J.; Holbrook, M.; Cupo, C.; Wang, Z.; Sun, D.; Biacchi, A. J.; Wilson-Stokes, C. E.; Watanabe, K.; Taniguchi, T.; Dean, C. R.; Hight Walker, A. R.; Barmak, K.; Martel, R.; Hone, J., *Nature* **2024,** *630* (8017), 636.
15. Bridgman, P. W., *J. Am. Chem. Soc.* **1914,** *36* (7), 1344.
16. Ling, X.; Wang, H.; Huang, S.; Xia, F.; Dresselhaus, M. S., *Proc. Natl. Acad. Sci.* **2015,** *112* (15), 4523.
17. Tran, V.; Soklaski, R.; Liang, Y.; Yang, L., *Phys. Rev. B* **2014,** *89* (23), 235319.
18. Liu, Y.; Xu, F.; Zhang, Z.; Penev, E. S.; Yakobson, B. I., *Nano Lett.* **2014,** *14* (12), 6782.
19. Yu, X.-f.; Ushiyama, H.; Yamashita, K., *Chem. Lett.* **2014,** *43* (12), 1940.
20. Castellanos-Gomez, A.; Vicarelli, L.; Prada, E.; Island, J. O.; Narasimha-Acharya, K. L.; Blanter, S. I.; Groenendijk, D. J.; Buscema, M.; Steele, G. A.; Alvarez, J. V.; Zandbergen, H. W.; Palacios, J. J.; van der Zant, H. S. J., *2d Mater.* **2014,** *1* (2), 025001.
21. Zhang, S.; Yang, J.; Xu, R.; Wang, F.; Li, W.; Ghufran, M.; Zhang, Y.-W.; Yu, Z.; Zhang, G.; Qin, Q.; Lu, Y., *ACS nano* **2014,** *8* (9), 9590.
22. Dai, J.; Zeng, X. C., *RSC Adv.* **2014,** *4* (89), 48017.
23. Wood, J. D.; Wells, S. A.; Jariwala, D.; Chen, K.-S.; Cho, E.; Sangwan, V. K.; Liu, X.; Lauhon, L. J.; Marks, T. J.; Hersam, M. C., *Nano Lett.* **2014,** *14* (12), 6964.
24. Jiang, J.-W.; Park, H. S., *Nat. Commun.* **2014,** *5* (1), 4727.
25. Jiang, J.-W.; Park, H. S., *J. Phys. D Appl. Phys.* **2014,** *47* (38), 385304.

26. Wang, H.; Wang, X.; Xia, F.; Wang, L.; Jiang, H.; Xia, Q.; Chin, M. L.; Dubey, M.; Han, S.-j., *Nano Lett.* **2014,** *14* (11), 6424.
27. Du, Y.; Liu, H.; Deng, Y.; Ye, P. D., *ACS nano* **2014,** *8* (10), 10035.
28. Das, S.; Zhang, W.; Demarteau, M.; Hoffmann, A.; Dubey, M.; Roelofs, A., *Nano Lett.* **2014,** *14* (10), 5733.
29. Buscema, M.; Groenendijk, D. J.; Blanter, S. I.; Steele, G. A.; van der Zant, H. S. J.; Castellanos-Gomez, A., *Nano Lett.* **2014,** *14* (6), 3347.
30. Buscema, M.; Groenendijk, D. J.; Steele, G. A.; van der Zant, H. S. J.; Castellanos-Gomez, A., *Nat. Commun.* **2014,** *5* (1), 4651.
31. Hong, T.; Chamlagain, B.; Lin, W.; Chuang, H.-J.; Pan, M.; Zhou, Z.; Xu, Y.-Q., *Nanoscale* **2014,** *6* (15), 8978.
32. Kou, L.; Frauenheim, T.; Chen, C., *J. Phys. Chem. Lett.* **2014,** *5* (15), 2675.
33. Chekmazov, S. V.; Zagitova, A. A.; Ionov, A. M.; Protasova, S. G.; Zverev, V. N.; Mazilkin, A. A.; Kulakov, V. I.; Bozhko, S. I., *J. Surf. Investig.* **2023,** *17* (3), 620.
34. Morita, A., *Appl. Phys. A* **1986,** *39* (4), 227.
35. Asahina, H.; Shindo, K.; Morita, A., *J. Phys. Soc. Jpn.* **1982,** *51* (4), 1193.
36. Xia, F.; Wang, H.; Jia, Y., *Nat. Commun.* **2014,** *5* (1), 4458.
37. Liang, L.; Wang, J.; Lin, W.; Sumpter, B. G.; Meunier, V.; Pan, M., *Nano Lett.* **2014,** *14* (11), 6400.
38. Novoselov, K. S.; Geim, A. K.; Morozov, S. V.; Jiang, D.; Katsnelson, M. I.; Grigorieva, I. V.; Dubonos, S. V.; Firsov, A. A., *Nature* **2005,** *438* (7065), 197.
39. Mak, K. F.; Lee, C.; Hone, J.; Shan, J.; Heinz, T. F., *Phys. Rev. Lett.* **2010,** *105* (13), 136805.
40. Britnell, L.; Ribeiro, R. M.; Eckmann, A.; Jalil, R.; Belle, B. D.; Mishchenko, A.; Kim, Y.-J.; Gorbachev, R. V.; Georgiou, T.; Morozov, S. V.; Grigorenko, A. N.; Geim, A. K.; Casiraghi, C.; Neto, A. H. C.; Novoselov, K. S., *Science* **2013,** *340* (6138), 1311.
41. Zhou, Q.; Chen, Q.; Tong, Y.; Wang, J., *Angew. Chem. Int. Ed.* **2016,** *55* (38), 11437.
42. Yu, W.; Sisi, L.; Haiyan, Y.; Jie, L., *RSC Adv.* **2020,** *10* (26), 15328.
43. Brill, A. R.; Koren, E.; de Ruiter, G., *J. Mater. Chem. C* **2021,** *9* (35), 11569.
44. Thurakkal, S.; Zhang, X., *Adv. Sci.* **2020,** *7* (2), 1902359.
45. Martín, N.; Tagmatarchis, N.; Wang, Q. H.; Zhang, X., *Chem. Eur. J.* **2020,** *26* (29), 6292.
46. Ryder, C. R.; Wood, J. D.; Wells, S. A.; Yang, Y.; Jariwala, D.; Marks, T. J.; Schatz, G. C.; Hersam, M. C., *Nat. Chem.* **2016,** *8* (6), 597.
47. Thurakkal, S.; Zhang, X. Y., *Mater. Chem. Front.* **2021,** *5* (6), 2824.
48. Zhao, Y.; Tong, L.; Li, Z.; Yang, N.; Fu, H.; Wu, L.; Cui, H.; Zhou, W.; Wang, J.; Wang, H.; Chu, P. K.; Yu, X.-F., *Chem. Mater.* **2017,** *29* (17), 7131.
49. van Druenen, M.; Davitt, F.; Collins, T.; Glynn, C.; O'Dwyer, C.; Holmes, J. D.; Collins, G., *Chem. Mater.* **2018,** *30* (14), 4667.
50. Hu, H.; Gao, H.; Gao, L.; Li, F.; Xu, N.; Long, X.; Hu, Y.; Jin, J.; Ma, J., *Nanoscale* **2018,** *10* (13), 5834.
51. Sofer, Z.; Luxa, J.; Bouša, D.; Sedmidubský, D.; Lazar, P.; Hartman, T.; Hardtdegen, H.; Pumera, M., *Angew. Chem. Int. Ed.* **2017,** *56* (33), 9891.
52. Zhang, L.; Wang, Z.-J.; Ma, B.; Li, X.-Y.; Dai, Y.-C.; Hu, G.; Peng, Y.; Wang, Q.; Zhang, H.-L., *Chin. Chem. Lett.* **2022,** *33* (10), 4640.
53. Liu, Y.; Gao, P.; Zhang, T.; Zhu, X.; Zhang, M.; Chen, M.; Du, P.; Wang, G.-W.; Ji, H.; Yang, J.; Yang, S., *Angew. Chem. Int. Ed.* **2019,** *58* (5), 1479.
54. Abellán, G.; Neiss, C.; Lloret, V.; Wild, S.; Chacón-Torres, J. C.; Werbach, K.; Fedi, F.; Shiozawa, H.; Görling, A.; Peterlik, H.; Pichler, T.; Hauke, F.; Hirsch, A., *Angew. Chem. Int. Ed.* **2017,** *56* (48), 15267.

55. Jin, M. Y.; Zhen, Q.; Xiao, D.; Tao, G.; Xing, X.; Yu, P.; Xu, C., *Nat. Commun.* **2022,** *13* (1), 3276.
56. Zhao, B.; Liu, P.-W.; Liu, D.-Y.; Kolibaba, T. J.; Zhang, C.-Y.; Liu, Y.-T.; Liu, Y.-Q., *Macromol. Mater. Eng.* **2019,** *304* (8), 1900164.
57. Cheng, Y.; Xie, Y.; Cao, H.; Li, L.; Liu, Z.; Yan, S.; Ma, Y.; Liu, W.; Yue, Y.; Wang, J.; Gao, Y.; Li, L., *J. Chem. Eng.* **2023,** *453*, 139823.
58. Arunan, E.; Desiraju, G. R.; Klein, R. A.; Sadlej, J.; Scheiner, S.; Alkorta, I.; Clary, D. C.; Crabtree, R. H.; Dannenberg, J. J.; Hobza, P.; Kjaergaard, H. G.; Legon, A. C.; Mennucci, B.; Nesbitt, D. J., *Pure Appl. Chem.* **2011,** *83* (8), 1619.
59. Abellán, G.; Wild, S.; Lloret, V.; Scheuschner, N.; Gillen, R.; Mundloch, U.; Maultzsch, J.; Varela, M.; Hauke, F.; Hirsch, A., *J. Am. Chem. Soc.* **2017,** *139* (30), 10432.
60. Aykol, M.; Doak, J. W.; Wolverton, C., *Phys. Rev. B* **2017,** *95* (21), 214115.
61. Mekuye, B.; Abera, B., *Nano Sel.* **2023,** *4* (8), 486.
62. Favron, A.; Gaufrès, E.; Fossard, F.; Phaneuf-L'Heureux, A.-L.; Tang, N. Y. W.; Lévesque, P. L.; Loiseau, A.; Leonelli, R.; Francoeur, S.; Martel, R., *Nat. Mater.* **2015,** *14* (8), 826.
63. Shutt, R. R. C.; Ramireddy, T.; Stylianidis, E.; Di Mino, C.; Ingle, R. A.; Ing, G.; Wibowo, A. A.; Nguyen, H. T.; Howard, C. A.; Glushenkov, A. M.; Stewart, A.; Clancy, A. J., *Chem. Eur. J.* **2023,** *29* (55), e202301232.
64. Kang, J.; Wood, J. D.; Wells, S. A.; Lee, J.-H.; Liu, X.; Chen, K.-S.; Hersam, M. C., *ACS nano* **2015,** *9* (4), 3596.
65. Paolucci, V.; D'Olimpio, G.; Lozzi, L.; Mio, A. M.; Ottaviano, L.; Nardone, M.; Nicotra, G.; Le-Cornec, P.; Cantalini, C.; Politano, A., *ACS Sustain. Chem. Eng.* **2020,** *8* (51), 18830.
66. Lee, G.; Lee, J.-Y.; Lee, G.-H.; Kim, J., *J. Mater. Chem. C* **2016,** *4* (26), 6234.
67. Smith, J. B.; Hagaman, D.; Ji, H.-F., *Nanotechnology* **2016,** *27* (21), 215602.
68. Xu, Y.; Shi, X.; Zhang, Y.; Zhang, H.; Zhang, Q.; Huang, Z.; Xu, X.; Guo, J.; Zhang, H.; Sun, L.; Zeng, Z.; Pan, A.; Zhang, K., *Nat. Commun.* **2020,** *11* (1), 1330.
69. Zhao, Y.; Mao, J.; Wu, Z.; Io, W. F.; Pang, S.-Y.; Zhao, Y.; Hao, J., *Nat. Commun.* **2024,** *15* (1), 6795.
70. Yau, S.-L.; Moffat, T. P.; Bard, A. J.; Zhang, Z.; Lerner, M. M., *Chem. Phys. Lett.* **1992,** *198* (3), 383.
71. Zhan, T.-G.; Zhou, T.-Y.; Lin, F.; Zhang, L.; Zhou, C.; Qi, Q.-Y.; Li, Z.-T.; Zhao, X., *Org. Chem. Front.* **2016,** *3* (12), 1635.
72. Ding, J.; Zheng, C.; Wang, L.; Lu, C.; Zhang, B.; Chen, Y.; Li, M.; Zhai, G.; Zhuang, X., *J. Mater. Chem. A* **2019,** *7* (41), 23337.
73. Stuart, A. M.; Merfield, C. N.; Horgan, F. G.; Willis, S.; Watts, M. A.; Ramírez-Muñoz, F.; U, J. S.; Utyasheva, L.; Eddleston, M.; Davis, M. L.; Neumeister, L.; Sanou, M. R.; Williamson, S., *Environ. Sci. Pollut. Res. Int.* **2023,** *30* (7), 16984.
74. Bockman, T. M.; Kochi, J. K., *J. Org. Chem.* **1990,** *55* (13), 4127.
75. Peon, J.; Tan, X.; Hoerner, J. D.; Xia, C.; Luk, Y. F.; Kohler, B., *J. Phys. Chem. A* **2001,** *105* (24), 5768.
76. Striepe, L.; Baumgartner, T., *Chem. Eur. J.* **2017,** *23* (67), 16924.
77. Cheng, W.-C.; Kurth, M. J., *Org. Prep. Proced. Int.* **2002,** *34* (6), 585.
78. Teixeira, R. I.; Garden, S. J.; de Lucas, N. C., *J. Photochem. Photobiol. A Chem.* **2020,** *401*, 112777.
79. Isukapalli, S. V. K.; Vennapusa, S. R., *J. Photochem. Photobiol. A Chem.* **2023,** *441*, 114695.
80. Kawano, S.-i.; Baumgarten, M.; Chercka, D.; Enkelmann, V.; Müllen, K., *Chem. Commun.* **2013,** *49* (44), 5058.

81. Nokami, T.; Matsuo, T.; Inatomi, Y.; Hojo, N.; Tsukagoshi, T.; Yoshizawa, H.; Shimizu, A.; Kuramoto, H.; Komae, K.; Tsuyama, H.; Yoshida, J.-i., *J. Am. Chem. Soc.* **2012,** *134* (48), 19694.
82. Carlsen, P. H. J.; Katsuki, T.; Martin, V. S.; Sharpless, K. B., *J. Org. Chem.* **1981,** *46* (19), 3936.
83. Sarkar, I.; Guo, C.; Peng, C.; Wang, Y.; Li, Y.; Zhang, X., *Small* **2025**, 2410300.
84. Huang, Y.; Qiao, J.; He, K.; Bliznakov, S.; Sutter, E.; Chen, X.; Luo, D.; Meng, F.; Su, D.; Decker, J.; Ji, W.; Ruoff, R. S.; Sutter, P., *Chem. Mater.* **2016,** *28* (22), 8330.
85. Yang, S.; Chen, G.; Ricciardulli, A. G.; Zhang, P.; Zhang, Z.; Shi, H.; Ma, J.; Zhang, J.; Blom, P. W. M.; Feng, X., *Angew. Chem. Int. Ed.* **2020,** *59* (1), 465.
86. Wei, Z.; Shin, W.; Jiang, H.; Wu, X.; Stickle, W. F.; Chen, G.; Lu, J.; Alex Greaney, P.; Du, F.; Ji, X., *Nat. Commun.* **2019,** *10* (1), 3227.
87. Sexton, B. A.; Avery, N. R., *Surf. Sci.* **1983,** *129* (1), 21.
88. Hultgren, R.; Gingrich, N. S.; Warren, B. E., *J. Chem. Phys.* **1935,** *3* (6), 351.

Paper I

RESEARCH ARTICLE

NANO · MICRO small
www.small-journal.com

Boosting 2D Black Phosphorus Ambient Stability: Noncovalent Functionalization Using Viologen Molecules

*Ishan Sarkar, Cong Guo, Cheng Peng, Yu Wang, Yafei Li, and Xiaoyan Zhang**

Black phosphorus nanosheets (BPNSs) have recently emerged as a valuable addition to the diverse family of 2D materials, holding promises for a wide range of applications. However, their practical use is limited by poor stability under ambient conditions, as they degrade quickly when exposed to light, air, or moisture. Noncovalent functionalization offers a promising approach to address these challenges. Herein, viologen derivatives are incorporated into a BPNS suspension in acetonitrile, resulting in the formation of two hybrid materials. These hybrids are subsequently stored under ambient conditions to track their degradation over time. The degradation behavior of these functionalized BPNSs is analyzed and compared to that of pristine BPNSs stored in both nitrogen and ambient environments, using X-ray photoelectron spectroscopy. Interestingly, the two viologen-based hybrid systems exhibited varying degrees of ambient protection efficiency, attributed to differences in their average adsorption energies and aggregation kinetics with BPNSs. Methyl viologen-functionalized BPNSs showed markedly reduced degradation in ambient conditions, with less pronounced differences for samples stored in a protected environment. This study introduces a promising strategy for enhancing the stability of BPNSs, making them more resistant to decomposition and potentially suitable for energy storage applications and optoelectronic devices.

1. Introduction

Over the past decade, 2D materials including graphene, transition metal dichalcogenides, and BPNSs, have attracted significant attention from researchers worldwide.[1–3] Their ability to manifest characteristics of the quantum realm in macroscopic dimensions has paved the way for modern technology.[4,5] Among all of them, 2D BPNSs, being relatively recent and having distinctive properties such as thickness dependent tunable direct band gap,[6,7] high charge-carrier mobility[8] and strong in plane anisotropy,[9] have found inherent applications in photocatalysis,[10–12] energy storage,[12,13] semiconductor-electronics,[12,14,15] optoelectronics,[12,16,17] sensing and biomedicines.[18]

Despite the extraordinary characteristics, the practical relevance of BPNSs is significantly limited by their poor stability under ambient conditions, primarily due to chemical degradation when exposed to light, air, and moisture.[19] The high affinity of phosphorus atoms for oxygen, driven by the strong bond-dissociation energy, accelerates this degradation process. It is hypothesized that degradation begins with a light-dependent initiation process, where the nanosheets generate superoxide radical anions, leading to the formation of peroxide linkages (**Figure 1**) on the nanosheets. This is followed by a propagation process, in which surrounding water molecules interact, ultimately resulting in the formation of phosphoric acid.[20,21]

To date, some efforts have been made to address the issue of ambient instability by mitigating one or more of the three factors contributing to the degradation process, generally categorized as covalent and noncovalent approaches, depending on whether chemical bonding is involved.[22] Each passivation method offers distinct advantages and trade-offs, with the choice depending on the target application—such as optoelectronics, sensing, or field-effect transistors (FETs)—and the specific type of 2D material involved. The properties of hybrid nanosheets after passivation depend on the substrate and the intended effect of the process. Covalent functionalization has provided itself as a promising strategy for stabilization with new and improved physicochemical properties. Surface modification and passivation of BPNSs via covalent bond formation can be performed through diazonium salt chemistry as shown by Ryder et al.[23] Porphyrin functionalized BPNSs prepared though diazonium chemistry has provided significant protection against ambient degradation along with interesting photophysical properties.[24] However, diazonium chemistry also carries the risk of a single-electron transfer process,

I. Sarkar, C. Peng, X. Zhang
Department of Chemistry and Chemical Engineering
Chalmers University of Technology
Kemigården 4, Göteborg SE-412 96, Sweden
E-mail: xiaoyan.zhang@chalmers.se

C. Guo, Y. Wang, Y. Li
Jiangsu Collaborative Innovation Centre of Biomedical Functional Materials
School of Chemistry and Materials Science
Nanjing Normal University
Nanjing 210023, P. R. China

The ORCID identification number(s) for the author(s) of this article can be found under https://doi.org/10.1002/smll.202410300

DOI: 10.1002/smll.202410300

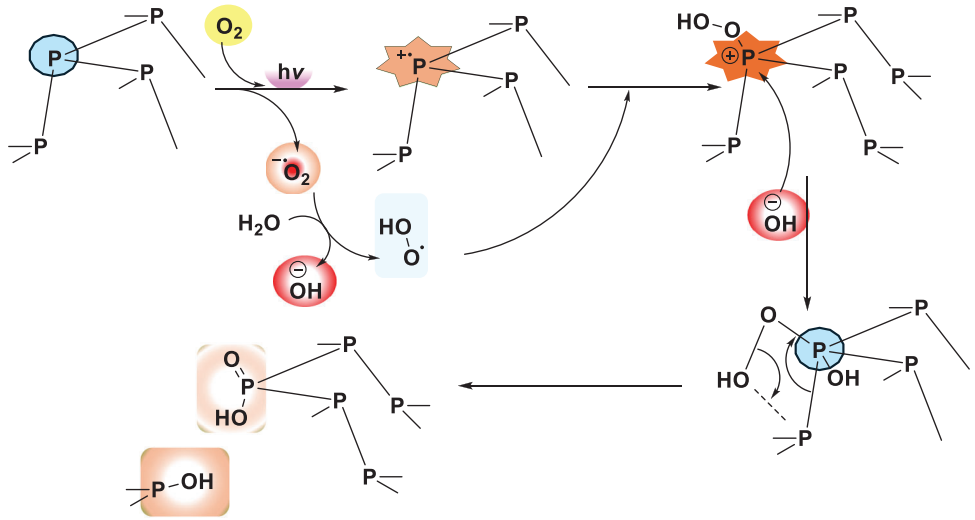

Figure 1. Plausible degradation mechanism of BPNSs under aerobic and light exposure.

where electrons from the nanosheets transfer to the charged nitrogen species in diazonium salts. This leads to a high density of unpaired electrons on the nanosheet surface, ultimately causing interface amorphization as the system minimizes energy, resulting in red phosphorus-like structures.[25] Aryl-iodonium salts[26] and nucleophilic reagents[27] also open a vast field of covalent modification. Azide based functionalization methods have been developed, which involve the formation of nitrene intermediates to establish P═N bonds. This approach has demonstrated significant improvements in ambient stability for the BPNSs.[28] Wang et al.[29] showed that when BPNSs are functionalized covalently using graphitic carbon nitrides, the P—N bonds can help regulating electron transfer processes from BPNSs to the carbon nitride moieties. This functionalization enables their use as controlled oxygen electrocatalysts and facilitates their utility as valuable components in zinc–air batteries (ZABs). Kuchkaev et al. showed that P—C bonds can directly be formed through carbene generation from chloroform by strong bases, e.g., potassium tert-butoxide.[30] Compared to non-covalent functionalization, covalent functionalization was performed at lower concentrations to obtain a lower degree of functionalization, thus minimizing the detrimental increase in off current.[23] A moderate level of covalent functionalization can potentially enhance the stability and optimize the properties of BPNSs.[17]

Non-covalent functionalization leverages van der Waals interactions to passivate the conduction band of BPNSs, effectively halting the formation of superoxide radicals.[17] Redox-active electron-deficient hydrophobic anthraquinone has been employed by Pumera and co-workers[31] to interact with BPNSs through van der Waals interactions, thus enhancing the charge storage capacity of the hybrid material. AlO_x, initially used to passivate the BPNS surface and enhance the nanosheets' mobility and on/off ratio over time,[20] was later found to increase the barrier potential for charge diffusion and electromigration at the grain boundaries when applied to graphene, leading to improved conductivity under high-current treatment.[32] Ag^+ ions have been deployed to interact with the bare lone pairs of BPNSs through noncovalent interactions, which can enhance both the ambient stability and transistor performance of the exfoliated BPNSs.[33] Previous theoretical calculations by Zhao et al. demonstrated that the self-assembly of perylene-3,4,9,10-tetracarboxylic dianhydride on BPNS surfaces via van der Waals interactions can effectively shield the surface from oxidation while preserving the electronic band structure of BPNSs.[34] This essentially implies that non-covalent modification has a significantly smaller impact on the electronic structure of the nanosheets.

Viologens and their derivatives are a class of molecules derived from 4,4′-bipyridylium salts, characterized by rigid π-electron deficient structures. They are well-known for their exceptional reversible redox properties, which are crucial for various energy storage applications.[35] The term "viologen" is derived from their capacity to produce a violet color upon reduction. The reduction process of viologens, which possess an extended π-system, typically involves multiple radical-cation intermediates that can be resonance-stabilized.[36] The radical cation generated upon reduction is intensely colored which makes it an outstanding candidate for electrochromic systems. Herein, two viologen derivatives with extended π-systems have been employed to passivate the electronically dense surface of the BPNSs (**Figure 2**).

2. Results and Discussion

To test the hybrid formation, titration of the BPNSs by viologen derivatives were performed in acetonitrile and the experiments were monitored by UV–vis absorption spectroscopy. The peak molecular absorbance in acetonitrile was recorded at 256 nm for methyl viologen (MV). Red shifts in the absorption peak to 259 nm were observed for the MV samples (1 mg mL^{-1}) with the gradual addition of a fixed amount of BPNSs (1.75 mL of 0.143 mg mL^{-1} dispersion), as shown in **Figure 3**. The shift of the absorption peak suggests that there might be interactions between the MV molecules and BPNSs in the hybrid material, which can further be verified by the formation of precipitates. During titration, the addition of the molecular solution induces aggregate formation, altering the pre-existing scattering behavior

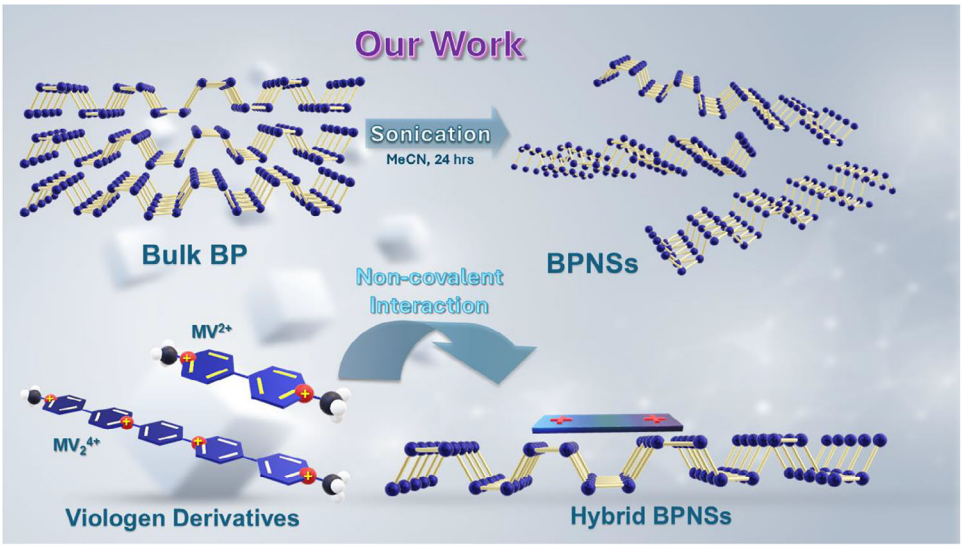

Figure 2. Schematic representation of non-covalent functionalization between BPNSs and viologen derivatives.

of BPNSs. After normalizing the peak absorbance in the range of 214–330 nm, the peak shift persists without significant broadening, as shown in Figure S4 (Supporting Information). The molecular absorption offset was similar to that of the hybrids, indicating that the broadening seen in the unprocessed plots was likely due to scattering from the hybrid aggregates. It is noteworthy that, when scaled up, the precipitation rate for the MV-BPNS hybrid remained consistent. The Zeta potential study presented further insight on the charge-neutralization point of BPNSs when the MV molecules (13.2 mg mL^{-1}, 10 µL each time) were gradually added to a fixed amount of a BPNS dispersion (0.29 mg mL^{-1}, 700 µL) in water. The zeta potential of the BPNSs was observed to be −33 mV when no titrant was added, however, upon addition of the MV molecules to the BPNSs, the zeta potential was observed to shift toward less negative value. The saturation point was observed at a mass fraction of 0.86 for MV (Figure 3) where the zeta potential within the hydrodynamic radius of the hybrids was mostly neutralized. More addition of the MV molecules results in slightly positive values and at the mass fraction of 0.89 for MV, the zeta potential was observed to be +2.1 mV.

FTIR spectra were recorded for the MV and was compared to pure BPNSs and the MV-BPNS hybrid by employing attenuated total reflectance (ATR) measurement. The C–H out-of-plane bending vibration of the terminal methyl groups can be observed at 818 cm^{-1} for MV, which is absent in the spectrum for the bare BPNSs. In the hybrid material, the out-of-plane bending mode shifted to 833 cm^{-1} (**Figure 4**), indicating a restriction in the MV's out-of-plane bending modes due to its stacking on the BPNS surface. The shift in the FTIR spectra suggests potential interactions between the MV molecules and BPNSs.

Mean Raman spectra were recorded using a 532 nm excitation laser and the mean Raman spectra was obtained by averaging the data thus obtained. The BPNSs show three prominent sharp peaks which correspond to the out-of-plane symmetric phonon mode A^1_g at 362 cm^{-1}, the in-plane modes B_{2g} at 437 cm^{-1} and A^2_g at 468 cm^{-1}.[24,37,38] After noncovalent functionalization, all

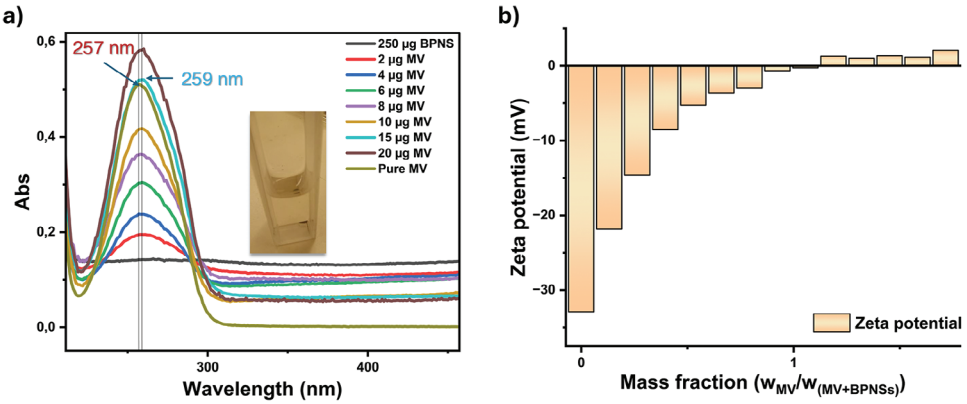

Figure 3. Titrimetric studies indicate the interaction between the MV molecules and BPNSs. a) UV–vis absorption and b) Zeta potential measurements. The absorbance of a 3.01 mL solution containing 0.0138 mg mL^{-1} of $MV(PF_6)_2$ in acetonitrile was measured for comparison. Zeta potential measurements were performed by adding MV molecules to BPNSs dispersed in water.

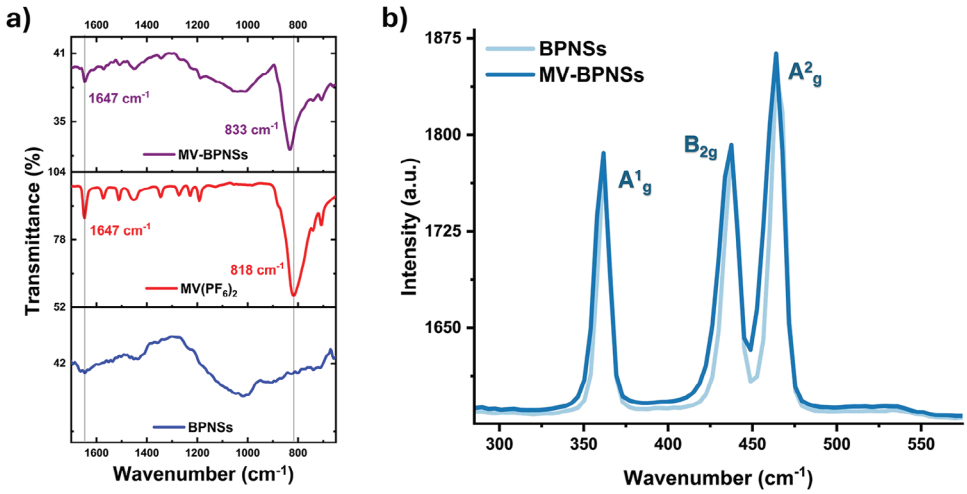

Figure 4. Studies indicate the interactions between the MV molecules and BPNSs. a) ATR-IR, b) Mean Raman spectra of BPNSs and MV-BPNSs measured using a 532 nm laser excitation. Blue shift in the IR for the out-of-plane bending modes at 818 cm^{-1} from the terminal methyl groups of the MV molecules suggests the possible interactions between the two components in the hybrid.

the peaks for their respective vibrational modes were preserved in the MV-BPNS hybrid (Figure 4b). The average Raman spectra, derived from over 20 measurements for each sample, revealed A^1g to A^2_g intensity ratios of 0.719 for BPNSs and 0.716 for MV-BPNSs, indicating a minimal oxidation rate throughout the MV-BPNS hybrid preparation.[39]

To predict the properties and interaction of the viologen derivatives with BPNSs, density functional theory (DFT) studies were employed. The energy levels of the highest occupied molecular orbitals (HOMO) and lowest unoccupied molecular orbitals (LUMO) were calculated. The HOMO levels were determined to be −2.65 and −2.63 eV for MV and MV_2, respectively, while the LUMO levels were found to be −0.94 and −1.25 eV for the same. The HOMO-LUMO gaps were calculated to be 1.7 and 1.38 eV for MV and MV_2, respectively. The normalized adsorption energies were calculated for MV (**Table 1**) in the direction parallel, perpendicular and diagonally to the ridges of BPNSs (MV_2-BPNSs: Table S1, Supporting Information). For the MV_2-BPNS hybrid, the normalized adsorption energy value was found to be lower (−0.0472 eV) than that of the MV-BPNS hybrid (−0.0518 eV), which explains the slower precipitation speed of MV_2-BPNS upon mixing (Table 1). DFT calculations also predicted partial charge transfer processes, with the extent of charge transferred from the BPNSs to the viologen derivatives measured at 0.73*e* and 1.75*e* for the MV-BPNS and MV_2-BPNS hybrids, respectively, along the parallel direction of the BPNS ridges (**Figure 5**). DFT calculation results suggest the presence of possible cation-induced dipole interactions between the MV molecules and BPNSs. Further calculations on the oxygen adsorption on the nanosheet surfaces revealed more information on the degradation mechanism. A previous study demonstrated that O_2 readily dissociated on the black phosphorus surface.[40] The adsorption of O_2 at various sites under MV coverage was calculated, revealing that O_2 similarly underwent spontaneous dissociation into two oxygen atoms (Figure S7, Supporting Information). As a result, the free energy of adsorption of the O atom was employed as the criterion for evaluating the ease of BPNS oxidation in all subsequent analyses. The Gibbs free energy for the oxygen atom adsorption was calculated for the surfaces of pure BPNSs, MV- and MV_2-BPNS hybrids. Interestingly, the calculated adsorption free energy increased by 0.04 and 0.02 eV for the MV- and MV_2-BPNS hybrids, respectively, compared to the pure BPNSs (Figures S8–S11, Supporting Information). This suggests that oxygen adsorption is more favorable and likely to occur spontaneously on pure BPNSs, whereas it is comparatively less probable on the MV-BPNS hybrids. The calculation, however, did not account for the excitonic pairs generated on the nanosheets under light exposure or the charged superoxide radical anion species formed through electron transfer from the conduction band of the nanosheets to molecular oxygen.

Table 1. Total and average adsorption energy of the MV-BPNSs hybrids along different directions from the ridges of BPNSs calculated by DFT.

Materials [MV-BPNSs]	E_{ads} [eV]	Number of atoms [X]	E_{ads}/X [eV]
Perpendicular	−1.45	28	−0.0518
Parallel	−1.47	28	−0.0524
Diagonal	−1.44	28	−0.0516

SEM was performed to investigate the surface morphology of the bare BPNSs and the viologen-BPNS hybrids. To compare the hybrids, SEM imaging of the viologen derivatives were also recorded. Viologen derivatives exhibited a 3D morphology characterized with distinct solid, block-like features (**Figure 6**b,c), with rod-like structures observed for MV (Figure 6b). The bare BPNSs showed flakes of nanosheets (Figure 6a–d), which was preserved in the MV-BPNS hybrid (Figure 6e,f) along with large solid features scattered throughout the samples, indicating that the noncovalent functionalization process minimally impacts the overall morphology. The scale bars in Figure 6b,c were deliberately kept large to highlight the difference in aspect ratios between the molecular 3D features and the nanosheets' dimensions.

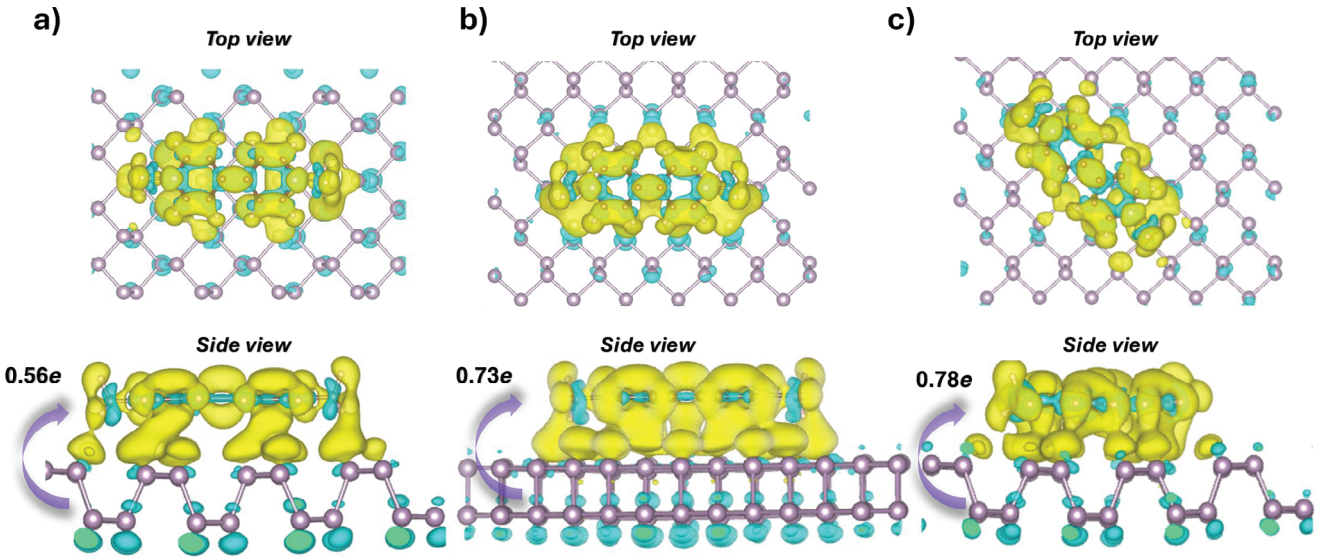

Figure 5. Charge difference plots of the MV molecules on top of a single-layer BPNS surface. a) perpendicular to the ridge, b) parallel to the ridge, c) diagonal to the ridge. Orbital overlap scenarios for the MV-BPNS hybrids in each direction are shown as the side view located under each consecutive illustration. The yellow region represents areas of electron accumulation, while the cyan region indicates areas of electron depletion.

Furthermore, a closer look on the exfoliated and the functionalized BPNSs through transmission electron microscopy (TEM) and high-resolution TEM (HR-TEM) uncovered information on the lattice parameters of the sheets. **Figure** 7a shows the morphology of a few-layer BPNS, highlighting its structural features. The lattice fringes for the (111)[41] plane and the (014) plane[24] can be observed for the bare BPNSs with d-spacings of ≈2.5 and 2.2 Å, respectively (Figure 7c). The (111) plane of BPNSs can be observed with the d-spacing value of 2.5 Å in the MV-BPNS hybrids, suggesting the unaffected crystallinity of BPNSs through the non-covalent functionalization process (Figure 7d). It is worth mentioning that the MV-BPNS hybrid displayed an aggregated morphology (Figure 7b; Figure S5b,c, Supporting Information), consistent with observations from UV titration and large-scale sample preparation for IR, Raman, and XPS measurements. In contrast to this observation, the MV_2-BPNS hybrid did not show an aggregated morphology (Figure S12c, Supporting Information) as the MV_2 molecules passed through the TEM

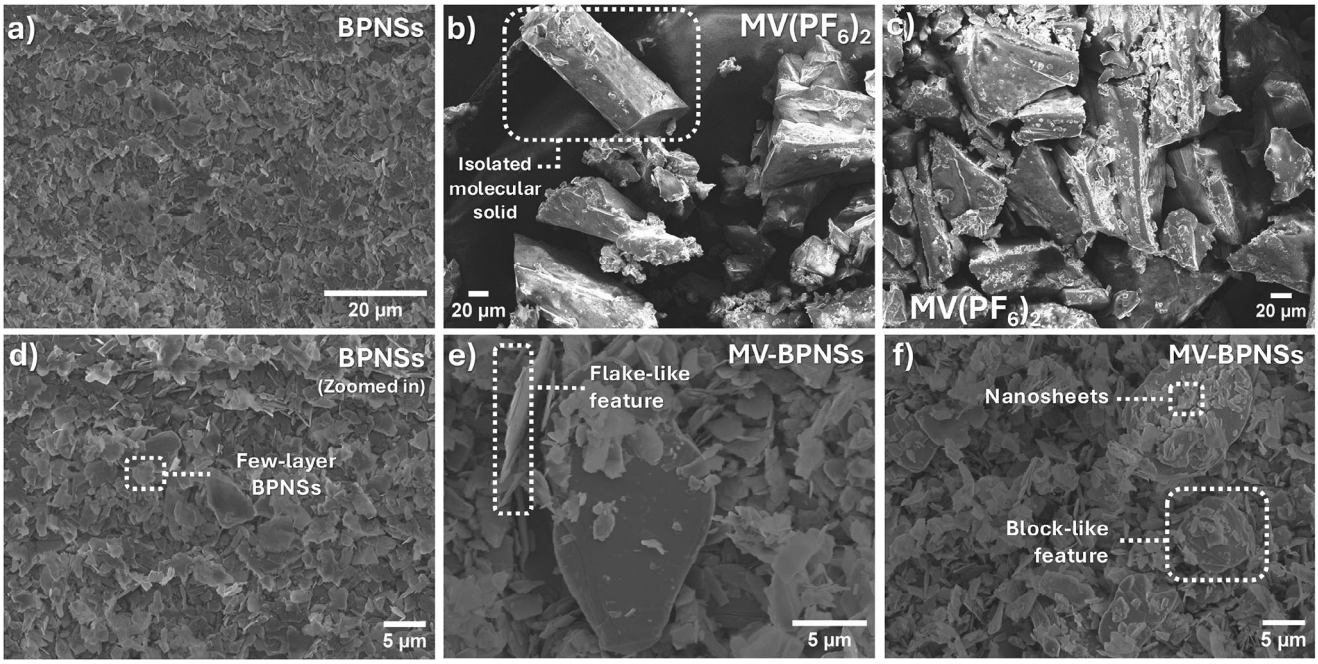

Figure 6. SEM images of a) BPNSs, b,c) $MV(PF_6)_2$, d) BPNSs (zoomed in) and e,f) the $MV(PF_6)_2$-BPNS hybrids.

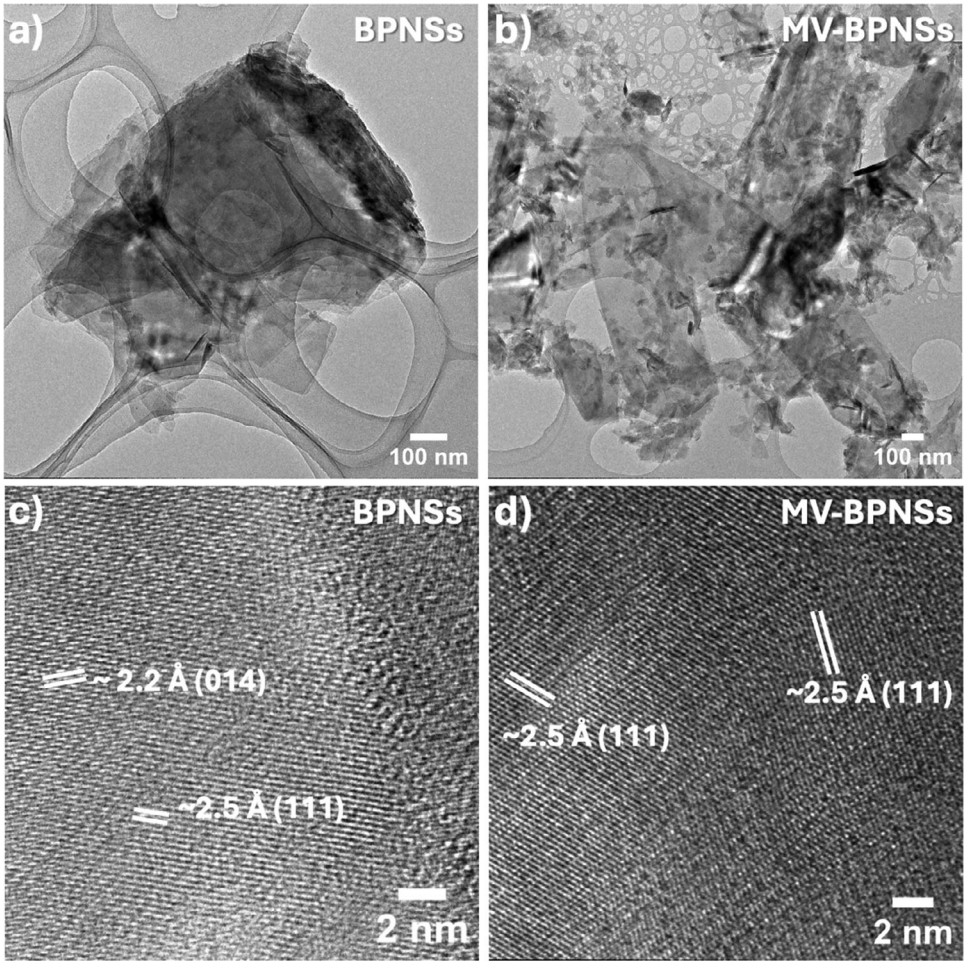

Figure 7. TEM and HR-TEM images of a,c) BPNSs and b,d) the $MV(PF_6)_2$-BPNS hybrids.

grid due to their lower adsorption energy and slower aggregation kinetics.[42]

The ambient stability of the BPNSs and the hybrid materials were compared using X-ray photoelectron spectroscopy (XPS), as shown in **Figure 8**. A control experiment was conducted by storing pristine BPNSs and MV-BPNS hybrids under nitrogen atmosphere for 6 days, while identical samples were kept under ambient conditions for the same duration. This procedure was repeated multiple times to ensure consistency.[43] The core-level P2p intensities were plotted against binding energy, revealing four fitted peaks for BPNSs under protected conditions at 129.69, 130.53, 133.23, and 134.47 eV (Figure 8a, **Table 2**), corresponding to $P2p_{3/2}$, $P2p_{1/2}$, P—O and P═O, respectively. In the MV-BPNS hybrid under protected conditions, the respective P signals were observed at 129.62, 130.46, 133.35, and 134.24 eV (Figure 8c, Table 2). The P2p intensity of P-F for MV-BPNSs could not be traced due to the low requirement of the MV molecule to form the hybrid, however, the molecular signal of N1s can still be traced in both the survey scan and the high-resolution spectra (Figures S13 and S14, Supporting Information). For BPNSs and MV-BPNSs kept under ambient conditions, the $P2p_{3/2}$, $P2p_{1/2}$, P—O and P═O peaks can be observed at 129.71, 130.55, 132.83, 133.97 eV and 129.73, 130.57, 133.39, 134.30 eV (Figure 8b–d and Table 2). For the samples stored under ambient conditions, a significant increase in the P—O/P ═O content was observed in the BPNSs (163%, Figure 8b). In contrast, the average increase in the P—O/P═O content for the MV-BPNS hybrid was significantly lower (24%, Figure 8d). Repeated measurements confirmed a higher degree of oxidation in the BPNSs compared to the MV-BPNS hybrids under similar experimental conditions, as shown in **Figure 9**. However, the MV-BPNS hybrid exhibited minimal degradation, showing the least change in the P—O/P═O content. Additionally, based on the atomic ratio between phosphorus and nitrogen in the XPS measurement, the noncovalent functionalization degree for the MV-BPNS hybrid is calculated to be every ≈21 phosphorus atoms having one MV molecule. The proposed mechanism for the enhanced ambient stability of the hybrid may stem from a decrease in surface electron density of the BPNSs, likely due to encapsulation by the MV molecules. This encapsulation could effectively block oxygen and water molecules from accessing the BPNS surface.

Another viologen derivative ($MV_2(PF_6)_4$: Scheme S1 (Supporting Information) was also employed to address the ambient stability issues associated with BPNSs. Titrimetric studies using UV–vis absorption spectroscopy suggests the interaction between the MV_2 molecules and BPNSs, where the absorption peak

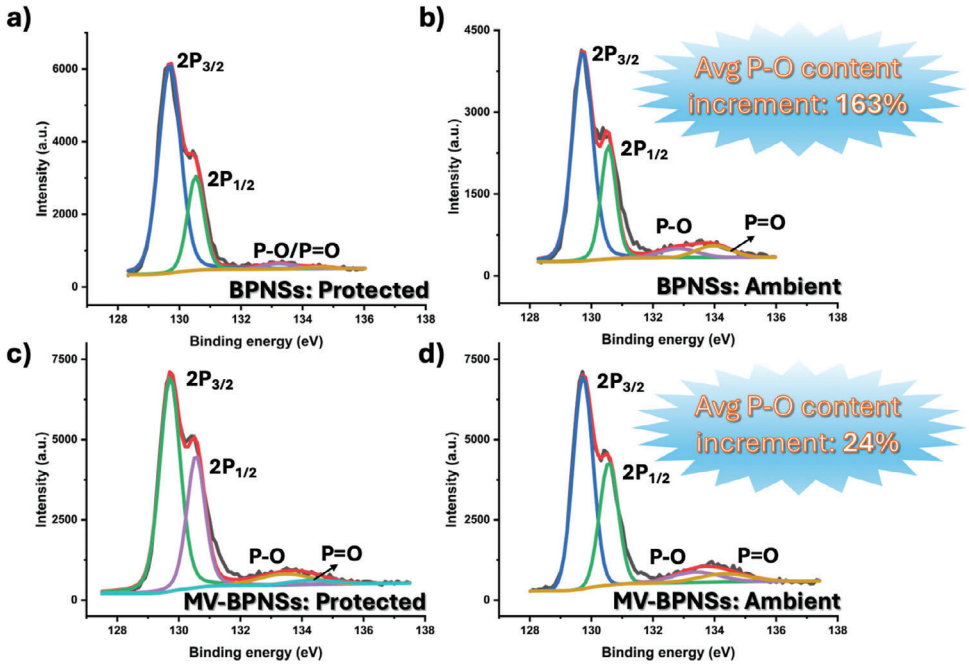

Figure 8. P2p XPS spectra of a,b) BPNS under protected and ambient conditions. c,d) MV-BPNS hybrids under protected and ambient conditions.

of MV_2 was observed to be shifted from 287 to 291 nm (Figure S6, Supporting Information), upon the gradual addition of the MV_2 molecule (1 mg mL^{-1}) to a fixed concentration of BPNSs (1.7 mL of 0.118 mg mL^{-1} dispersion). However, the precipitate formation observed in this experiment did not translate effectively to large-scale sample preparation, likely due to slower aggregation kinetics at higher concentrations and the potential presence of a dynamic adsorption-desorption process. ATR-IR measurements (Figure S9, Supporting Information) also showed a shift in the C–H out-of-plane bending mode in the hybrid from 818 to 837 cm^{-1} referring to the possible interactions between the MV_2 molecules and BPNSs. SEM images showed flake-like features of BPNSs alongside occasional scattered bulk features. The flake features of BPNSs in the hybrids were further confirmed by a d-spacing of 2.2 Å for the (014) plane (Figure S12, Supporting Information) observed in the HR-TEM measurements, with no distortion from aggregation, likely owing to the lower adsorption energy and slower aggregation kinetics. The ambient stability of the hybrids was also evaluated using XPS measurements (Figure S15, Supporting Information). However, due to the weak interaction and slow aggregation kinetics between the MV_2 molecules and BPNSs, a high loading of MV_2 molecules is required to form the hybrid, leading to inhomogeneity across the hybrids. The peaks for the MV_2-BPNS hybrids stored in the protected conditions at 129.63, 130.47, 133.38, 134.28, 136.57 eV (Figure S15a, Table S2, Supporting Information) and 129.04, 129.88, 133.31134.28 and 136.18 eV (Figure S15c, Table S2, Supporting Information) can be assigned to $P2p_{3/2}$, $P2p_{1/2}$, P—O, P═O and P–F.[24,44,45] The P–F peak was very intense in the case of the MV_2-BPNS hybrids, both in protected and ambient conditions, due to their weak

Table 2. P2p binding energies of BPNSs and MV-BPNS in XPS measurements.

Binding energy	BPNS-P [eV]	BPNS-A [eV]	MV-BPNS-P [eV]	M-BPNS-A [eV]
$P2p_{3/2}$	129.69	129.71	129.62	129.73
$P2p_{1/2}$	130.53	130.55	130.46	130.57
P–O	133.23	132.83	133.35	133.39
P = O	134.47	133.97	134.24	134.30

P-protected, A-ambient.

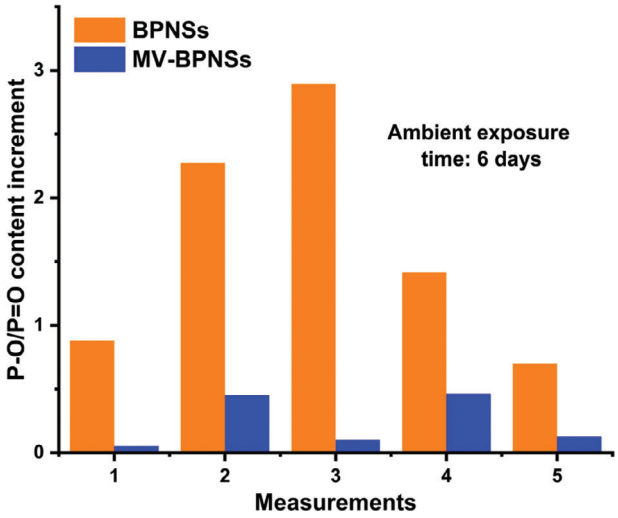

Figure 9. A comparison of the extent of oxidation between BPNSs and the MV-BPNS hybrids in various measurements over 6 days of ambient exposure.

interactions, high loading amount of MV_2 and inhomogeneity (Figure S15, Supporting Information).[46,47] For MV_2-BPNSs in ambient condition, the $P2p_{3/2}$, $P2p_{1/2}$, P—O, P═O and P–F peaks can be observed at 129.84, 130.68, 133.38, 134.28, 136.73 eV (Figure S15c, Table S2, Supporting Information) and 129.74, 130.58, 133.33, 134.23, and 136.92 eV (Figure S15d, Table S2, Supporting Information). The increase in the total P—O/P═O content for the MV_2-BPNS hybrid stored in ambient conditions varied significantly between samples, showing an approximate rise of 85% (from Figure S15a,b, Supporting Information) and up to 254% (from Figure S15c,d, Supporting Information), likely due to sample inhomogeneity.

3. Conclusion

In summary, two different viologen derivatives with 2 and 5 aromatic rings were successfully employed to passivate BPNS surface. The normalized adsorption energy was predicted using DFT calculations which directly correlates to the interactions of the viologen molecules with the BPNS surface and the interactions were supported by UV–vis absorption, FTIR and Raman spectroscopy. Contrary to our initial expectations, MV_2 formed weaker hybrids with BPNSs compared to MV, likely due to its lower average adsorption energy and slower aggregation kinetics, despite having a higher charge. The ambient stability efficiency was investigated using XPS studies by comparing the MV-BPNS hybrid to the pristine BPNSs in both protected and ambient conditions. BPNSs exhibited a higher oxidation tendency under aerobic conditions, even in their aggregated form, while the MV-BPNS hybrid showed minimal oxidation, consistent with DFT-based predictions, suggesting it as a potentially effective strategy for stabilizing BPNSs. Moreover, the non-covalent functionalization approach maintains a low degree of modification, as confirmed by XPS results, ensuring that the intrinsic properties of BPNSs remain largely intact. In contrast, the MV_2-BPNS hybrid showed inhomogeneity, resulting in an inconclusive protective effect. As this appears to be a novel observation, it represents a significant finding that warrants communication to the broader research community. This study introduces a promising approach to enhancing the stability of BPNSs, making them more resistant to decomposition and potentially useful in energy storage systems, such as batteries and supercapacitors.

4. Experimental Section

Chemicals and Materials: Black phosphorus (BP) was purchased from Smart Elements (≈99.998%) and methyl viologen dichloride was purchased from Sigma Aldrich (98%). The bulk BP and solvents were always kept inside in a glovebox. Transfer of solvents was carried out in a glovebox or nitrogen atmosphere. The solvent acetonitrile, dichloromethane and methanol were anhydrous and were purchased from Sigma–Aldrich. All the solvents were deoxygenated before the experiments unless otherwise mentioned.

Characterizations: Raman analysis was performed on a WITec alpha300 R confocal Raman microscopy system (excitation at 532 nm). XPS analysis was carried out on a PHI 5000 VersaProbe III Scanning XPS Microprobe and the spectra were processed using the PHI multiPak software. TEM and HR-TEM were performed on a FEI Tecnai T20 instrument at an acceleration voltage of 200 kV. ATR-IR spectra were recorded using a PerkinElmer Frontier Infrared Spectrometer with a GladiATR, diamond crystal design. UV–vis absorption spectra were recorded on a Varian Cary 50 Bio UV–vis spectrophotometer. ^{1}H NMR spectra of the molecules were recorded using a 600 MHz Bruker Avance NEO NMR spectrometer.

Ion-Exchange of Methyl Viologen: The reaction was performed by addition of excess ammonium hexafluorophosphate in a methyl viologen water solution (10 mg mL^{-1}) and the precipitate by centrifugation was collected with additional washing using DI water.

Preparation of BPNS: In a glove box, BP crystals (80 mg) were ground using a mortar and pestle and was transferred to a round bottom flask. The flask was filled with acetonitrile (60 mL) and was sonicated in 37 kHz for 24 h at 10–15 °C. The mixture was centrifugated at 10 °C at 3000 rpm for 30 min and the supernatant was collected separately to obtain single- and few-layer BPNSs.

Preparation of the MV-BPNS and MV_2-BPNS Hybrids: For the MV-BPNS hybrid, a BPNS dispersion in acetonitrile (5 mL, 0.14 mg mL^{-1}) was mixed with a MV solution (100 µL, 1 mg mL^{-1}) and the precipitate was isolated by centrifugation. To prepare the MV_2-BPNS hybrid, a BPNS dispersion in acetonitrile (5 mL, 0.14 mg mL^{-1}) was combined with a MV_2 solution (500 µL, 1 mg mL^{-1}). However, due to the absence of precipitate formation—attributable to the slower aggregation kinetics and lower average adsorption energy—acetonitrile was evaporated under a nitrogen atmosphere, resulting in inhomogeneity within the MV_2-BPNS hybrid.

Computational Methods: All first-principles calculations were implemented using the Vienna ab initio simulation package (VASP).[48,49] The Perdew, Burke, and Ernzerhof (PBE) functional of generalized gradient approximation (GGA) served to approximate exchange-correlation functions.[50,51] The projector-augmented wave (PAW) method was used to represent the core-valence electron interactions.[52,53] The cutoff energy of the plane-wave basis was set to 400 eV. The threshold for the convergence in the self-consistent field (SCF) was set to 10–5 eV and the ionic relaxation steps were stopped when the forces became smaller than 0.05 eV $Å^{-1}$. The dispersion interactions were achieved using Grimme's D3 method.[54] The BPNS model of the MV-BPNS and MV_2-BPNS hybrids were constructed by (6 × 4) and (10 × 4) black phosphorus supercells. The Monkhorst-Pack K point sampling mesh of 1 × 1 × 1 and 2 × 2 × 1 were chosen for geometry optimizations and electronic structure calculations, respectively. The vacuum space of the slabs was set as 18 Å to minimize the interaction between the periodic units. The ΔG was calculated from the equation: $\Delta G = \Delta E + \Delta ZPE - T\Delta S$, where ΔE refers to the electronic energy difference, ΔZPE and ΔS refer to the change of zero-point energy and entropy at room temperature, respectively. T refers to 298.15 K. The ΔG_{*O} was calculated from the equation: $\Delta G_{*O} = G_{*O} - G_{*} - G_{H_2O} + G_{H_2}$. In the above equation, ΔG_{*O} denotes the adsorption free energy of $^*O$, G_{*O} refers to the free energy of the substrate with an adsorbed O atom, G^* represents the free energy of the substrate, and G_{H2O} and G_{H2} denote the free energies of the H_2O and H_2 molecules, respectively.

Supporting Information

Supporting Information is available from the Wiley Online Library or from the author.

Acknowledgements

This work was financially supported by Stiftelsen Chalmers Tekniska Högskola, Adlerbertska Forskningsstiftelsen (C2021-1258, C 2023-0559), Carl Tryggers Stiftelse (CTS 22:2286), Olle Engkvists Stiftelse (227-0236), Swedish Foundation for International Cooperation in Research and Higher Education (IB 2020–8789), Göteborg Energi (Tänk:Om Stipendiet), Swedish Research Council starting grant (2020-04903), and 2D TECHVINNOVA competence Center (Ref. 2019-00068). Mangmang Shi is thanked for the assistance with the XPS measurement.

Conflict of Interest

The authors declare no conflict of interest.

Data Availability Statement

The data that support the findings of this study are available from the corresponding author upon reasonable request.

Keywords

ambient stability, black phosphorus, density functional theory, non-covalent functionalization, viologen derivatives

Received: November 1, 2024
Revised: January 30, 2025
Published online:

[1] K. S. Novoselov, A. K. Geim, S. V. Morozov, D. Jiang, Y. Zhang, S. V. Dubonos, I. V. Grigorieva, A. A. Firsov, *Science* **2004**, *306*, 666.
[2] Z. Li, H. Nameirakpam, E. Berggren, U. Noumbe, T. Kimura, E. Asakura, V. Gray, D. Thakur, T. Edvinsson, A. Lindblad, M. Kohda, R. B. Araujo, A. Rao, M. V. Kamalakar, *J. Am. Chem. Soc.* **2024**, *146*, 35146.
[3] X. Ling, H. Wang, S. Huang, F. Xia, M. S. Dresselhaus, *Proc. Natl. Acad. Sci* **2015**, *112*, 4523.
[4] R. K. Mishra, J. Sarkar, I. Chianella, S. Goel, H. Y. Nezhad, *Next Mater.* **2024**, *4*, 100217.
[5] A. C. Ferrari, F. Bonaccorso, V. Fal'ko, K. S. Novoselov, S. Roche, P. Bøggild, S. Borini, F. H. L. Koppens, V. Palermo, N. Pugno, J. A. Garrido, *Nanoscale* **2015**, *7*, 4598.
[6] W. Huang, J. Zhong, W. Sheng, A. Zhou, *J. Condens. Matter Phys.* **2023**, *36*, 075301.
[7] A. Cupo, P. M. Das, C. C. Chien, G. Danda, N. Kharche, D. Tristant, M. Drndic, V. Meunier, *ACS Nano* **2017**, *11*, 7494.
[8] R. Fang, X. Cui, C. Stampfl, S. P. Ringer, R. Zheng, *Phys. Chem. Chem. Phys.* **2020**, *22*, 2276.
[9] L. Henry, V. Svitlyk, M. Mezouar, D. Sifre, G. Garbarino, M. Ceppatelli, M. Serrano-Ruiz, M. Peruzzini, F. Datchi, *Nanoscale* **2020**, *12*, 4491.
[10] M. Habiba, B. Abdelilah, E. K. Abdallah, T. Abdelhafed, A. Ennaoui, E. M. Khadija, M. Omar, *RSC Adv.* **2021**, *11*, 16004.
[11] J. Ran, B. Zhu, S. Z. Qiao, *Angew. Chem., Int. Ed.* **2017**, *56*, 10373.
[12] H. Zhang, *ACS Nano* **2015**, *9*, 9451.
[13] C. M. Park, H. J. Sohn, *Adv. Mater.* **2007**, *19*, 2465.
[14] Y. Y. Illarionov, M. Waltl, G. Rzepa, T. Knobloch, J. S. Kim, D. Akinwande, T. Grasser, *npj 2D Mater. Appl.* **2017**, *1*, 23.
[15] M. V. Kamalakar, B. N. Madhushankar, A. Dankert, S. P. Dash, *Small* **2015**, *11*, 2209.
[16] Y. Deng, Z. Luo, N. J. Conrad, H. Liu, Y. Gong, S. Najmaei, P. M. Ajayan, J. Lou, X. Xu, P. D. Ye, *ACS Nano* **2014**, *8*, 8292.
[17] K. Du, Q. Lv, Z. Liang, G. Liu, S. Hussain, J. Liu, G. Qiao, *ACS Appl. Nano Mater.* **2023**, *6*, 3159.
[18] G. A. Nowsherwan, M. Khan, M. A. Iqbal, N. Nowsherwan, M. Ahmad, S. Haider, T. Ali, K. Morsy, S. S. Hussain, *Inorg. Chem. Commun.* **2024**, *160*, 111912.
[19] S. Thurakkal, X. Zhang, *Adv. Sci.* **2020**, *7*, 1902359.
[20] J. D. Wood, S. A. Wells, D. Jariwala, K.-S. Chen, E. Cho, V. K. Sangwan, X. Liu, L. J. Lauhon, T. J. Marks, M. C. Hersam, *Nano Lett.* **2014**, *14*, 6964.
[21] Q. Zhou, Q. Chen, Y. Tong, J. Wang, *Angew. Chem., Int. Ed.* **2016**, *55*, 11437.
[22] N. Martín, N. Tagmatarchis, Q. H. Wang, X. Zhang, *Chem. - Eur. J.* **2020**, *26*, 6292.
[23] C. R. Ryder, J. D. Wood, S. A. Wells, Y. Yang, D. Jariwala, T. J. Marks, G. C. Schatz, M. C. Hersam, *Nat. Chem.* **2016**, *8*, 597.
[24] S. Thurakkal, X. Y. Zhang, *Mater. Chem. Front.* **2021**, *5*, 2824.
[25] A. Mitrovic, S. Wild, V. Lloret, M. Fickert, M. Assebban, B. G. Markus, F. Simon, F. Hauke, G. Abellan, A. Hirsch, *Chem.* **2021**, *27*, 3361.
[26] M. van Druenen, F. Davitt, T. Collins, C. Glynn, C. O'Dwyer, J. D. Holmes, G. Collins, *Chem. Mater.* **2018**, *30*, 4667.
[27] Z. Sofer, J. Luxa, D. Bousa, D. Sedmidubsky, P. Lazar, T. Hartman, H. Hardtdegen, M. Pumera, *Angew. Chem., Int. Ed.* **2017**, *56*, 9891.
[28] Y. Liu, P. Gao, T. Zhang, X. Zhu, M. Zhang, M. Chen, P. Du, G. W. Wang, H. Ji, J. Yang, S. Yang, *Angew. Chem., Int. Ed.* **2019**, *58*, 1479.
[29] X. Wang, R. K. M. Raghupathy, C. J. Querebillo, Z. Liao, D. Li, K. Lin, M. Hantusch, Z. Sofer, B. Li, E. Zschech, I. M. Weidinger, T. D. Kuhne, H. Mirhosseini, M. Yu, X. Feng, *Adv. Mater.* **2021**, *33*, 2008752.
[30] A. M. Kuchkaev, A. M. Kuchkaev, A. V. Sukhov, S. V. Saparina, O. I. Gnezdilov, A. E. Klimovitskii, S. A. Ziganshina, I. R. Nizameev, I. R. Vakhitov, A. B. Dobrynin, D. I. Stoikov, G. A. Evtugyn, O. G. Sinyashin, X. Kang, D. G. Yakhvarov, *Nanomaterials* **2023**, *13*, 826.
[31] R. Gusmão, Z. Sofer, M. Pumera, *ACS Nano* **2018**, *12*, 5666.
[32] D. Belotcerkovtceva, H. Nameirakpam, G. Datt, U. Noumbe, M. V. Kamalakar, *Nanoscale Horiz.* **2024**, *9*, 456.
[33] Z. Guo, S. Chen, Z. Wang, Z. Yang, F. Liu, Y. Xu, J. Wang, Y. Yi, H. Zhang, L. Liao, P. K. Chu, X.-F. Yu, *Adv. Mater.* **2017**, *29*, 1703811.
[34] Y. Zhao, Q. Zhou, Q. Li, X. Yao, J. Wang, *Adv. Mater.* **2017**, *29*, 1603990.
[35] T. Škorjanc, D. Shetty, M. A. Olson, A. Trabolsi, *ACS Appl. Mater. Interfaces.* **2019**, *11*, 6705.
[36] X.-H. Zhou, Y. Fan, W.-X. Li, X. Zhang, R.-R. Liang, F. Lin, T.-G. Zhan, J. Cui, L.-J. Liu, X. Zhao, K.-D. Zhang, *Chin. Chem. Lett.* **2020**, *31*, 1757.
[37] H. B. Ribeiro, C. E. P. Villegas, D. A. Bahamon, D. Muraca, A. H. Castro Neto, E. A. T. de Souza, A. R. Rocha, M. A. Pimenta, C. J. S. de Matos, *Nat. Commun.* **2016**, *7*, 12191.
[38] Y. Liu, J. Zou, S. Chen, B. Zhong, Y. Wang, H. Wang, X. Huang, *Spectrochim. Acta A Mol. Biomol. Spectrosc.* **2022**, *271*, 120861.
[39] H. Shi, S. Fu, Y. Liu, C. Neumann, M. Wang, H. Dong, P. Kot, M. Bonn, H. I. Wang, A. Turchanin, O. G. Schmidt, A. Shaygan Nia, S. Yang, X. Feng, *Adv. Mater.* **2021**, *33*, 2105694.
[40] Y. Huang, J. Qiao, K. He, S. Bliznakov, E. Sutter, X. Chen, D. Luo, F. Meng, D. Su, J. Decker, W. Ji, R. S. Ruoff, P. Sutter, *Chem. Mater.* **2016**, *28*, 8330.
[41] S. Yang, G. Chen, A. G. Ricciardulli, P. Zhang, Z. Zhang, H. Shi, J. Ma, J. Zhang, P. W. M. Blom, X. Feng, *Angew. Chem., Int. Ed.* **2020**, *59*, 465.
[42] M. Paul, *Phys. Scr.* **1992**, *46*, 295.
[43] Oxidation degree may vary when the ambient condition changes and further studies are underway.
[44] M. Pelavin, D. N. Hendrickson, J. M. Hollander, W. L. Jolly, *J. Phys. Chem.* **1970**, *74*, 1116.
[45] R. Franke, T. Chassé, P. Streubel, A. Meisel, *J. Electron Spectros. Relat. Phenomena* **1991**, *56*, 381.
[46] J. Pan, Y. Li, L. Zhuang, J. Lu, *Chem. Commun.* **2010**, *46*, 8597.
[47] S. Men, D. S. Mitchell, K. R. J. Lovelock, P. Licence, *ChemPhysChem* **2015**, *16*, 2211.
[48] G. Kresse, J. Furthmüller, *Phys. Rev. B* **1996**, *54*, 11169.
[49] G. Kresse, J. Furthmüller, *Comput. Mater. Sci.* **1996**, *6*, 15.
[50] J. P. Perdew, J. A. Chevary, S. H. Vosko, K. A. Jackson, M. R. Pederson, D. J. Singh, C. Fiolhais, *Phys. Rev. B* **1992**, *46*, 6671.
[51] J. P. Perdew, K. Burke, M. Ernzerhof, *Phys. Rev. Lett.* **1997**, *78*, 1396.
[52] P. E. Blöchl, *Phys. Rev. B* **1994**, *50*, 17953.
[53] G. Kresse, D. Joubert, *Phys. Rev. B* **1999**, *59*, 1758.
[54] S. Grimme, J. Antony, S. Ehrlich, H. Krieg, *J. Chem. Phys.* **2010**, *132*, 154104.

NANO · MICRO small

Supporting Information

for *Small*, DOI 10.1002/smll.202410300

Boosting 2D Black Phosphorus Ambient Stability: Noncovalent Functionalization Using Viologen Molecules

*Ishan Sarkar, Cong Guo, Cheng Peng, Yu Wang, Yafei Li and Xiaoyan Zhang**

WILEY-VCH

Supporting Information

Boosting 2D Black Phosphorus Ambient Stability: Noncovalent Functionalization using Viologen Molecules

*Ishan Sarkar[a], Cong Guo[b], Cheng Peng[a], Yu Wang[b], Yafei Li[b], Xiaoyan Zhang[a]**

I. Sarkar, C. Peng, Prof. X. Zhang

Department of Chemistry and Chemical Engineering

Chalmers University of Technology

Kemigården 4, SE-412 96 Göteborg, Sweden

E-mail: xiaoyan.zhang@chalmers.se

Dr. C. Guo, Prof. Y. Wang, Prof. Y. Li

Jiangsu Collaborative Innovation Centre of Biomedical Functional Materials, School of Chemistry and Materials Science, Nanjing Normal University, Nanjing, 210023 P. R. China

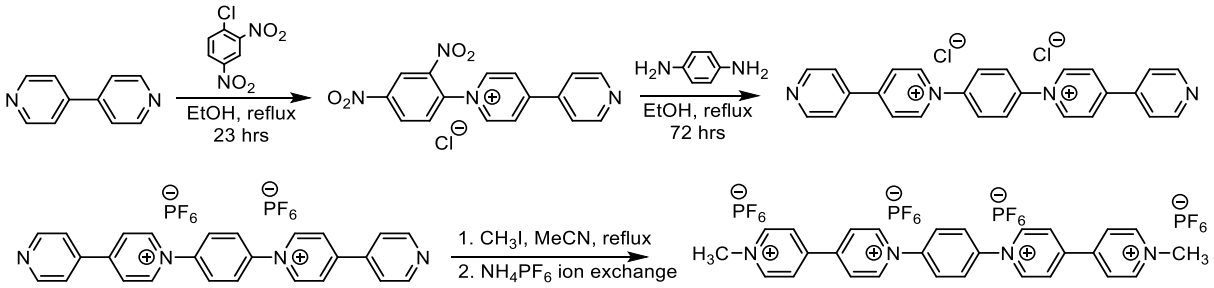

Scheme S1: Synthesis scheme for the MV_2-based viologen derivative.

Synthesis of 1-(2,4-dinitrophenyl)-[4,4'-bipyridin]-1-ium chloride (DNBP-Cl): 2,4-dinitrochlorobenzene (1 g, 4.9 mmol) and 4,4'-bipyridine (848.2 mg, 5.4 mmol) were dissolved in ethanol (25 mL). The mixture was heated under reflux for 24 h. The hot mixture was filtered, and the filtered cake was washed by acetone (2 × 80 mL). The solvent was evaporated and the remaining solid was recrystallized from C_2H_5OH/ether. The compound was obtained as a brown solid (0.45 g, 26%). Yield: 25.3% (448 mg), ^{1}H NMR (600 MHz, D_2O, δ): 9.40 (d, 1H), 9.26 (d, 2H), 8.95 (dd, 1H), 8.86 (d, 2H), 8.70 (d, 2H), 8.29 (d, 1H), 8.06 (d, 2H).

Synthesis of 1,1''-(1,4-phenylene)bis(([4,4'-bipyridin]-1-ium)) hexafluorophosphate ($MV_2(PF_6)_2$): 1-(2,4-dinitrophenyl)-[4,4'-bipyridin]-1-ium chloride (447.6 mg, 1.249 mmol) and *p*-phenylenediamine (64.23 mg, 0.594 mmol) were dissolved in ethanol (15 mL). The mixture was heated under reflux for 72 h. The solvent was evaporated and the remaining solid was washed by acetone (200 mL). The filter cake was collected and was dissolved in water and its hexafluorophosphate salt mixture was obtained by ion-exchange with NH_4PF_6 (excess). The pure compound was obtained as brown solid by recrystallization in MeCN/diethylether (1:3). Yield: 23.6% (91 mg), ^{1}H NMR (600 MHz, CD_3CN, δ): 9.11 (d, 4H), 8.93 (d, 4H), 8.58 (d, 4H), 8.12 (s, 4H), 7.93 (d, 4H).

Synthesis of 1',1'''-(1,4-phenylene)bis(1-methyl-[4,4'-bipyridine]-1,1'-diium) hexafluorophosphate ($MV_2(PF_6)_4$): In a sealed tube, 1,1''-(1,4-phenylene)bis(([4,4'-bipyridin]-

1-ium)) hexafluorophosphate (91 mg, 0.14 mmol) was dissolved in acetonitrile (5 ml) and to it methyl iodide (1 ml) was added. The mixture was heated to 80 °C and kept running overnight. The reaction was stopped afterwards, and the solvent was evaporated. The solid obtained was dissolved into water and its hexafluorophosphate salt was obtained by ion-exchange with NH_4PF_6 (excess). Yield: 62.2% (87 mg), ^{1}H NMR (600 MHz, CD_3CN, δ): 9.25 (d, 4H), 8.92 (d, 4H), 8.66 (d, 4H), 8.50 (d, 4H), 8.17 (s, 4H), 4.45 (s, 6H).

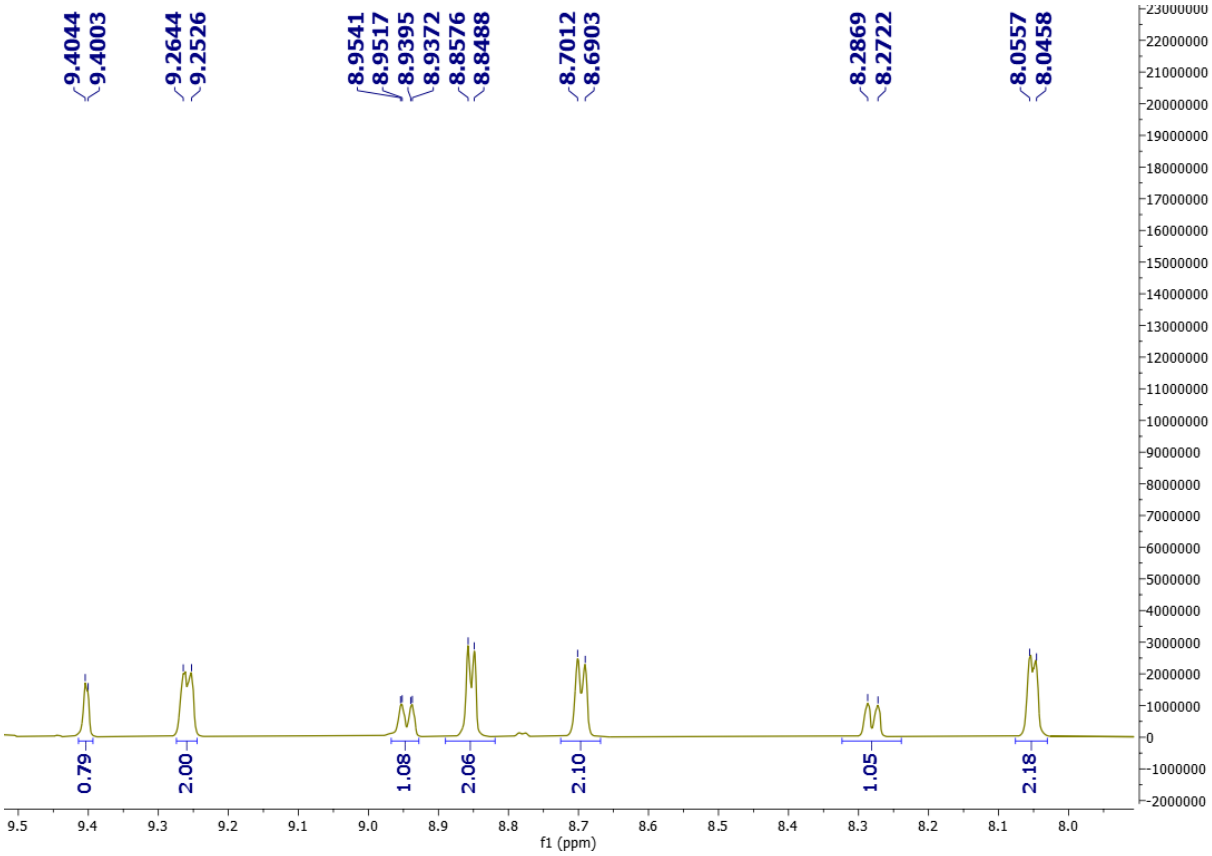

Figure S1. ^{1}H NMR spectrum of DNBP-Cl (D_2O, 600 MHz).

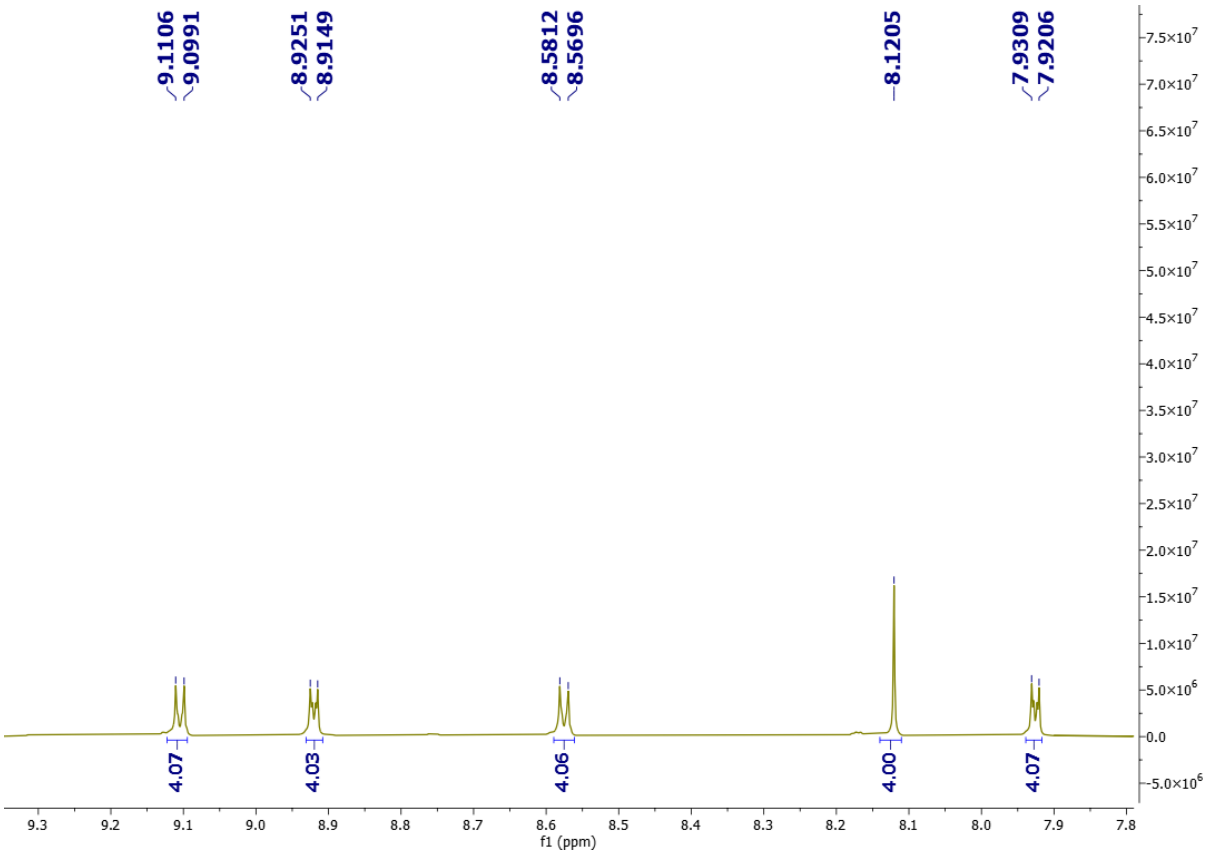

Figure S2. ^{1}H NMR spectrum of $MV_2(PF_6)_2$ (CD_3CN, 600 MHz).

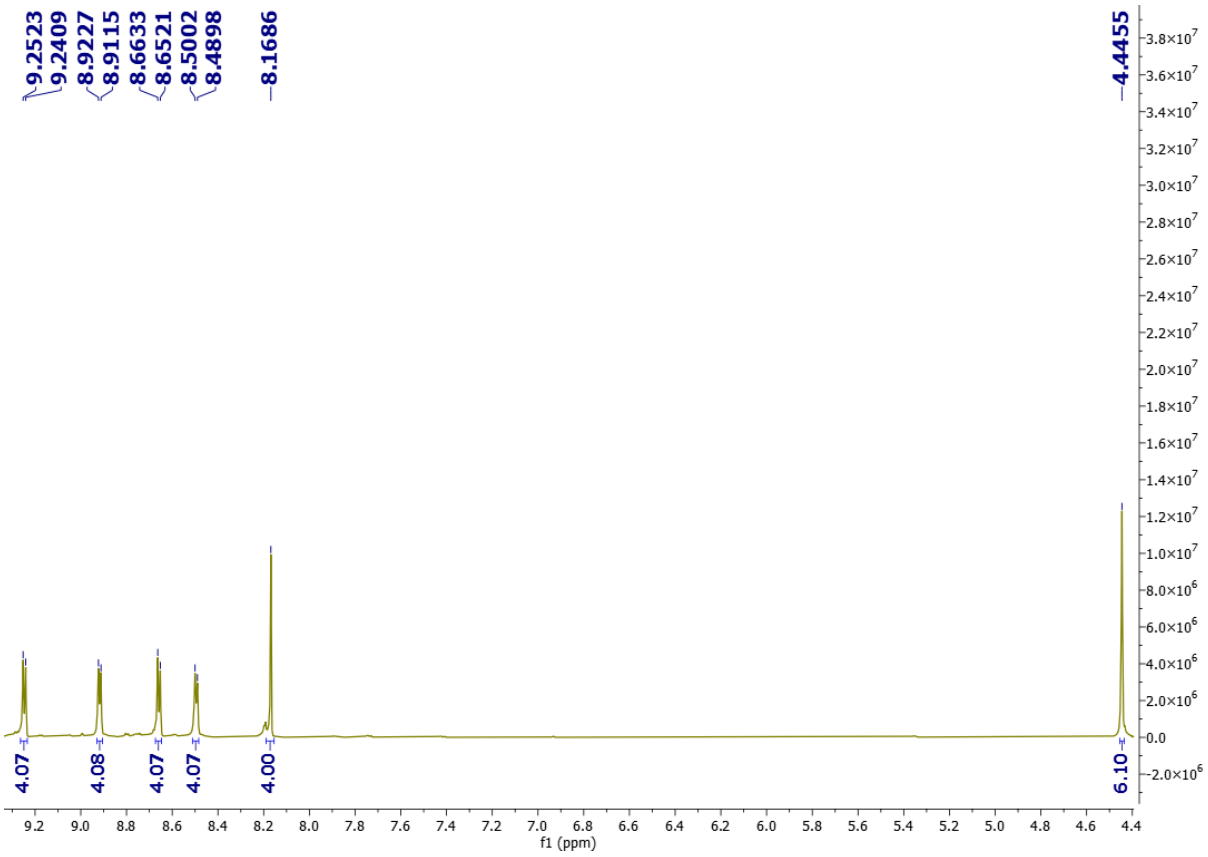

Figure S3. ^{1}H NMR spectrum of $MV_2(PF_6)_4$ (CD_3CN, 600 MHz).

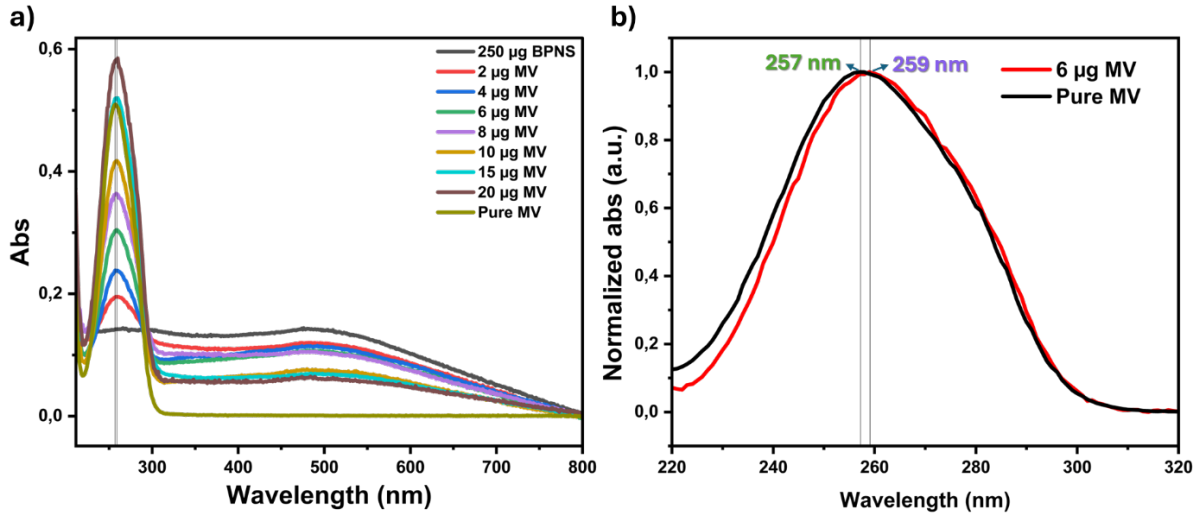

Figure S4. UV-vis absorption based titrimetric study between $MV(PF_6)_2$ and BPNSs, showing (a) full spectra of the hybrids compared to the pure molecular absorption (with zeroing) and (b) normalized absorption spectra showing the shift in peak absorbance.

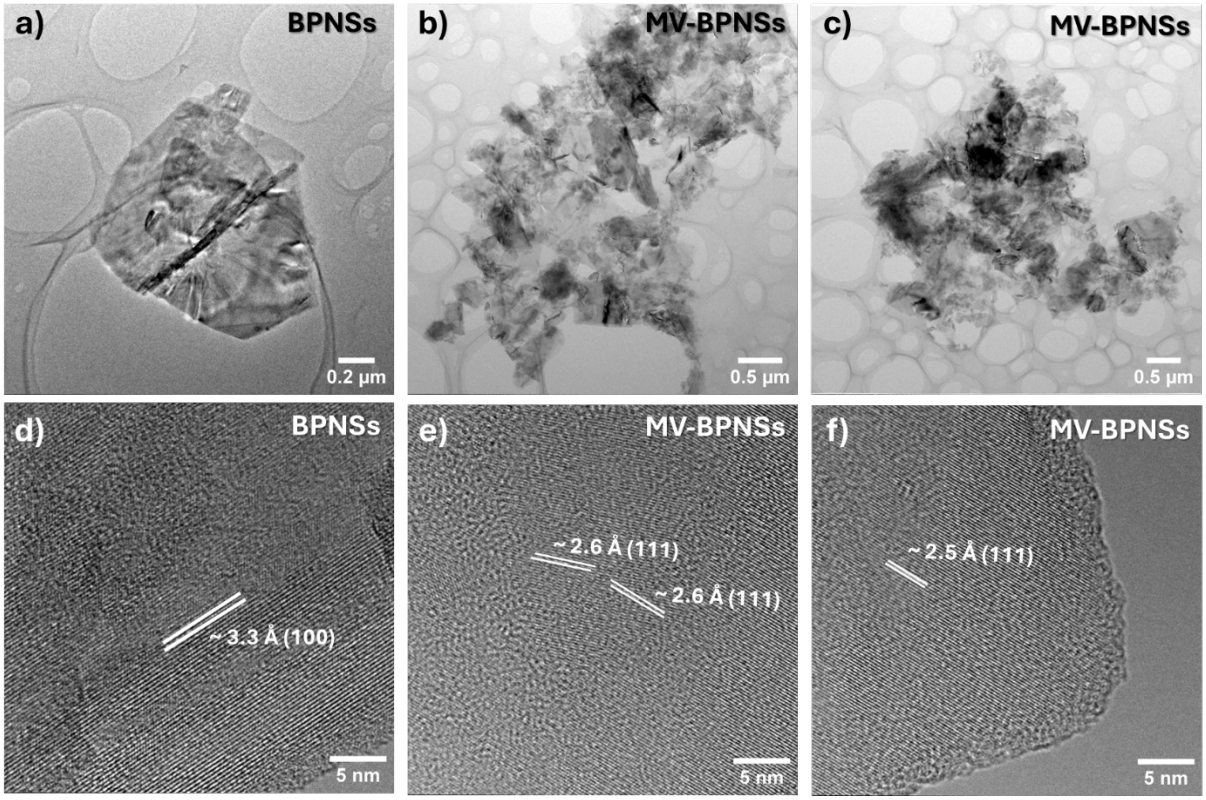

Figure S5. Additional TEM images of (a) BPNSs, (b,c) the MV-BPNS hybrids and HR-TEM images of (d) BPNSs showing the (100) plane with a d-spacing of approximately 3.3 Å and (e,f) the MV-BPNS hybrids showing the (111) planes with a d-spacing of approximately 2.6 Å.

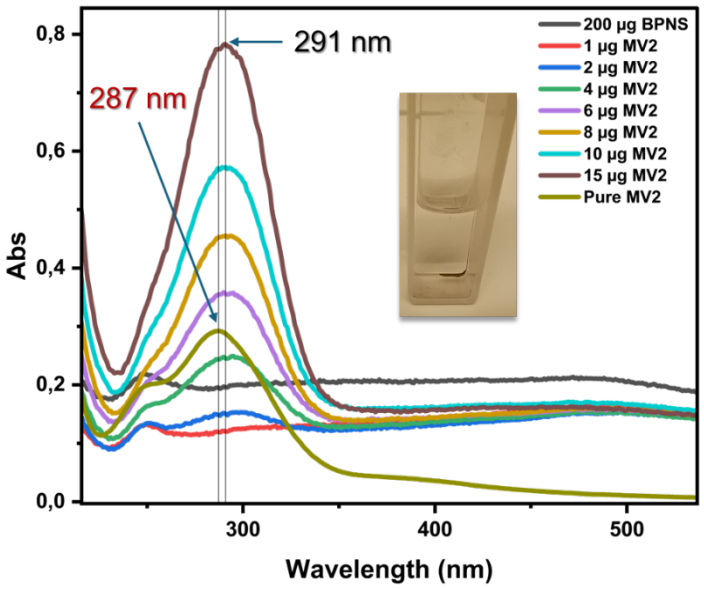

Figure S6. UV-vis absorption based titrimetric study between $MV_2(PF_6)_4$ and BPNSs, indicating the interaction between MV_2 and BPNSs at a low concentration level. The absorbance of $MV_2(PF_6)_4$ in acetonitrile (1.55 ml, 0.0045 mg ml^{-1}) was measured for comparison.

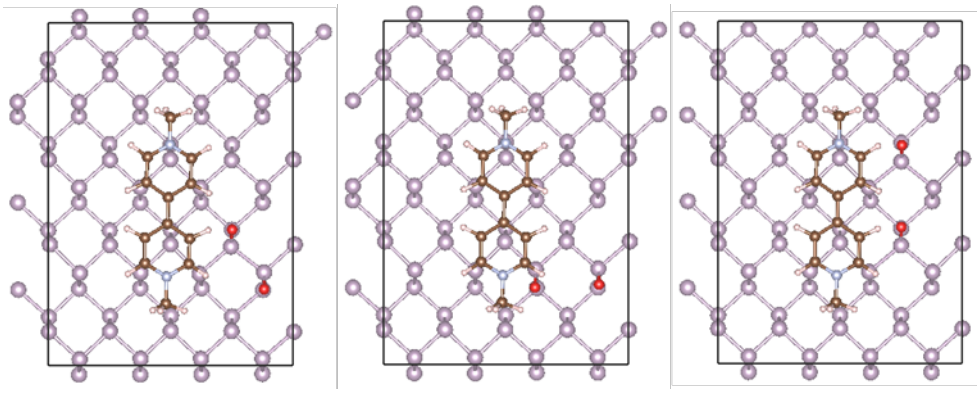

Figure S7. Structures of O_2 after adsorption at different sites on MV-BPNS.

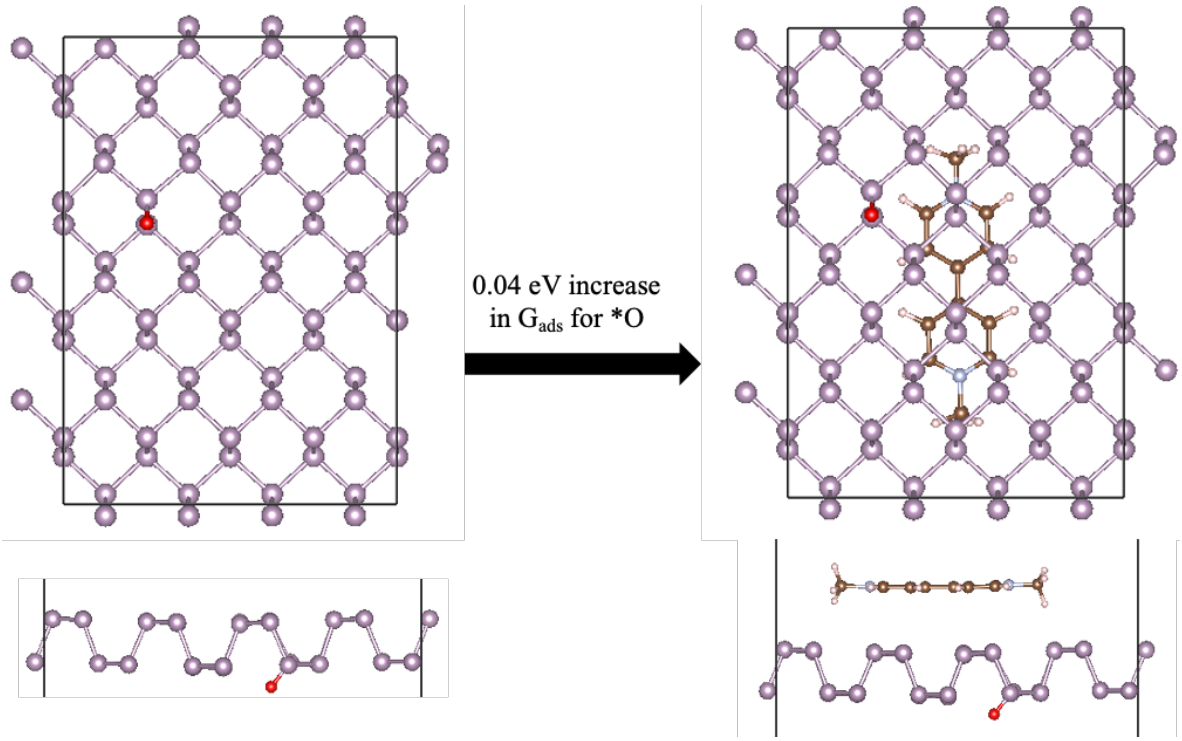

Figure S8. The calculated adsorption free energy increased by 0.04 eV for the MV-BPNS hybrid, compared to the pure BPNS.

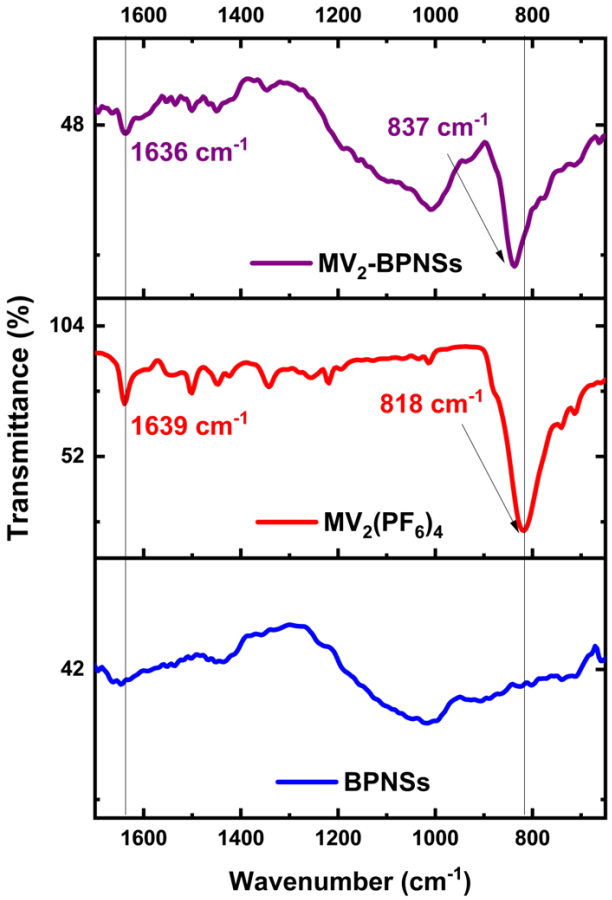

Figure S9. ATR-IR spectra of BPNSs, $MV_2(PF_6)_4$ and the MV_2-BPNS hybrid.

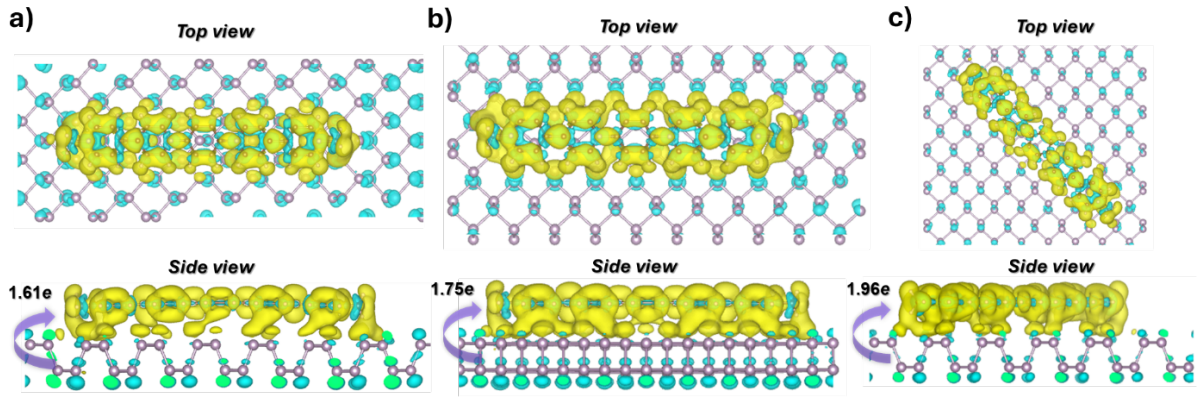

Figure S10. Charge difference plots of the MV_2 molecules on top of a single-layer BPNS surface: (a) perpendicular to the ridge, (b) parallel to the ridge, (c) diagonal to the ridge. Orbital overlap scenarios for the MV_2-BPNS hybrids in each direction are shown as the side view located under each consecutive illustration. The yellow region represents areas of electron accumulation, while the cyan region indicates areas of electron depletion.

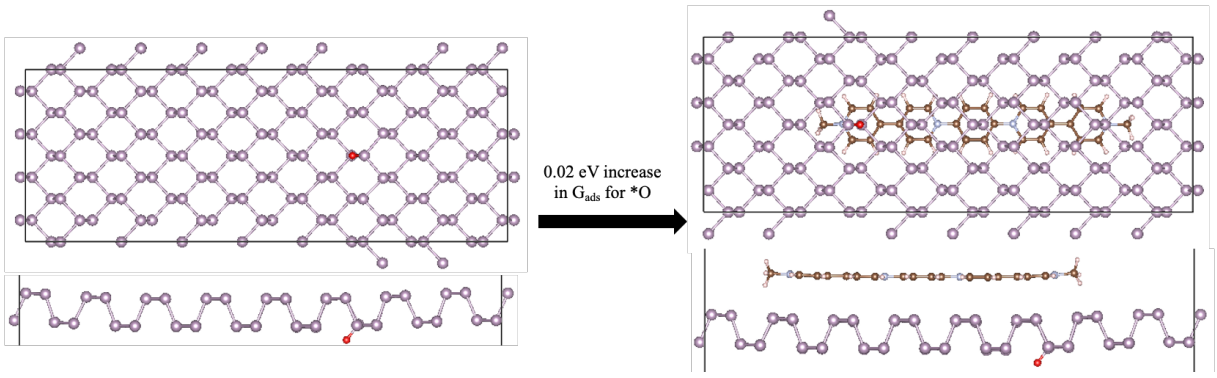

Figure S11. The calculated adsorption free energy increased by 0.02 eV for the MV_2-BPNS hybrid, compared to the pure BPNS.

Table S1. Total and average adsorption energy of the MV_2-BPNSs hybrids along different directions from the ridges of BPNSs calculated by DFT.

Materials [MV_2-BPNSs]	**E_{ads} (eV)**	**Number of atoms (X)**	**E_{ads}/X (eV)**
Perpendicular	−2.74	58	−0.0472
Parallel	−2.83	58	−0.0487
Diagonal	−2.67	58	−0.0460

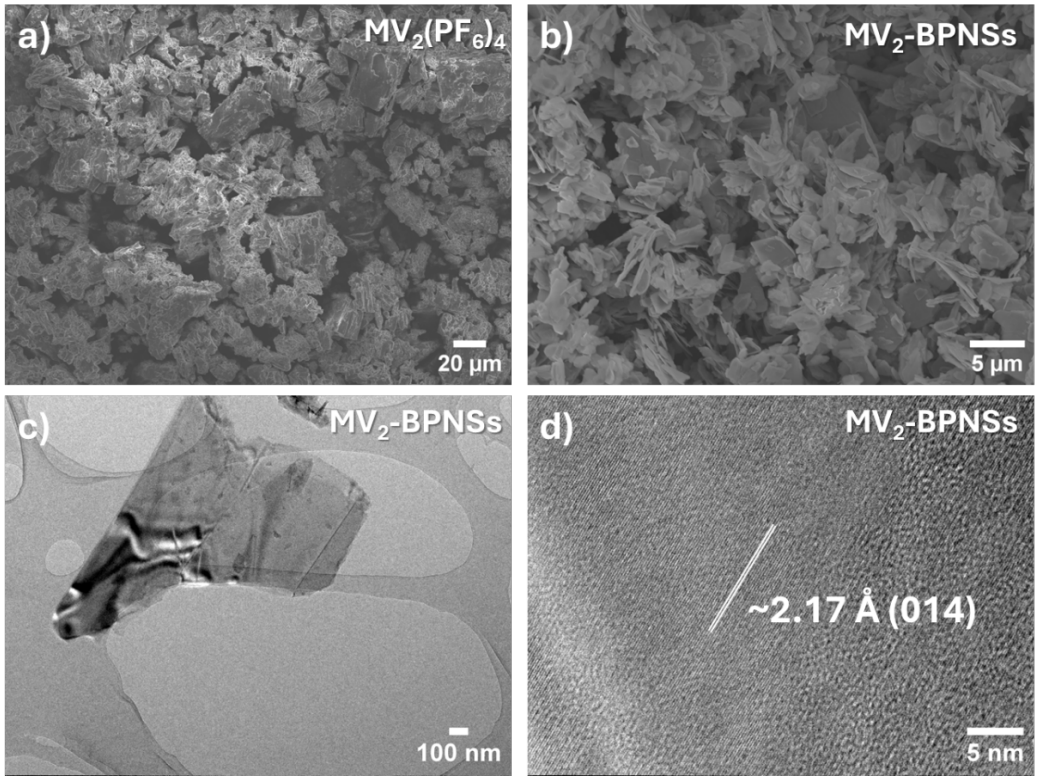

Figure S12. Electron microscopy images of the MV_2-BPNS hybrids (a) SEM image of $MV_2(PF_6)_4$, (b) SEM image of the $MV_2(PF_6)_4$-BPNS hybrid (zoomed in), (c) TEM image of the $MV_2(PF_6)_4$-BPNS hybrid and (d) HR-TEM image of the $MV_2(PF_6)_4$-BPNS hybrid. The MV_2-BPNS hybrid did not show an aggregated morphology as the MV_2 molecules might pass through the TEM grid due to the lower adsorption energy of the molecule and slower aggregation kinetics.

Table S2. P2p binding energies of the MV_2-BPNS hybrid in XPS measurements.

Binding Energy	**MV_2-BPNS-P1 (eV)**	**MV2-BPNS-P2 (eV)**	**MV_2-BPNS-A1 (eV)**	**MV_2-BPNS-A2 (eV)**
$P2p_{3/2}$	129.63	129.04	129.84	129.74
$P2p_{1/2}$	130.47	129.88	130.68	130.58
P−O	133.38	133.31	133.38	133.33
P=O	134.28	134.28	134.28	134.23
P-F	136.57	136.18	136.73	136.92

P-protected, A-ambient

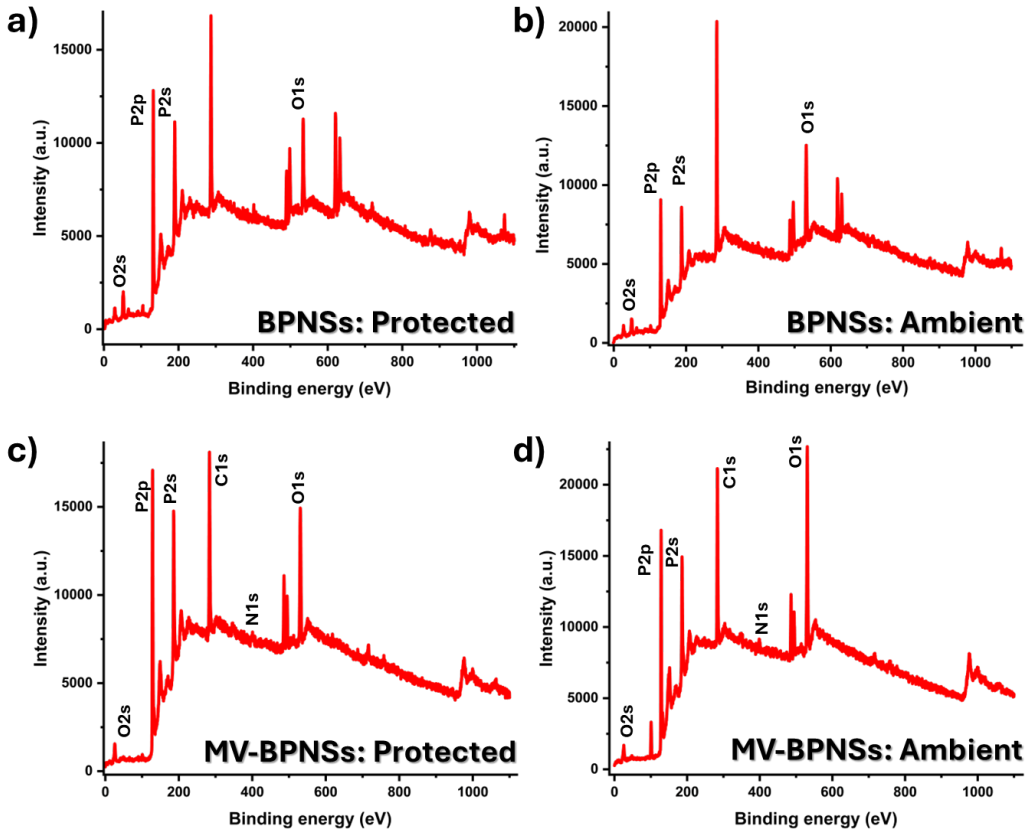

Figure S13. XPS: Survey spectra of (a) BPNSs in protected conditions (b) BPNSs in ambient conditions, (c) MV-BPNSs in protected conditions and (d) MV-BPNSs in ambient conditions.

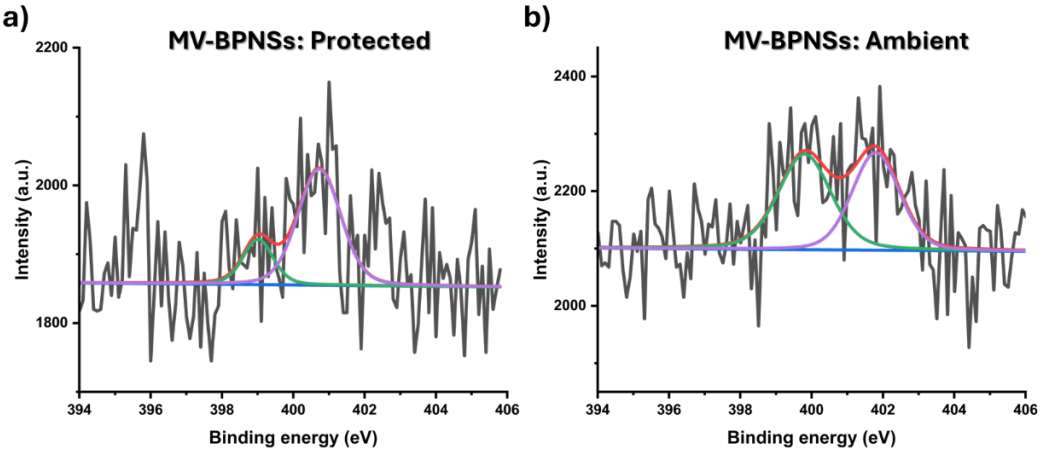

Figure S14. N1s XPS spectra of MV-BPNSs in (a) protected and (b) ambient conditions. The charged nitrogen (N^+) and radical cation ($N^{\cdot+}$) generated during X-ray exposure in the XPS chamber can be assigned to 400.7 eV and 399 eV for the protected hybrid and 401.8 eV and 399.8 eV for the hybrid in ambient condition.[S1] The sample preparation was performed in acetonitrile and the acetonitrile signal was not observed at 397.7 eV.[S2]

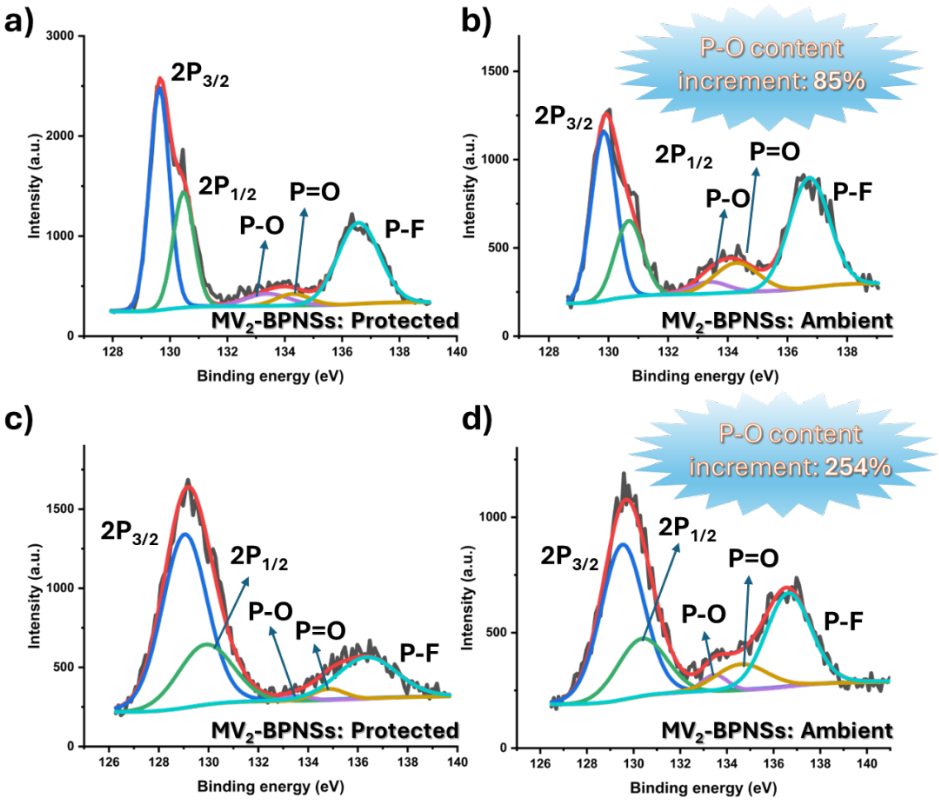

Figure S15. P2p XPS spectra of the MV_2-BPNS hybrid under (a,c) protected and (b,d) ambient conditions. The increase in the P-O/P=O content was compared under similar experimental conditions.

[S1]. Z. Wei, W. Shin, H. Jiang, X. Wu, W. F. Stickle, G. Chen, J. Lu, P. Alex Greaney, F. Du, X. Ji, *Nat. Commun.* **2019,** *10*, 3227.
[S2]. B. A. Sexton, N. R. Sexton, *Surf. Sci.* **1983,** *129*, 21-36.

Paper II

Charged Viologen Polymers with Hydrophobic Backbones Enable Improved Ambient Stability of 2D Black Phosphorus

*Ishan Sarkar[a], Xiaoyan Zhang[a]**

I. Sarkar, Prof. X. Zhang

Department of Chemistry and Chemical Engineering

Chalmers University of Technology

Kemigården 4, SE-412 96 Göteborg, Sweden
E-mail: xiaoyan.zhang@chalmers.se

Abstract

Black phosphorus nanosheets (BPNSs) exhibits unique layer-dependent electronic and optical properties, making it a promising candidate for next-generation nanoelectronics and optoelectronic devices. However, BP suffers from rapid degradation under ambient conditions due to photo-oxidation and moisture sensitivity. This instability severely limits its practical applications and long-term device performance. Strategies such as surface passiveness and encapsulation are therefore critical to enhancing BP's environmental stability. Herein, viologen-based polymer with a polystyrene-backbone was synthesized and employed as hydrophobic moieties to encapsulate the nanosheets. The non-covalent interaction was characterized and the resulting hybrid showed prolonged ambient stability for 6 days period. This paves the way for a new and promising approach towards ambient decomposition resistance for BPNSs.

Introduction

Black phosphorus nanosheets (BPNSs), a two-dimensional layered semiconductor with a thickness-dependent direct bandgap ranging from ~0.3 eV in bulk to ~2.0 eV in the monolayer regime, has attracted considerable attention for its potential in nanoelectronics and optoelectronic applications.[1-5] However, its intrinsic instability under ambient conditions presents a major obstacle to practical integration.[6, 7] Exposure to air initiates a photoinduced oxidation process, whereby absorbed oxygen and water molecules react with phosphorus atoms which leads to the formation of phosphorus oxides which undergo further hydrolysis and degradation of the BP lattice.[6-9] The photodegradation is thermodynamically favorable and often causes substantial deterioration of its

structural and electronic properties, resulting in progressive loss of device performance.

Several strategies have been investigated to address the ambient instability of BPNSs, with protective methods generally categorized into covalent and non-covalent approaches. Covalent strategies involve modifying the BPNS surface by forming chemical bonds with various functional groups, such as alkyl or aryl groups, often achieved through reactions like diazonium/azide coupling, free radical reactions and nucleophilic substitution reactions.[10-14] These modifications can effectively reduce exposure to reactive agents and enhance resistance to oxidation. However, they can also alter the material's electronic structure, potentially introduce defects or disrupt charge transport characteristics. Non-covalent methods, in contrast, rely on weaker interactions—such as van der Waals forces or π-π stacking interactions—to provide protective coatings that preserve BP's crystal integrity. Common techniques in this category include encapsulation with inert materials like hexagonal boron nitride (h-BN), graphene, or aluminum oxide (AlO_x), as well as the adsorption of stabilizing organic molecules or polymers.[15]

The degradation pathway of BPNSs has previously been investigated by many, both experimentally and theoretically. Hersam et al has conducted detailed studies on the formation of phosphoric acid onto the nanosheets upon ambient exposure with the help of atomic force microscopy.[15] Theoretical studies showed that the degradation pathway is initiated by the formation of peroxides in the presence of oxygen and is photocatalyzed. The intermediate oxide/peroxide species are polar and undergoes further degradation facilitated by water.

Although lower than graphene, BPNSs, being made up of phosphorus atoms, are inherently hydrophobic in nature. Hydrophobic interactions, often misinterpreted as van der Waals forces, arise not from direct attractions between hydrophobic species but from the entropic cost of disrupting the hydrogen-bonded water network, which drives water to exclude nonpolar groups.[16] Long term stability has been achieved for BPNSs by using fluorinated surfactants which in turn gives near-superhydrophobic properties for the hybrids.[17] Our previous work[18] on the ambient stability issue of BPNSs revealed excellent protection of the nanosheets by dimethyl viologen molecules by means of cation-induced dipole interaction. Herein, we explored the effect of multiple Van der Waals' interaction with BPNSs by introducing hydrophobic polymeric backbone of polystyrene coupled with the diffused cationic π-system of the viologen moieties and examined the ambient protection efficiency of the polymeric structure.

Results and discussions

The polymeric viologen derivative was designed to include hydrophobic interaction alongside charge-induced dipole interactions. The synthesis starts from mono-methylation of 4,4'-bipyridine followed by S_N2 substitution of 4-vinylbenzyl chloride and radical polymerization by $K_2S_2O_8$ to yield the polymer.

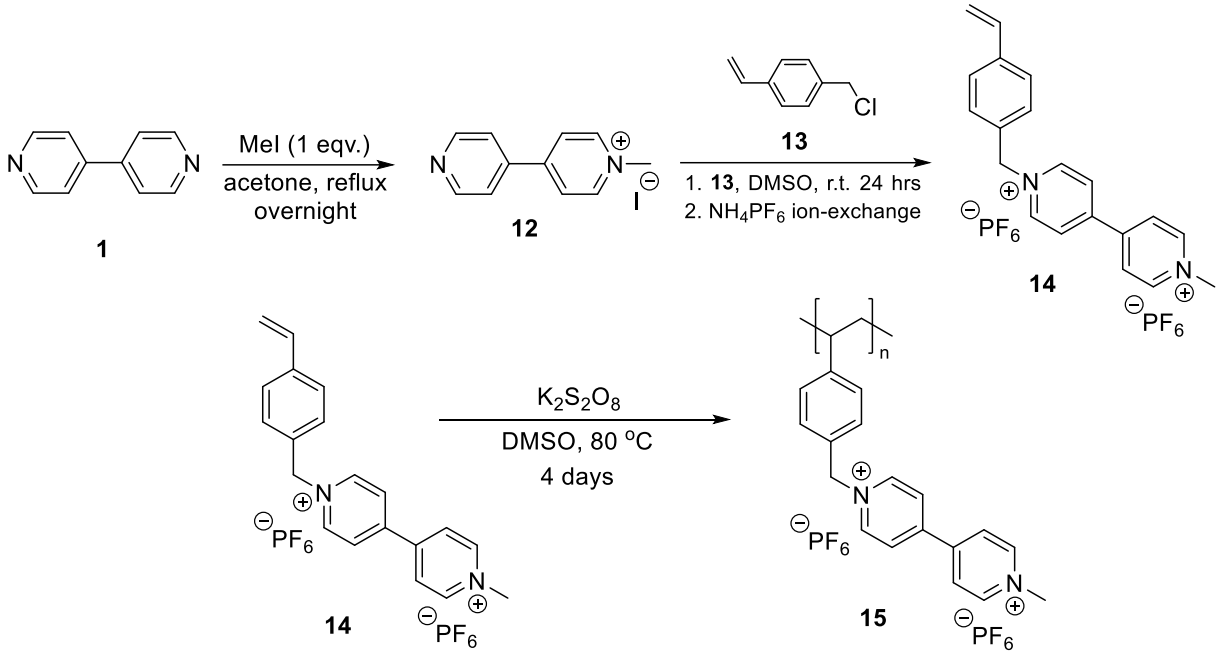

Scheme 1. *Synthetic scheme for viologen-based polymer **15** with alkyl chain as a backbone. (For the conversion of **1** to **12**, more than 1 equivalent of methyl iodide has been used, however, due to the very low solubility of **12** in acetone, the mono-substituted product precipitates and the reaction is terminated before further substitution).*

In earlier studies, viologen moieties have been found to interact with BPNS surfaces through charge induced dipole interactions, however, the interaction was found to be much weaker in the case of viologen-based extended π-network where free rotation of aromatic rings is allowed. Compound 15, hence, was measured for the peak absorbance, which was found to be around 273 nm (Figure X) in acetonitrile medium, and the offset for the absorbance was observed to start from a relatively lower wavelength, attributed to the scattering by the polymeric backbone in acetonitrile due to its poor dispersibility in the solvent system.

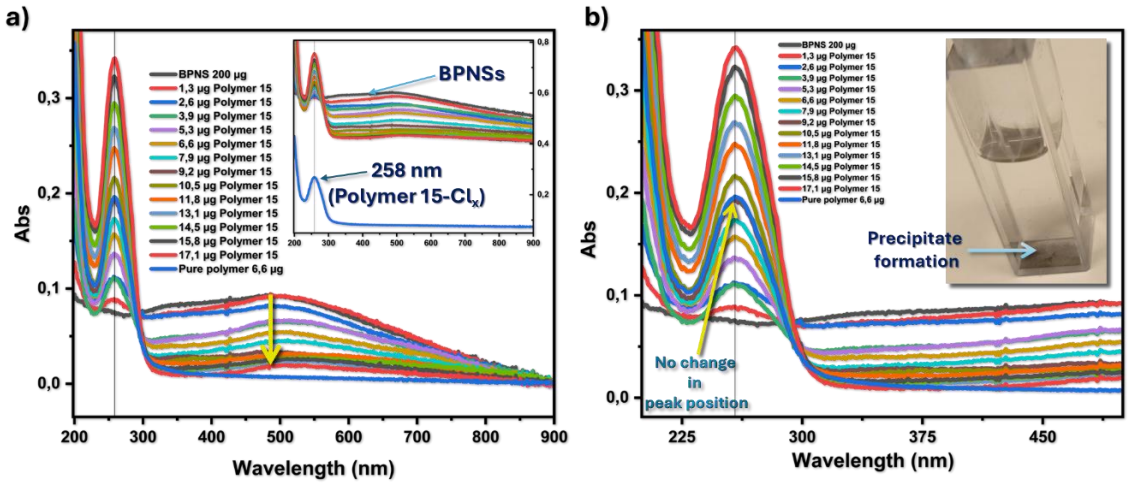

Figure X1. *Titrimetric studies indicate the interaction between the polymer* ***15-Cl$_x$*** *and BPNSs (200 µg, 2 ml) in water, as observed through UV-vis absorption measurements, (a) lowering of scattering with the addition of* ***15-Cl$_x$*** *to the BPNS dispersion after zeroing (inset: original spectra without zeroing), (b) clear view of peak absorbances of the* ***15****-BPNS hybrids with no shift in peak positions as compared against the pure* ***15-Cl$_x$*** *(inset: precipitation was observed at the bottom of the cuvette).*

To further investigate the nature of the interaction, the polymer was synthesized from the chloride derivative of the monomer and was titrated against the BPNS dispersion in water medium. The dispersibility of the polymer was found to be excellent in water and the absorbance peak was found to be at 258 nm (Figure X1). However, the addition of the polymer to a BPNS dispersion showed a 2 nm red shift along with worsened dispersibility. This is suspected to originate from the formation of aggregates in the aqueous medium.

The aggregate formation was further characterized by zeta potential studies. The polymer is positively charged with negatively charged chlorides as counter anions. Since small molecules and ions don't show zeta potential, the positive value of +30.9 mV can only be attributed to the positively charged polymer. Pure BPNS dispersions on the other hand show a zeta potential of –13.9 mV. The mass fraction of the nanosheets and the polymer was varied, and the zeta potential was measured for the composites. With the increment of mass fraction for the polymer, the mean zeta potential of the pure nanosheets was observed to be shifted towards more positive value (normalized intensity distribution provided in fig X2) and the charge neutralization point was observed at a mass fraction of 0.04. The mean zeta potential was further observed to increase with increment in mass fraction and finally converge towards the zeta potential value of the pure polymer.

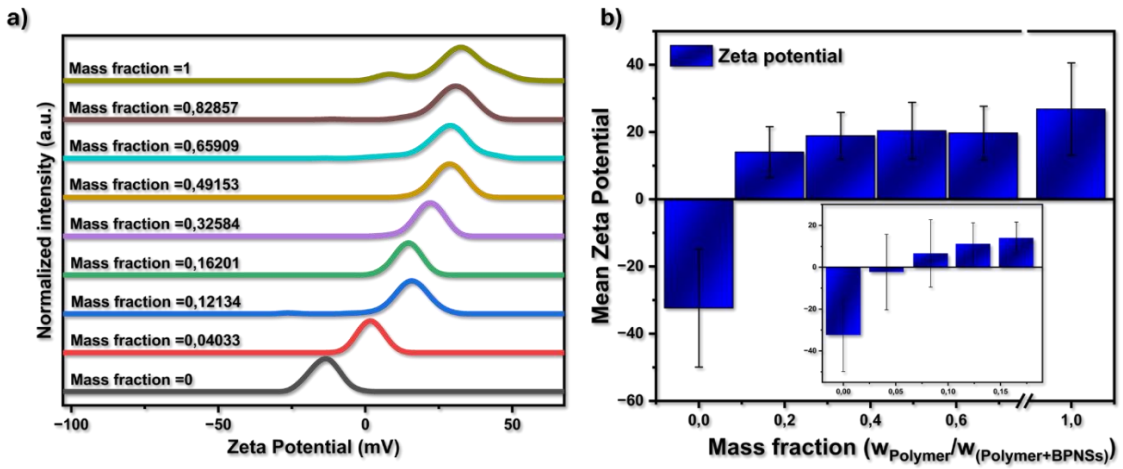

Figure X2. *Zeta potential studies for the* ***15****-BPNS hybrid systems, (a) changes in zeta potential plotted against the normalized intensity with the increment in polymeric mass fractions, (b) mean zeta potential increment with the increase in polymeric mass fractions (neutralization-point was achieved between the polymeric mass fraction of 0.04 and 0.08 (inset)).*

ATR-FTIR was performed on the hybrids to observe the interaction between the polymer and BPNSs. The aliphatic bending modes and the stretching modes of the polymer can be traced to the hybrid samples at 1639 (C=C stretch), 1560-1506 (C-C in ring stretch, aromatic), 1456 (C-H bend, alkane) and 1342 (C-N stretch, aromatic) cm^{-1} (Figure X). The clear distinction of the aliphatic C−H out-of-plane bending modes (750-850 cm^{-1}) of the polymer cannot be observed in the hybrid, instead of which a new cluster of peaks can be seen around 1118 cm^{-1} because of the aggregation of the polymer around the nanosheets which could be assigned to the available bending modes in the new hybrid system (Figure X3).

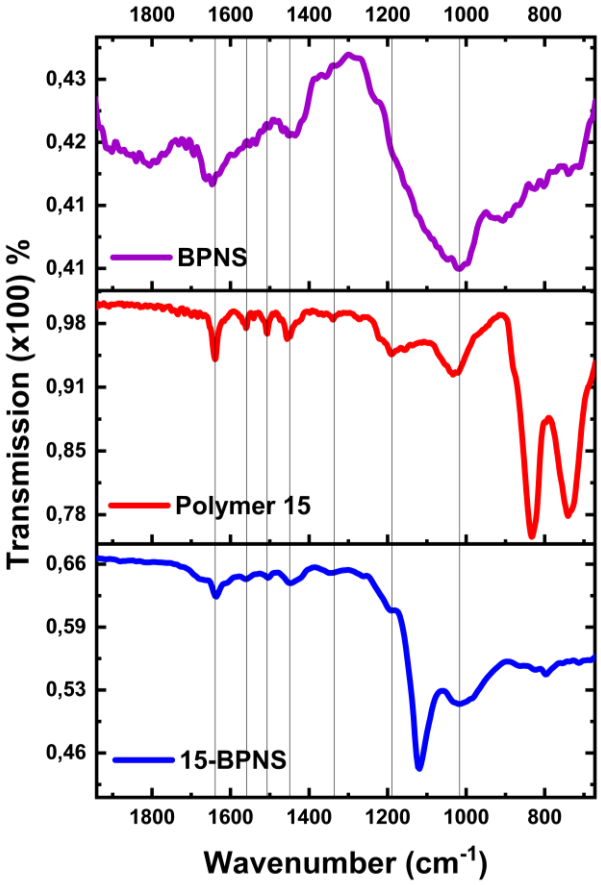

Figure X3. *ATR-FTIR spectra of BPNSs, polymer-15, and the 15-BPNS hybrid.*

The morphology of the hybrids was characterized by scanning electron microscopy imaging. The hybrid samples were prepared by grinding the BPNSs and the polymers in dry DMSO under constant nitrogen flow to avoid inhomogeneity in the samples. The dry samples for the SEM studies were obtained by evaporating the DMSO under high vacuum. The morphology of the hybrid samples was seen to contain non-flake like features onto the nanosheet surfaces which were observed to be completely absent in the bare nanosheet surfaces (Figure X4). This in turn indicates the formation of hybrid materials with the nanosheets having flake-like features retained.

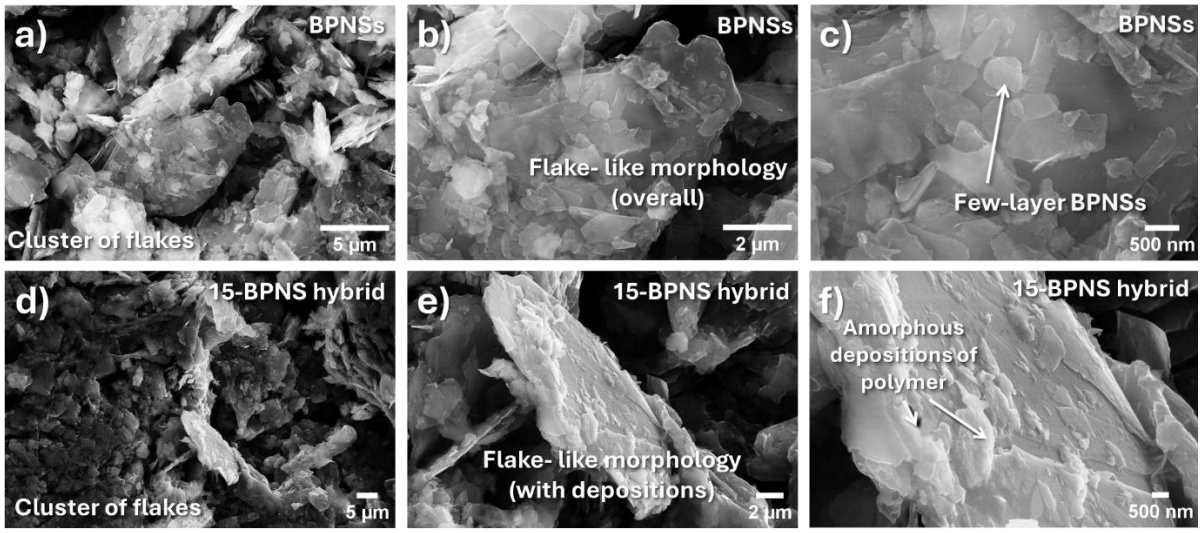

Figure X4. *SEM images of (a-c) BPNSs and (d-f) the **15**-BPNS hybrid. Flake-like morphology is present in both cases; in contrast, amorphous polymeric depositions can be observed for the **15**-BPNS hybrid (e,f).*

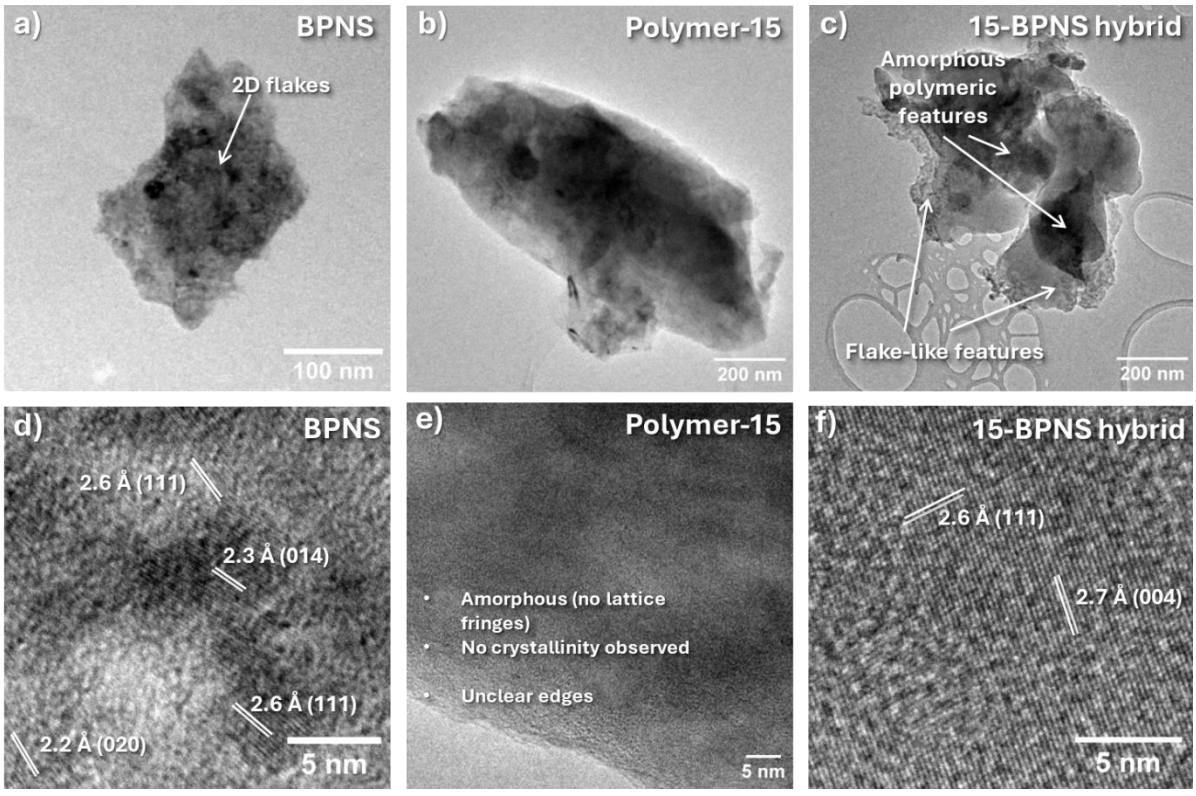

Figure X5. *TEM (a-c) and HR-TEM (d-f) images of (a,d) BPNSs, (b,e) polymer-**15** and (c,f) **15**-BPNS hybrids. The lattice fringes have been assigned by generating powder XRD patterns in VESTA using the crystallographic data provided by Hultgren et al.[19]*

Ambient stability efficiency was investigated using XPS studies and the $P2p_{3/2}$, $P2p_{1/2}$, P-O and P=O peaks can be observed at 129.79, 130.63, 133.51, 134.03 eV for the bare BPNSs (Figure X3, table X) and at 129.29, 130.13, 132.98, 134.26 eV for the 15-BPNS hybrid (Figure X3, table X) preserved in the protected

conditions. The $P2p_{3/2}$, $P2p_{1/2}$, P-O and P=O peaks can be observed at 129.82, 130.66, 133.43, 134.44 eV for the bare BPNSs (Figure X3, Table X) and at 129.50, 130.34, 133.38, 134.26 eV for the 15-BPNS hybrid (Figure X3, Table X) stored in ambient conditions.

Table X. P2p binding energies of BPNSs and 15-BPNS in XPS measurements.

Binding Energy	BPNS-P* (eV)	BPNS-A* (eV)	15-BPNS-P (eV)	15-BPNS-A (eV)
$P2p_{3/2}$	129.79	129.29	129.82	129.50
$P2p_{1/2}$	130.63	130.13	130.66	130.34
P–O	133.51	132.98	133.43	133.38
P=O	134.03	134.26	134.44	134.26

**P-protected, A-ambient*

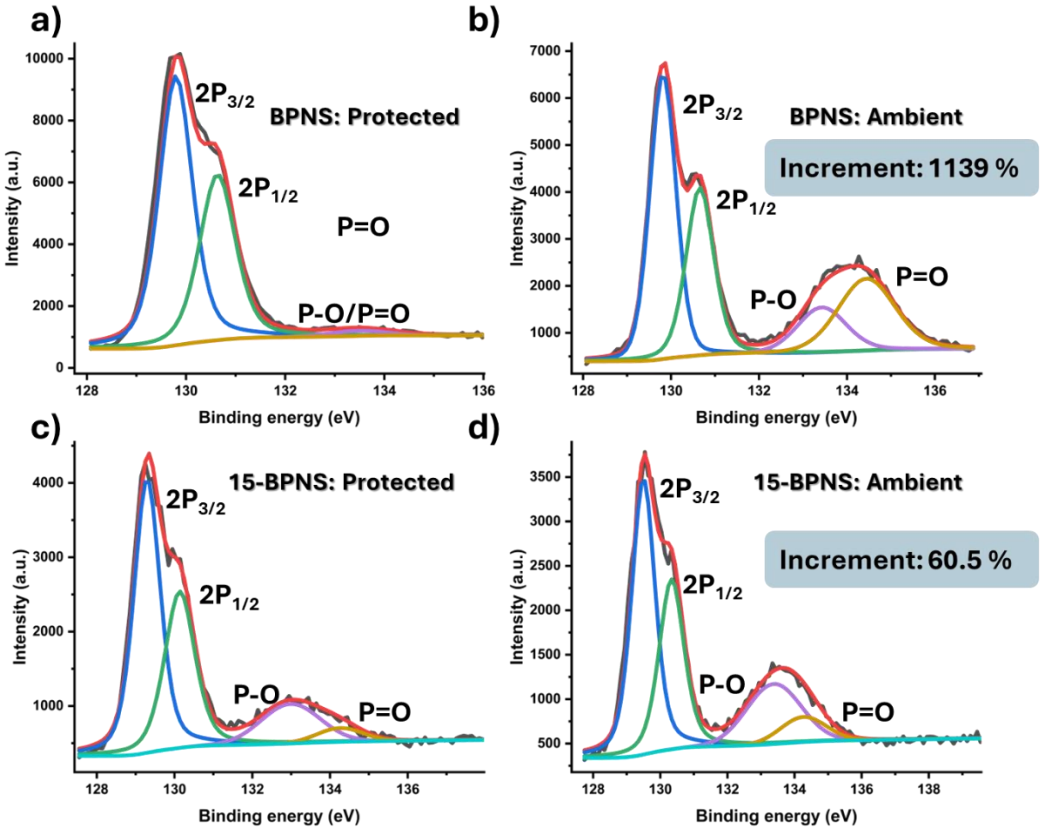

Figure X6. *P2p XPS spectra of (a,b) BPNS under protected and ambient conditions. (c,d) The 15-BPNS hybrid under protected and ambient conditions.*

The extent of oxidation was determined by comparing the P-O/P=O content for both the samples after 6 days of exposure. The pure BPNSs sample had an overall

increment of 1139 % in the P-O/P=O content, whereas the polymer- hybrid showed only 60.5 % of increment within the same exposure time. More experiments will be conducted to further validate the results.

*Synthesis of compound **12**:* In a sealed tube, 4,4'-bipyridine (500 mg, 3.2 mmol, 1 eqv.) was dissolved in acetone (15 ml). To it, methyl iodide (0.4 ml, 6.43 mmol, 2 eqv.) was added. The mixture was stirred at room temperature for 24 hours. The precipitate was filtered, washed with acetone, and the filter cake was collected by redissolving it in methanol. Yield: 89.4% (853.11 mg), ^{1}H NMR (600 MHz, CD_3OD, δ): 9.04 (d, 2H), 8.84 (d, 2H), 8.51 (d, 2H), 7.99 (d, 2H), 4.47 (s, 3H).

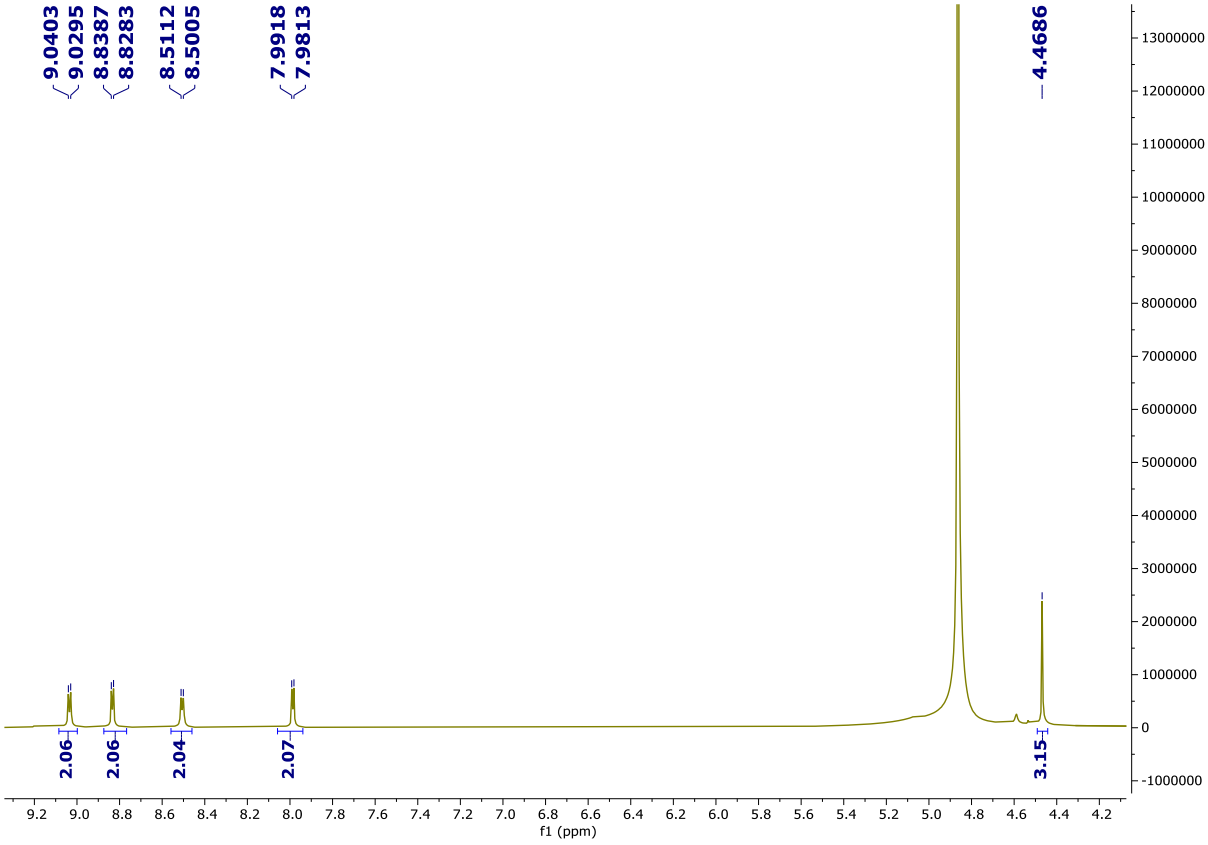

Figure S1. *^{1}H NMR spectrum of compound **12** (CD_3OD, 600 MHz).*

*Synthesis of compound **14**:* In a capped vial, *N*-methyl-4,4'-bipyridinium iodide (500 mg, 1.68 mmol) was dissolved in DMSO (3 ml). To it, 4-vinylbenzylchloride (0.29 ml, apprx. 308 mg, 1.2 eqv) was added. The mixture was stirred at room temperature for 24 hours. To the mixture, acetonitrile (20 ml) was added. The orange solid was precipitated and collected by filtration. The filter cake was washed with acetonitrile and recollected using methanol. Yield: 50.9% (386.46 mg). The hexafluorophosphate salt derivative was obtained by ion-exchange with

NH_4PF_6 (excess). The pure compound was obtained as white solid, ^{1}H NMR (600 MHz, CD_3OD, δ): 9.34 (d, 2H), 9.19 (d, 2H), 8.68 (d, 2H), 8.65 (d, 2H), 7.58

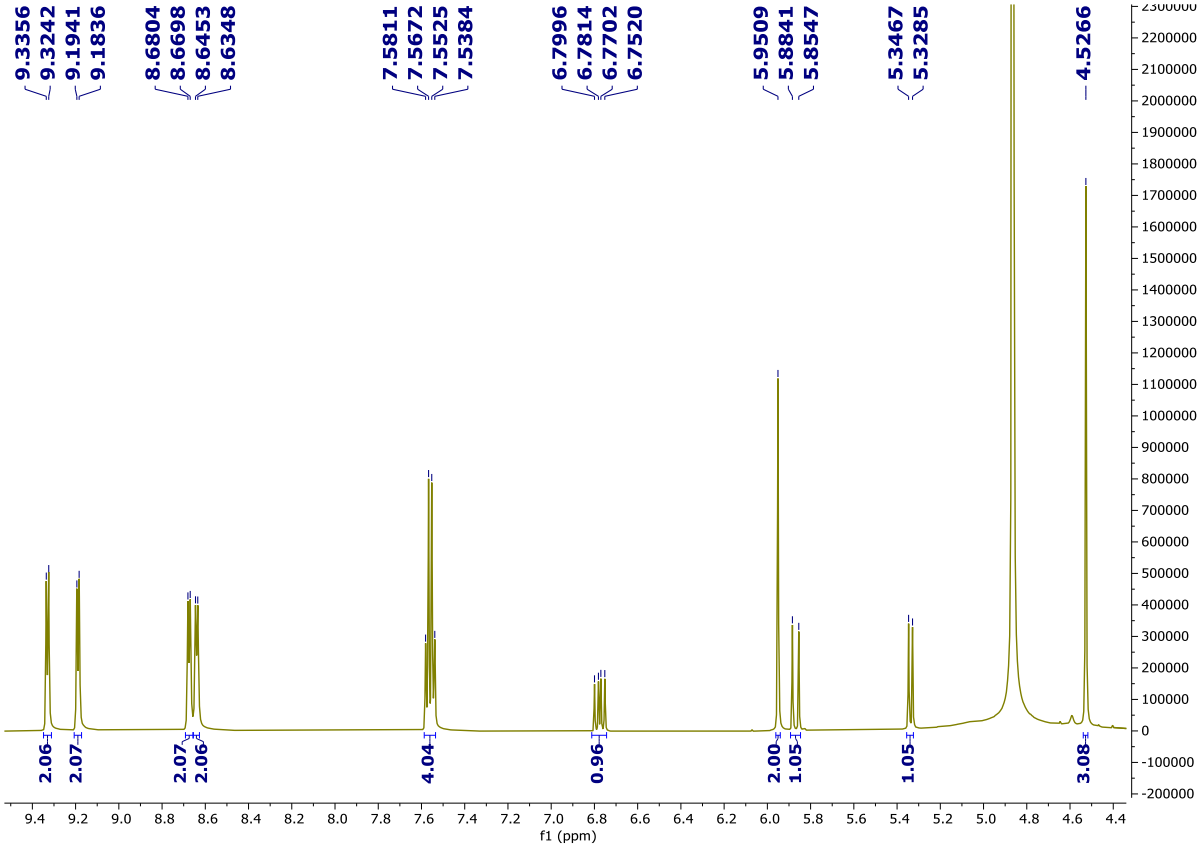

Figure S2. *^{1}H NMR spectrum of compound **14** (CD_3OD, 600 MHz).*

*Synthesis of compound **15**:* In a nitrogen-filled sealed tube, compound **14** (82.34 mg) was dissolved in DMSO (4 ml) and to it $K_2S_2O_8$ (15 mg) was added, and the mixture was heated to 80 °C overnight. The reaction was then stopped and to the mixture acetone was added. The precipitates were collected, redispersed in acetone by sonication and the solvent was removed by centrifugation. The washing step was repeated several times and the solid was collected separately.

1. Kim, J.; Baik, S. S.; Ryu, S. H.; Sohn, Y.; Park, S.; Park, B.-G.; Denlinger, J.; Yi, Y.; Choi, H. J.; Kim, K. S., *Science* **2015,** *349* (6249), 723.
2. Morita, A., *Appl. Phys. A* **1986,** *39* (4), 227.
3. Das, S.; Zhang, W.; Demarteau, M.; Hoffmann, A.; Dubey, M.; Roelofs, A., *Nano Lett.* **2014,** *14* (10), 5733.

4. Castellanos-Gomez, A.; Vicarelli, L.; Prada, E.; Island, J. O.; Narasimha-Acharya, K. L.; Blanter, S. I.; Groenendijk, D. J.; Buscema, M.; Steele, G. A.; Alvarez, J. V.; Zandbergen, H. W.; Palacios, J. J.; van der Zant, H. S. J., *2d Mater.* **2014,** *1* (2), 025001.
5. Liang, L.; Wang, J.; Lin, W.; Sumpter, B. G.; Meunier, V.; Pan, M., *Nano Lett.* **2014,** *14* (11), 6400.
6. Favron, A.; Gaufrès, E.; Fossard, F.; Phaneuf-L'Heureux, A.-L.; Tang, N. Y. W.; Lévesque, P. L.; Loiseau, A.; Leonelli, R.; Francoeur, S.; Martel, R., *Nat. Mater.* **2015,** *14* (8), 826.
7. Huang, Y.; Qiao, J.; He, K.; Bliznakov, S.; Sutter, E.; Chen, X.; Luo, D.; Meng, F.; Su, D.; Decker, J.; Ji, W.; Ruoff, R. S.; Sutter, P., *Chem. Mater.* **2016,** *28* (22), 8330.
8. Dai, J.; Zeng, X. C., *RSC Adv.* **2014,** *4* (89), 48017.
9. Zhou, Q.; Chen, Q.; Tong, Y.; Wang, J., *Angew. Chem. Int. Ed.* **2016,** *55* (38), 11437.
10. Ryder, C. R.; Wood, J. D.; Wells, S. A.; Yang, Y.; Jariwala, D.; Marks, T. J.; Schatz, G. C.; Hersam, M. C., *Nat. Chem.* **2016,** *8* (6), 597.
11. Sofer, Z.; Luxa, J.; Bouša, D.; Sedmidubský, D.; Lazar, P.; Hartman, T.; Hardtdegen, H.; Pumera, M., *Angew. Chem. Int. Ed.* **2017,** *56* (33), 9891.
12. Hu, H.; Gao, H.; Gao, L.; Li, F.; Xu, N.; Long, X.; Hu, Y.; Jin, J.; Ma, J., *Nanoscale* **2018,** *10* (13), 5834.
13. van Druenen, M.; Davitt, F.; Collins, T.; Glynn, C.; O'Dwyer, C.; Holmes, J. D.; Collins, G., *Chem. Mater.* **2018,** *30* (14), 4667.
14. Liu, Y.; Gao, P.; Zhang, T.; Zhu, X.; Zhang, M.; Chen, M.; Du, P.; Wang, G.-W.; Ji, H.; Yang, J.; Yang, S., *Angew. Chem. Int. Ed.* **2019,** *58* (5), 1479.
15. Wood, J. D.; Wells, S. A.; Jariwala, D.; Chen, K.-S.; Cho, E.; Sangwan, V. K.; Liu, X.; Lauhon, L. J.; Marks, T. J.; Hersam, M. C., *Nano Lett.* **2014,** *14* (12), 6964.
16. Arunan, E.; Desiraju, G. R.; Klein, R. A.; Sadlej, J.; Scheiner, S.; Alkorta, I.; Clary, D. C.; Crabtree, R. H.; Dannenberg, J. J.; Hobza, P.; Kjaergaard, H. G.; Legon, A. C.; Mennucci, B.; Nesbitt, D. J., *Pure Appl. Chem.* **2011,** *83* (8), 1619.
17. Matthews, P. D.; Hirunpinyopas, W.; Lewis, E. A.; Brent, J. R.; McNaughter, P. D.; Zeng, N.; Thomas, A. G.; O'Brien, P.; Derby, B.; Bissett, M. A.; Haigh, S. J.; Dryfe, R. A. W.; Lewis, D. J., *Chem. Commun.* **2018,** *54* (31), 3831.
18. Sarkar, I.; Guo, C.; Peng, C.; Wang, Y.; Li, Y.; Zhang, X., *Small* **2025**, 2410300.
19. Hultgren, R.; Gingrich, N. S.; Warren, B. E., *J. Chem. Phys.* **1935,** *3* (6), 351.